國立臺灣大學工學院化學工程學研究所

碩士論文

Graduate Institute of Chemical Engineering

College of Engineering

National Taiwan University

Master Thesis

鹽類價數與奈米通道之幾何形狀對其整流行為的影響

Influences of Salt Valence and Geometric Shape of a

Nanochannel on Its Rectification Behavior

陳俞閔

Yu-Min Chen

指導教授：徐治平 博士

Advisor: Jyh-Ping Hsu, Ph.D.

中華民國 107 年 7 月

July, 2018

中文摘要

在奈米流體尺度下，電雙層重疊效應顯著，使奈米通道可引起許多有趣的電動力學現象，如離子濃度極化(ICP)和離子電流整流(ICR)，也因而製備與合成奈米通道成為奈米科技上的一股熱潮。在第一章節中，我們利用數值模擬的方法，考慮不同電解質溶液 $LaCl_3$、$CaCl_2$、KCl、KNO_3、K_2SO_4，研究其離子價數比之不對稱性對圓錐形奈米通道的離子整流效應所造成的影響。改變價數比時有兩種方式，第一種方式是固定陰離子的價數，改變陽離子的價數;而第二種則是固定陽離子的價數，改變陰離子的價數。我們發現，離子強度與離子擴散係數對其電動力學現象扮演著舉足輕重的角色。另外，定性上帶正電的奈米通道之整流行為與帶負電的奈米通道相似。

第二章節中，我們則是討論一表面具有 pH 可調節電荷之兩性離子基團的仿生雪茄形奈米通道。考慮在外加電場作用下，溶液酸鹼值 pH、溶液鹽濃度、底端的開口半徑以及奈米通道形狀對離子傳輸行為的影響。藉由調節孔口半徑與表面曲率以得到雪茄形奈米通道的最佳整流表現與離子選擇性。除了能夠解釋相關電動力學現象之外，所獲得的結果還為相關設備的複雜設計提供了必要的資訊。

關鍵字：電雙層；離子電流整流；圓錐形奈米通道；離子價數;兩性離子基團；雪茄形奈米通道;形狀效應

Abstract

The overlapping of electric double layer in a nano-scaled system is usually significant, rendering it having profound and interesting electrokinetic phenomena, such as ion concentration polarization (ICP) and ion current rectification (ICR), and thus fabrication of nanodevices becomes a trend of nanotechnology. In Chapter 1, by taking account of various electrolyte solution $LaCl_3$、$CaCl_2$、KCl、KNO_3, and K_2SO_4, a thorough numerical simulation is conducted to illustrate the influence of asymmetry of various ionic valence ratio on the ICR behavior in a conical nanochannel. We show that the electrokinetic phenomena depend highly on ionic strength and ion diffusivity. The qualitative behavior of the ion current rectification of a positively charged conical nanochannel is similar to that of a negatively charged one.

In Chapter 2, we consider a bioinspired cigar-shaped nanochannel where its surface is pH-regulated, and has zwitterionic groups. The influences of the solution pH, the bulk concentration, the base opening radii, and the nanochannel shape on the associated ICR behavior and ionic selectivity are examined, focusing on discussing the underlying mechanisms in detail. We show that the best nanochannel performance can be achieved

by adjusting the base orifice radii and surface curvature appropriately. In addition to proposing underlying mechanisms for the phenomena observed, the results gathered in this study also provide necessary information for designing relevant devices.

III

Contents

List of Figures

V

VI

VIII

IX

X

List of Tables

Chapter 1

Influence of Salt Valence on the Rectification Behavior of Nanochannels
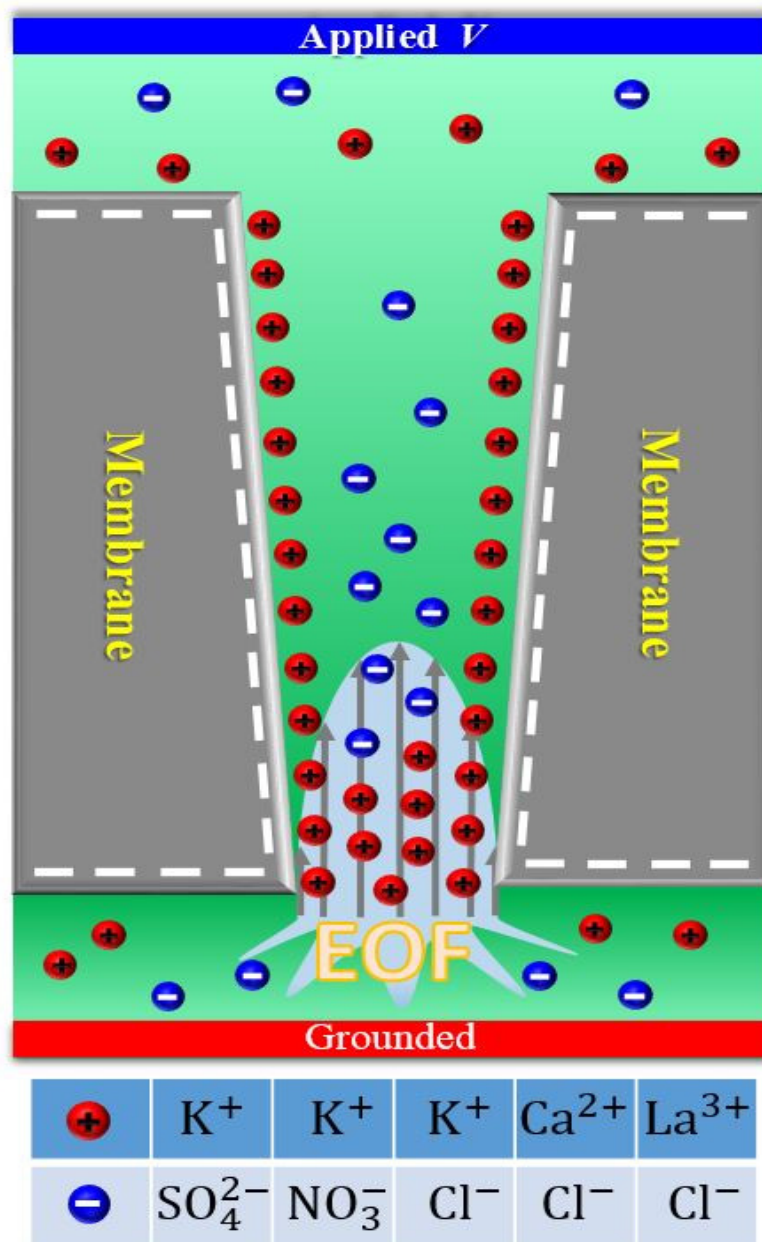
1-1. Introduction

Recent advances in nanoscience and nanotechnology lead to a considerable progress in preparing nanomaterials including, for instance, nanowires and quantum dots, and fabricating nanodevices such as nanopores/nanochannels [1], nanopipettes, and nanoelectrodes. These devices and associated techniques have been applied successfully in various areas such as control of ionic transport [2-10] and detection, analysis, and separation of single nanoparticles [11-15]. The former includes, for instance, ionic gate [16-20], nanofluidic diode [21-26], and energy storage [27-29]. The nanoparticles in the latter include, for example, DNA [30-32], proteins [33], and biomolecules [34,35].
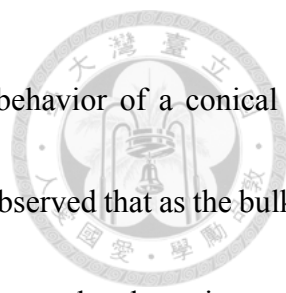
The overlapping of electrical double layer (EDL) in a nano-scaled system is usually significant, rendering it having profound and interesting electrokinetic phenomena. For example, the ionic current coming from the transport of ions in a nanopore may not obey Ohm's law [36]: the magnitude of this current at a negatively applied potential bias can be different from that at a positively applied potential bias. This yields a diode-like behavior, known as ion current rectification (ICR) [36-45], first observed in a conical quartz nanopipette [36]. ICR resembles the behavior of the ionic transport through the ion channels of a biological membrane.

It is generally accepted that ICR occurs to a conical nanopore if its diameter is comparable to the associated Debye screening length (or thickness of EDL) [4]. The diameter of a conical

2

nanopore varies along its axis, so is the degree of EDL overlapping. That is, the asymmetric geometry of a conical nanopore leads to a non-uniform ionic distribution along its axis, resulting in the ICR behavior. Several mechanisms are proposed to explain this behavior including, for example, electric potential barrier inside a nanopore [37], electrochemical properties of the nanopore tip [46,47], and ion enrichment/depletion inside a nanopore [48,49]. In addition to the asymmetric geometry of a nanopore [50-52], ICR might also arise from several other factors, such as the asymmetric charge distribution on the nanopore surface [26,53-56], an imposed salt gradient [41,57], and nanoparticle blocking [58].

Recently, the ICR behavior of a conical nanopore has drawn the attention of many researches. It is found that this behavior can be influenced by parameters including bulk salt concentration [59], surface charge density [51,60], orifice diameter [51,59], cone angle [51,59], tip shape [28,51,59], and pH [61-63]. However, most of the reported results focused on an aqueous KCl solution; only few on other types of salt. Note that both the hydrated radius of ions and Debye screening length depend upon the type of salt, so is the associated electrokinetic behavior. Several efforts were made on analyzing the ICR for the case of divalent salts [64,65]. Neglecting the effect of electroosmotic flow and adopting KCl and K_2SO_4 as representative salts, Perez-Mitta *et al.* [64] studied the influence of the type of salt on the ionic current in an asymmetric nanopore. They showed that the higher the valence of ions the larger the ionic current and the corresponding

3

rectification factor. Wei *et al.* [65] investigated the electrokinetic behavior of a conical PET nanopore by considering MgCl2, CaCl2, LiCl, NaCl, and KCl. They observed that as the bulk salt concentration varies from 0.0001 to 1 M the rectification factor shows a local maximum. The bulk salt concentration at which the rectification factor reaches its local maximum for bi-valent cations is lower than that for mono-valent cations. In addition, the local maximum of the former is larger than that of the latter. While these observations are interesting, the role that the ionic valence plays has not been elaborated comprehensively. Extending their analysis, we examine the electrokinetic behavior of a conical nanochannel by considering mono-, bi-, and tri-valent ions in this study. In addition to a thorough simulation of the behavior of the system under various conditions, the underlying mechanisms are discussed comprehensively.

1-2. Theory

As shown in Figure 1-1, we consider a conical nanochannel of axial length L_N, tip radius R_t, base radius R_b and opening angle θ ($=\tan^{-1}(R_b-R_t)/L_N$) connecting two large, identical reservoirs of axial length L_r and radius R_r. The nanochannel and the two reservoirs are filled with an aqueous salt solution. The nanochannel surface and the reservoir side walls are homogeneously charged with the charge density σ_s. A potential bias V is applied on one reservoir, and the other reservoir grounded (0 V). The electric field thus established drives the ions from one reservoir to the other,

4

yielding an electroosmotic flow (EOF) through the nanochannel. We adopt the cylindrical coordinates (r, θ, z) with its origin at the nanochannel center, and the system is axial symmetric.

Letting z_j, C_j, $\mathbf{v}_j$, D_j, and $\mathbf{u}$ be the valence, the molar concentration, the velocity, the diffusion coefficient of ionic species j, and the fluid velocity, respectively, the ionic flux $\mathbf{N}_j$ can be expressed by Nernst-Planck equation,

$$\mathbf{N}_j = C_j \mathbf{v}_j = C_j \mathbf{u} - D_j (\nabla C_j + \frac{z_j F C_j}{RT} \nabla \phi), j=1, \text{cations, 2, anions} \tag{1.1}$$

F, R, T, and ϕ are Faraday constant, gas constant, the absolute temperature, and the electric potential, respectively. The conservation of ions yields

$$\nabla \cdot \mathbf{N}_j = 0 \tag{1.2}$$

If ρ_e is the space charge density of mobile ions, and ε the permittivity of the liquid phase, the electrical potential ϕ can be described by Poisson equation
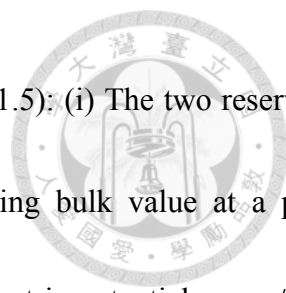
$$\nabla^2 \phi = -\frac{\rho_e}{\varepsilon} = -\sum_{j=1}^{2} \frac{z_j F C_j}{\varepsilon} \tag{1.3}$$

In our case, the Reynolds number of the EOF in a nanochannel is much smaller than unity, that is, the fluid flow is in the creeping flow regime, and the flow field at steady state can be described by the equation of continuity and the modified Navier-Stokes equation.

$$\nabla \cdot \mathbf{u} = 0 \tag{1.4}$$

$$\mu \nabla^2 \mathbf{u} - \nabla p - \rho_e \nabla \phi = \mathbf{0} \tag{1.5}$$

μ and p are the fluid viscosity and the hydrodynamic pressure, respectively.

5

The following boundary conditions are assumed for Eqs. (1.1)-(1.5): (i) The two reservoirs are large, so that the ionic concentration reaches the corresponding bulk value at a point sufficiently away from the nanochannel opening, $C_j=C_{j0}$, and the electric potentials are ϕ (z=-($L_N/2$)-L_r)=V and ϕ (z=($L_N/2$)+L_r)=0. In addition, $\mathbf{n}\cdot\nabla\phi=0$ and $\mathbf{n}\cdot\mathbf{N}_j=0$ are assumed there, where $\mathbf{n}$ is the unit outer normal vector. (ii) The nanochannel surface and the reservoir wall are ion-impenetrable so that $\mathbf{n}\cdot\mathbf{N}_j=0$, and has the constant surface charge density $\sigma_s=-\varepsilon\mathbf{n}\cdot\nabla\phi$. This assumption is reasonable when the solution pH significantly deviates from the pK_a of the dissociable functional groups on the channel surface. In this case, the dissociation of the functional groups on the nanochannel surface is almost complete so that the charge regulation nature can be negligible [66]. (iii) The nanochannel surface and the reservoir walls are non-slip, so that $\mathbf{u}=\mathbf{0}$. (iv) No external pressure gradient is applied. (v) Slip boundary condition for the flow field are specified on the side boundaries of two reservoirs, which are far away from the nanochannel.

If Ω is the surface of either reservoir end normal to the nanochannel axis, the ionic current I through the nanochannel is

$$I=\int_{\Omega} F(z_1\mathbf{N}_1+z_2\mathbf{N}_2)\cdot\mathbf{n}\,d\Omega \tag{1.6}$$

1-3. Results and Discussion

6
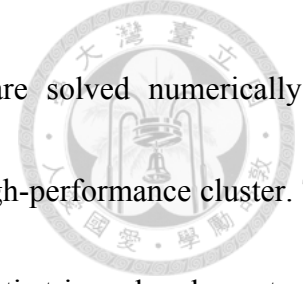
The set of nonlinear, coupled equations, Eqs. (1.1)-(1.5), are solved numerically by COMSOL (version 4.3a, http://www.comsol.com), operated in a high-performance cluster. The computational domain shown in Figure 1-1 is discretized into quadratic triangular elements, and non-uniform elements are employed. Greater number of elements is assigned locally as necessary. Typically, using a total number of 183640 elements is sufficient for recovering convergent result.

The behavior of the system under consideration is examined under various conditions through numerical simulation. For illustration, we assume L_N=3000 nm, R_t=5 nm, L_r=R_r=1000 nm [66], $\varepsilon = 6.95 \times 10^{-10}$ F/m, and $\mu = 10^{-3}$ Pa·s. Five types of salt are considered: KCl, CaCl$_2$, LaCl$_3$, KNO$_3$, and K$_2$SO$_4$. At T=298.15 K, $D_{K^+} = 1.96 \times 10^{-9}$ m^2/s, $D_{Ca^{2+}} = 7.93 \times 10^{-10}$ m^2/s, $D_{La^{3+}} = 6.17 \times 10^{-10}$ m^2/s, $D_{Cl^-} = 2.03 \times 10^{-9}$ m^2/s, $D_{NO_3^-} = 1.90 \times 10^{-9}$ m^2/s, and $D_{SO_4^{2-}} = 1.07 \times 10^{-9}$ m^2/s. The ionic size effect is negligible because the hydration radius for all ions examined are less than 0.4 nm [67], which are much smaller than the smallest length scale of the considered system (i.e., 5 nm). Moreover, the present continuum-based model is valid for capturing the ion transport phenomena in the nanochannel as long as the length scale is larger than 5 nm [68].
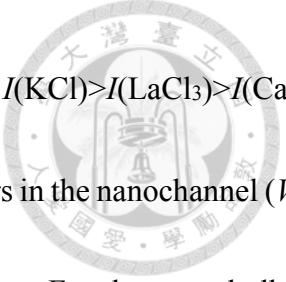
1-3.1 Influence of Cation Valence on the ICR Behavior

The influence of the valence of cations on the ICR behavior of a negatively charged

7

nanochannel is illustrated in Figure 1-2, where the simulated I-V curves of various types of salt having the same anions are shown for two levels of the bulk salt concentration C_0.

Since the potential bias V is applied to the base-end reservoir and the tip-end reservoir grounded, the ionic current I is directed from the based end of the nanochannel to its tip end (i.e., $I>0$) when $V>0$, and reversed when $V<0$ (i.e., $I<0$). Because the nanochannel is negatively charged, $|I(V<0)|>|I(V>0)|$, yielding a diode-like or ICR behavior. Since the lower the bulk salt concentration the thicker the double layer, this behavior is enhanced if C_0 is low.

As seen in Figure 1-2(a), the magnitudes of the ion current rank as $I(LaCl_3)>I(CaCl_2)>I(KCl)$, regardless of the sign of the applied potential bias. This is because the ionic strength ranks as $LaCl_3>CaCl_2>KCl$, so is the associated ionic current. In this case, because the bulk salt concentration is high (300 mM), the overlapping of electric double layer is unapparent, and therefore, ICR phenomenon is insignificant. However, if the bulk salt concentration is low (3 mM), ion depletion (enrichment) occurs in the conical nanochannel when the applied potential bias is positive (negative). The depletion of ions not only leads to a decrease in the concentration of mobile ions but also an increase in the Debye length (or electric double layer thickness), which is the screening length of the surface charge produced by the counterions. In the extreme case where anions are completely excluded by the negatively charged nanochannel, the ionic current is contributed solely by cations (counterions), so that it depends upon their concentration, valence,

8
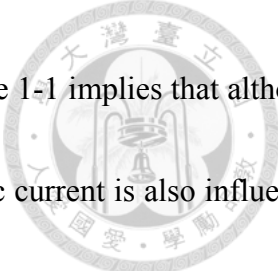
and diffusion coefficient due to Nernst-Planck equation. Therefore, $I(KCl)>I(LaCl_3)>I(CaCl_2)$ for the same bulk salt concentration. Similarly, if ion enrichment occurs in the nanochannel ($V<0$), the concentration of mobile ions increases and Debye length decreases. For the same bulk salt concentration, the concentration of Cl^- ranks as $LaCl_3>CaCl_2>KCl$, so that $I(LaCl_3)>I(CaCl_2)>I(KCl)$.

1-3.2 Influence of Anion Valence on the ICR Behavior
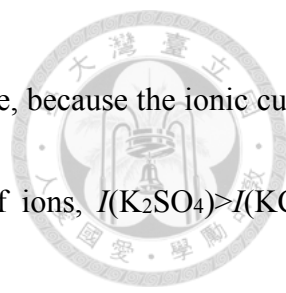
Figure 1-3 illustrates the influence of anions valence on the ICR behavior of a negatively charged nanochannel, where the salts examined have the same cations.

As seen in Figure 1-3(a), the ionic currents associated with the salts examined rank as $I(K_2SO_4)>I(KCl)\cong I(KNO_3)$, regardless of the sign of the applied potential bias. If the bulk salt concentration is sufficiently high (300 mM), the overlapping of electric double layer is insignificant, so is the corresponding ICR behavior. In this case, because the ionic strength ranks as $K_2SO_4>KCl=KNO_3$, the associated ionic current should follow the same trend. However, $I(KCl)$ is slightly larger than $I(KNO_3)$ at a negative applied potential bias. This is because $D_{Cl^-}>D_{NO_3^-}$.

Table 1-1 summarizes the percentage selectivity of anions, $S=\left|I^-/I\right|\times100\%$ with I^- being the ionic current contributed by anions, at two levels of salt concentration. The selectivity of

9

anions at V=-1 V is seen to be much larger than that at V=+1 V. Table 1-1 implies that although

the nanochannel is negatively charged (i.e., cation selective) the ionic current is also influenced

by the transport of anions, especially when $V<0$, because the selectivity of anions (Cl^- and NO_3^-)

is appreciable. Note that if $V<0$, since $D_{Cl^-} > D_{NO_3^-}$, the amount of Cl^- entering the nanochannel is

greater than that of NO_3^-, and therefore, the ionic current contributed by Cl^- is larger than that by

NO_3^-. To maintain electroneutrality, the amount of K^+ coming from KCl is greater than that from

KNO$_3$, so that the ionic current contributed by the K^+ from KCl is greater than that from KNO$_3$.

Due to these two effects, I(KCl)$>I$(KNO$_3$) when $V<0$, as is seen in Table 1-1. If $V>0$, the

selectivity of the cations of KCl and KNO$_3$ (i.e., K^+) exceeds 99 % so that the ionic current of

KCl is almost the same as that of KNO$_3$. However, if the bulk salt concentration is low (3 mM),

the ionic concentration in the nanochannel for $V>0$ is lower than that for $V<0$, especially for

anions. If $V>0$, the depletion of ions leads to a decrease in the concentration of mobile ions, and

therefore, an increase in the thickness of electric double layer. At the low level of C_0 (3 mM),

anions are almost completely excluded from the nanochannel so that the mobile ions inside it are

essentially cations, the concentration of which is governed by its surface charge. Therefore, the

concentrations of cations at $V>0$ for the types of salt examined are almost the same. In this case,

since the ionic current is contributed mainly by cations (K^+), the ionic current is insensitive to the

type of salt, as seen in Figure 1-3(b). Similarly, if $V<0$, the enrichment of ions in the nanochannel

10

yields a decrease in the thickness of electric double layer. In this case, because the ionic current

is governed by the ionic strength and the diffusion coefficient of ions, $I(K_2SO_4) > I(KCl) \cong$

$I(KNO_3)$.

To further explain the results shown in Figure 1-2 and Figure 1-3, we plot the axial variation

in the cross sectional averaged concentration of cations, C_1, and that of anions, C_2, under various

conditions in Figure 1-4 and Figure 1-5. Here, the concentration profile of KNO$_3$ is similar to

that of KCl, except that the latter is slightly higher than the former. As can be seen in Figure 1-4

and Figure 1-5, the concentration of anions correlates with that of cations, which originates from

the ratio of the salt valence in the bulk phase. For example, in the case of K$_2$SO$_4$ the bulk

concentration of K$^+$ is twice that of SO_4^{2-}. Due to ion enrichment/depletion, the concentration of

anions inside the negatively charged nanochannel for $V < 0$ is much higher than that for $V > 0$.

If $V < 0$, the induced negative axial electric field inside the nanochannel attracts the cations in

the tip-end reservoir towards the nanochannel tip. These ions tend to accumulate there due to the

attraction of the fixed charge, yielding a local maximum in the concentration profile. To maintain

electroneutrality, the anions of the tip-end reservoir are also driven towards the nanochannel tip

so that its concentration profile is similar to that of cations. The accumulation of ions near the

nanochannel tip leads to a higher current. On the other hand, if $V > 0$, cations are driven out of the

nanochannel by the induced electric field, so are anions to maintain electroneutrality. The

11
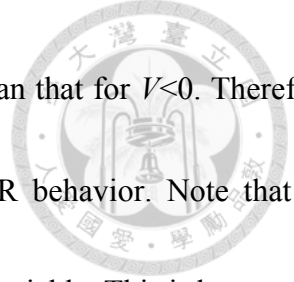
decrease in the ion concentration makes the ionic current smaller than that for $V<0$. Therefore, $R_f=|I(V=-1 \text{ V})/I(V=+1 \text{ V})|>1$, and the nanochannel exhibits an ICR behavior. Note that the concentration of cations near the nanochannel tip for $V>0$ is still appreciable. This is because the decrease in the concentration of mobile ions makes the overlapping of electric double layer significant, especially when the bulk salt concentration is low.
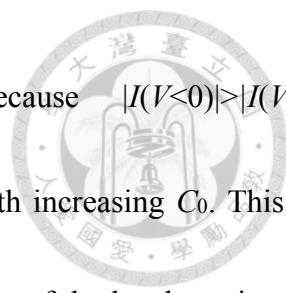
1-3.3 Influence of Bulk Salt Concentration on the ICR Behavior

Figure 1-6 reveals that for all the types of salt examined the rectification factor R_f has a local maximum as the bulk salt concentration C_0 varies. We choose the case of KCl as an example to explain this behavior.

As shown in Figure 1-7, since the nanochannel is negatively charged, the ionic current at a negatively applied potential bias is larger than that at the corresponding positively applied potential bias (i.e., $|I(V<0)|>|I(V>0)|$). Differentiating $|I(V<0)/I(V>0)|$ with respect to C_0 yields
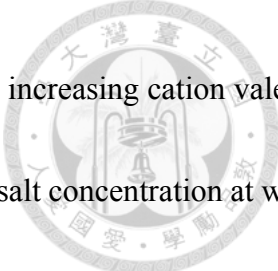
$$\frac{d|I(V<0)/I(V>0)|}{dC_0}=\frac{|I(V>0)|(d|I(V<0)|/dC_0)-|I(V<0)|(d|I(V>0)|/dC_0)}{|I(V>0)|^2} \quad (1.7)$$

Figure 1-7 shows that the slopes of the curves are positive, that is, $d|I(V<0)|/dC_0>0$ and $d|I(V>0)|/dC_0>0$. If C_0 is low (<60 mM), $d|I(V<0)|/dC_0>>d|I(V>0)|/dC_0$, and although $|I(V<0)|>|I(V>0)|$, $d|I(V<0)/I(V>0)|/dC_0>0$, implying that $|I(V<0)/I(V>0)|$ increases with increasing C_0. This is consistent with the results seen in Figure 1-6. In contrast, if C_0 is high (>60

12

mM), $d|I(V<0)|/dC_0 \cong d|I(V>0)|/dC_0$. In this case, because $|I(V<0)|>|I(V>0)|$, $d|I(V<0)/I(V>0)|/dC_0<0$, implying that $|I(V<0)/I(V>0)|$ decreases with increasing C_0. This also agrees with the results seen in Figure 1-6. These explain the presence of the local maximum of R_f at $C_0 \cong 60$ mM for the case of KCl. A similar reasoning was given by Cervera et al. [59]. In fact, if the bulk salt concentration C_0 is adjusted from high C_0 to moderate C_0, because the electric double layer (EDL) becomes thicker, the EDL overlapping is more significant, and thus the ICR effect is more appreciable, yielding a larger R_f. However, if the bulk salt concentration C_0 is further adjusted from moderate C_0 to lower C_0, because the transport ion amounts are too insufficient to generate enough ionic flux, and although the EDL overlapping is quite obvious, the ICR behavior gradually disappears, leading to a decline of R_f. This is why the R_f shows a local maximum as C_0 varies.

When the negative charge on the nanochannel surface is balanced by an excess amount of cations in the electric double layer, the rectification factor R_f reaches its maximum value $R_{f(max)}$. Since multivalent cations carry more amount of charge than monovalent ions, the former has a stronger shielding effect than the latter, and therefore, the $R_{f(max)}$ of the former is reached at a lower salt concentration. In our case, the salt concentrations of KCl, $CaCl_2$, and $LaCl_3$ at which $R_{f(max)}$ occurs are ca. 60 mM, 20 mM, and 10 mM, respectively. Note that, however, regardless of the type of salt, $R_{f(max)}$ occurs at about the same ionic strength or double layer thickness. This

13
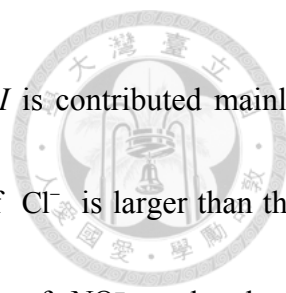
explains the shift in the salt concentration at which $R_{f(max)}$ occurs with increasing cation valence, which was observed experimentally by Wei *et al.* [65]. Similarly, the salt concentration at which $R_{f(max)}$ occurs also shifts to a lower level as the valence of anions increases. For instance, the $R_{f(max)}$ for the case of KCl occurs at $C_0 \cong 60$ mM, but at $C_0 \cong 20$ mM for the case of K_2SO_4. Again, they occur at about the same ionic strength or electric double layer thickness. If two salts have the same valences in cations and anions, the levels of the salt concentration at which $R_{f(max)}$ occurs are the same, but the value of $R_{f(max)}$ depends upon ionic diffusivity. For example, because the diffusivity of Cl^- is larger than that of NO_3^-, $R_f(KCl)>R_f(KNO_3)$. We conclude that the salt concentration at which $R_{f(max)}$ occurs depends mainly on the asymmetry of ionic valence ratio. For the cases of K_2SO_4 (1:2) and $CaCl_2$ (2:1), the salt concentrations (or ionic strength) at which $R_{f(max)}$ occur are also about the same ($C_0 \cong 20$ mM). It can be shown that the ionic strength (or electric double layer thickness) at which $R_{f(max)}$ occurs is independent of the type of salt. In addition, the $R_{f(max)}$ of the multi-valent salt is larger than that of the mono-valent salt, as observed experimentally by Wei *et al.* [65]

As seen in Figure 1-8, since the nanochannel is negatively charged, $|I(V<0)|>|I(V>0)|$. Note that the greater the difference between $|I(V<0)|$ and $|I(V>0)|$ the larger the R_f, and the smaller the difference between them the closer the R_f to unity. Figure 1-8 also reveals that if C_0 is sufficiently high, the higher the valence of ions the faster the rate of increase of I with increasing C_0 at $V>0$,

14

and $I(V>0)$ approaches $I(V<0)$. This is because the higher the ionic strength the thinner the electric double layer, and therefore, less significant the rectification behavior of the nanochannel.

Figure 1-6 also indicates that if C_0 is low, the rectification factor of the salts having common anions ranks as $R_f(LaCl_3)>R_f(CaCl_2)>R_f(KCl)$, but this order is reversed if C_0 is high. This is because if C_0 is low, the difference between $|I(V<0)|$ and $|I(V>0)|$ for the types of salt examined ranks as $LaCl_3>CaCl_2>KCl$, but becomes $KCl>CaCl_2>LaCl_3$ if C_0 is high. If C_0 is low, the R_f for the salts having the same cations in Figure 1-6 ranks as $R_f(K_2SO_4)>R_f(KCl) \cong R_f(KNO_3)$, but this order becomes reversed if C_0 is high. Again, this can be explained by the difference between $|I(V<0)|$ and $|I(V>0)|$. Therefore, we conclude that if the bulk salt concentration is low, the rectification factor ranks as $R_f(\text{multi-valent salt})>R_f(\text{mono-valent salt})$. However, if it is high, then $R_f(\text{mono-valent salt})>R_f(\text{multi-valent salt})$. This behavior was observed experimentally by Wei *et al.* [65]

If two types of salt have the same cations and the same valence ratio, the relative magnitude of the corresponding rectification factors depends upon the diffusivity of anions. For example, because the diffusivity of Cl^- is larger than that of NO_3^-, $R_f(KCl)>R_f(KNO_3)$. Note that the concentration of anions in a negatively charged nanochannel for $V<0$ is much higher than that for $V>0$. In addition, as shown in Table 1-1, the selectivity of anions for $V<0$ is much larger than that for $V>0$. Because the selectivity of anions (Cl^- and NO_3^-) is appreciable, they contribute

15

appreciably to the ionic current I, especially when $V<0$, although I is contributed mainly by cations. As mentioned previously, if $V<0$, because the diffusivity of Cl^- is larger than that of NO_3^- the amount of Cl^- entering the nanochannel is greater than that of NO_3^- so that the ionic current contributed by Cl^- is larger than that by NO_3^-. To maintain electroneutrality, the amount of K^+ coming from KCl is greater than that from KNO₃, implying that the ionic current contributed by the former is larger than that by the latter. Therefore, if $V<0$, I(KCl)$>I$(KNO₃), as seen in Table 1-1.

If $V>0$, the selectivity of cations in the cases of KCl and KNO₃ exceeds 99 %. Since the cations in these two cases are the same, the corresponding ionic currents are almost the same. However, Figure 1-6 shows that the values of R_f in those two cases are different appreciably. As illustrated in Figure 1-9, this is because the associated ionic currents are different if $V<0$. Note that if $V<0$, since the diffusivity of Cl^- is larger than that of NO_3^-, I(KCl)$>I$(KNO₃).

1-3.4 Influence of the Charged Nature of Nanochannel on the ICR Behavior

The rectification factor of a positively charged nanochannel needs be defined as $|I(+V)/I(-V)|=(1/R_f)$ so that it can be compared with that of a negatively charged nanochannel. The profile of $(1/R_f)$ for a positively charged nanochannel presented in Figure 1-10 is similar to that of R_f for the corresponding negatively charged nanochannel. If C_0 is low, the $(1/R_f)$ for the salts having

16
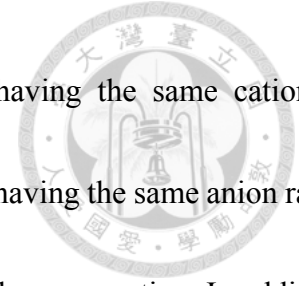
the same anions ranks as $LaCl_3 > CaCl_2 > KCl$, and for the salts having the same cation as

$K_2SO_4 > KCl \cong KNO_3$. In contrast, if C_0 is high, the $(1/R_f)$ for the salts having the same anion ranks

as $KCl > CaCl_2 > LaCl_3$, and $KCl \cong KNO_3 > K_2SO_4$ for the salts having the same cation. In addition,

the level of C_0 at which the local maximum of $(1/R_f)$ occurs depends upon the salt valence: the

higher the valence the lower that level is. We conclude that the qualitative behavior of the ionic

current rectification of a positively charged conical nanochannel is similar to that of a negatively

charged one. Note that, however, the values of $(1/R_f)$ for both $CaCl_2$ and $LaCl_3$ at $\sigma_s = +e/nm^2$

are much smaller than the corresponding values of R_f at $\sigma_s = -e/nm^2$.

Table 1-2 reveals that if $\sigma_s = +e/nm^2$, ion depletion occurs when $V < 0$, and if $\sigma_s = -e/nm^2$, ion

depletion occurs when $V > 0$. This can be explained by that if ion depletion occurs to a positively

charged nanochannel, the ionic current is contributed mainly by anions, that is, anions (cations)

are the major (minor) species. In contrast, cations (anions) are the major (minor) species for a

negatively charged nanochannel. In the case of Table 1-2 if $\sigma_s = +e/nm^2$, Cl^- is the major

species and other cations are the minor species; if $\sigma_s = -e/nm^2$, Cl^- becomes the minor species

and other cations are the major ionic species. Since the concentration of Cl^- is higher than that

of the other cations, and the diffusivity of Cl^- larger than those of the other cations, $\left| I\left(+e/nm^2\right) \right|$

$> \left| I\left(-e/nm^2\right) \right|$ and the observed behavior in the ionic current is reasonable.

If $\sigma_s = +e/nm^2$, ion enrichment occurs when $V > 0$, and if $\sigma_s = -e/nm^2$, ion enrichment occurs

17
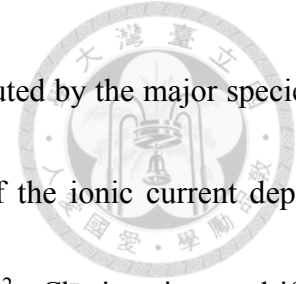
when $V<0$. As shown in Table 3, because the ionic currents contributed by the major species of the salts examined are almost the same, the relative magnitude of the ionic current depends mainly upon the types of coions (i.e., minor species). If σ_s=-e/nm^2, Cl$^-$ is coion, and if σ_s=+e/nm^2, Ca^{2+} and La^{3+} are coion. Because the concentration of Cl$^-$ is higher that of Ca^{2+} and La^{3+} and the diffusion coefficient of Cl$^-$ larger than that of Ca^{2+} and La^{3+}, the magnitude of the ionic current at σ_s=-e/nm^2 is greater than that at σ_s=+e/nm^2. Therefore, for both CaCl$_2$ and LaCl$_3$ the R_f at σ_s=-e/nm^2 is larger than the corresponding $(1/R_f)$ at σ_s=+e/nm^2.

However, for the case of K$_2$SO$_4$, $1/R_f(\sigma_s$=+e/nm$^2)>R_f(\sigma_s$=-e/nm$^2)$. This is because if σ_s=+e/nm^2, ion depletion occurs when $V<0$, and if σ_s=-e/nm^2, ion depletion occurs when $V>0$. The major species is SO$_4^{2-}$ at σ_s=+e/nm^2, and K$^+$ at σ_s=-e/nm^2. Since the concentration of SO$_4^{2-}$ is lower than that of K$^+$ and the diffusion coefficient of SO$_4^{2-}$ is smaller than that of K$^+$, $\left| I\left(+e/nm^2 \right) \right| < \left| I\left(-e/nm^2 \right) \right|$, as seen in Table 1-4.

If σ_s=+e/nm^2, ion enrichment occurs when $V>0$, and if σ_s=-e/nm^2, ion enrichment occurs when $V<0$. As shown in Table 1-5, the magnitude of the ionic current contributed by major species at σ_s=+e/nm^2 is almost the same as that at σ_s=-e/nm^2, the relative magnitude of the ionic currents depends mainly on minor species (coion). In the present case SO$_4^{2-}$ is coion at σ_s=-e/nm^2, and it is K$^+$ at σ_s=+e/nm^2. Because the concentration of SO$_4^{2-}$ is lower than that of K$^+$ and the diffusion coefficient of SO$_4^{2-}$ smaller than that of K$^+$, the magnitude of the ionic current

18
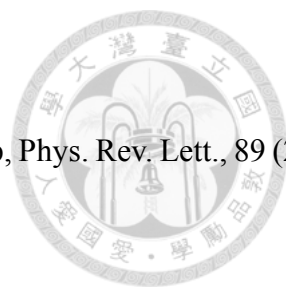
at σ_s =-e/nm^2 is smaller than that at σ_s =+e/nm^2. Therefore, the R_f at σ_s =-e/nm^2 is smaller than

the (1/R_f) at σ_s =+e/nm^2.
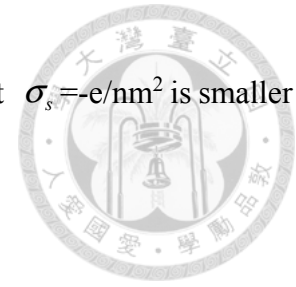
1-4. Conclusions

We analyze theoretically the influence of the ionic valence on the electrokinetic behavior of

a conical nanochannel, in particular, its current-voltage characteristics and ionic current

rectification (ICR) phenomenon. Typical salts including KCl, KNO$_3$, K$_2$SO$_4$, CaCl$_2$, and LaCl$_3$

are considered, for illustration. Due to the difference in the ionic strength and the diffusivity of

ions, the behaviors of the current-voltage curves for the types of salt examined are different both

quantitatively and qualitatively. The rectification factor has a local maximum as the salt

concentration increases. In addition, the local maximum position is related to the asymmetry of

salt valence ratio: the higher the ionic valence the lower the salt concentration at which the

rectification factor has the local maximum. However, the maximal rectification factor occurs at

the same ionic strength, regardless of the type of salt, implying that the thickness of electric

double layer plays the key role. The ICR behavior of a positively charged conical nanochannel

is qualitatively similar to that of a negatively charged nanochannel.

19

References

[1] Z. Siwy, A. Fulinski, Fabrication of a synthetic nanopore ion pump, Phys. Rev. Lett., 89 (2002) 198103.

[2] X. Hou, W. Guo, L. Jiang, Biomimetic smart nanopores and nanochannels, Chem. Soc. Rev., 40 (2011) 2385-2401.

[3] W. Guo, Y. Tian, L. Jiang, Asymmetric ion transport through ion-channel-mimetic solid-state nanopores, Acc. Chem. Res., 46 (2013) 2834-2846.

[4] R.B. Schoch, J.Y. Han, P. Renaud, Transport phenomena in nanofluidics, Rev. Mod. Phys., 80 (2008) 839-883.

[5] D.G. Haywood, A. Saha-Shah, L.A. Baker, S.C. Jacobson, Fundamental studies of nanofluidics: nanopores, nanochannels, and nanopipets, Anal. Chem., 87 (2015) 172-187.

[6] Z.D. Harms, D.G. Haywood, A.R. Kneller, S.C. Jacobson, Conductivity-based detection techniques in nanofluidic devices, Analyst, 140 (2015) 4779-4791.

[7] L. Luo, S.R. German, W.J. Lan, D.A. Holden, T.L. Mega, H.S. White, Resistive-pulse analysis of nanoparticles, Annu. Rev. Anal. Chem., 7 (2014) 513-535.

[8] Y.H. He, M. Tsutsui, C. Fan, M. Taniguchi, T. Kawai, Controlling DNA translocation through gate modulation of nanopore wall surface charges, ACS Nano, 5 (2011) 5509-5518.

[9] J.P. Hsu, T.W. Lin, C.Y. Lin, S.J. Tseng, Salt-dependent ion current rectification in conical

nanopores: impact of salt concentration and cone angle, J. Phys. Chem. C, 121 (2017) 28139-28147.

[10] J.P. Hsu, S.T. Yang, C.Y. Lin, S. Tseng, Ionic current rectification in a conical nanopore: influences of electroosmotic flow and type of salt, J. Phys. Chem. C, 121 (2017) 4576-4582.

[11] C. Dekker, Solid-state nanopores, Nature Nanotech., 2 (2007) 209-215.

[12] S. Howorka, Z. Siwy, Nanopore analytics: sensing of single molecules, Chem. Soc. Rev., 38 (2009) 2360-2384.

[13] S. Lee, Y.H. Zhang, H.S. White, C.C. Harrell, C.R. Martin, Electrophoretic capture and detection of nanoparticles at the opening of a membrane pore using scanning electrochemical microscopy, Anal. Chem., 76 (2004) 6108-6115.

[14] J.E. Wharton, P. Jin, L.T. Sexton, L.P. Horne, S.A. Sherrill, W.K. Mino, C.R. Martin, A method for reproducibly preparing synthetic nanopores for resistive-pulse biosensors, Small, 3 (2007) 1424-1430.

[15] Y.H. Qiu, C.Y. Lin, P. Hinkle, T.S. Plett, C. Yang, J.V. Chacko, M.A. Digman, L.H. Yeh, J.P. Hsu, Z. Siwy, Highly charged particles cause a larger current blockage in micropores compared to neutral particles, ACS Nano, 10 (2016) 8413-8422.

[16] W. Guo, H.W. Xia, L.X. Cao, F. Xia, S.T. Wang, G.Z. Zhang, Y.L. Song, Y.G. Wang, L. Jiang, D.B. Zhu, Integrating ionic gate and rectifier within one solid-state nanopore via modification

with dual-responsive copolymer brushes, Adv. Funct. Mater., 20 (2010) 3561-3567.

[17] A.E. Abelow, O. Schepelina, R.J. White, A. Vallee-Belisle, K.W. Plaxco, I. Zharov, Biomimetic glass nanopores employing aptamer gates responsive to a small molecule, Chem. Commun., 46 (2010) 7984-7986.

[18] M. Ali, S. Mafe, P. Ramirez, R. Neumann, W. Ensinger, Logic gates using nanofluidic diodes based on conical nanopores functionalized with polyprotic acid chains, Langmuir, 25 (2009) 11993-11997.

[19] K. Xiao, G.H. Xie, P. Li, Q. Liu, G.L. Hou, Z. Zhang, J. Ma, Y. Tian, L.P. Wen, L. Jiang, A biomimetic multi-stimuli-response ionic gate using a hydroxypyrene derivation-functionalized asymmetric single nanochannel, Adv. Mater., 26 (2014) 6560-6565.

[20] Q. Liu, K. Xiao, L.P. Wen, H. Lu, Y.H. Liu, X.Y. Kong, G.H. Xie, Z. Zhang, Z.H. Bo, L. Jiang, Engineered ionic gates for ion conduction based on sodium and potassium activated nanochannels, J. Am. Chem. Soc., 137 (2015) 11976-11983.

[21] H. Daiguji, Y. Oka, K. Shirono, Nanofluidic diode and bipolar transistor, Nano Lett., 5 (2005) 2274-2280.

[22] R. Karnik, C.H. Duan, K. Castelino, H. Daiguji, A. Majumdar, Rectification of ionic current in a nanofluidic diode, Nano Lett., 7 (2007) 547-551.

[23] I. Vlassiouk, Z.S. Siwy, Nanofluidic diode, Nano Lett., 7 (2007) 552-556.
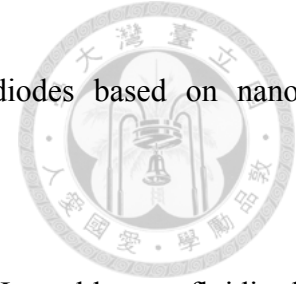
[24] R.X. Yan, W.J. Liang, R. Fan, P.D. Yang, Nanofluidic diodes based on nanotube heterojunctions, Nano Lett., 9 (2009) 3820-3825.

[25] M. Ali, P. Ramirez, S. Mafe, R. Neumann, W. Ensinger, A pH-tunable nanofluidic diode with a broad range of rectifying properties, ACS Nano, 3 (2009) 603-608.

[26] C.Y. Li, F.X. Ma, Z.Q. Wu, H.L. Gao, W.T. Shao, K. Wang, X.H. Xia, Solution-pH-modulated rectification of ionic current in highly ordered nanochannel arrays patterned with chemical functional groups at fesigned positions, Adv. Funct. Mater., 23 (2013) 3836-3844.

[27] J. Gao, W. Guo, D. Feng, H.T. Wang, D.Y. Zhao, L. Jiang, High-performance ionic diode membrane for salinity gradient power generation, J. Am. Chem. Soc., 136 (2014) 12265-12272.

[28] J. Cervera, P. Ramirez, S. Mafe, P. Stroeve, Asymmetric nanopore rectification for ion pumping, electrical power generation, and information processing applications, Electrochim. Acta, 56 (2011) 4504-4511.

[29] J.P. Hsu, S.C. Lin, C.Y. Lin, S. Tseng, Power generation by a pH-regulated conical nanopore through reverse electrodialysis, J. Power Sources, 366 (2017) 169-177.

[30] J. Clarke, H.C. Wu, L. Jayasinghe, A. Patel, S. Reid, H. Bayley, Continuous base identification for single-molecule nanopore DNA sequencing, Nat. Nanotechnol., 4 (2009) 265-270.
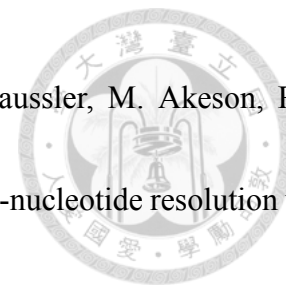
[31] W. Vercoutere, S. Winters-Hilt, H. Olsen, D. Deamer, D. Haussler, M. Akeson, Rapid discrimination among individual DNA hairpin molecules at single-nucleotide resolution using an ion channel, Nat. Biotechnol., 19 (2001) 248-252.

[32] L.J. Steinbock, A. Lucas, O. Otto, U.F. Keyser, Voltage-driven transport of ions and DNA through nanocapillaries, Electrophoresis, 33 (2012) 3480-3487.

[33] R. de la Rica, H. Matsui, Applications of peptide and protein-based materials in bionanotechnology, Chem. Soc. Rev., 39 (2010) 3499-3509.

[34] L.H. Yeh, M.K. Zhang, S.Z. Qian, J.P. Hsu, Regulating DNA translocation through functionalized soft nanopores, Nanoscale, 4 (2012) 2685-2693.

[35] L.H. Yeh, M.K. Zhang, S.W. Joo, S. Qian, J.P. Hsu, Controlling pH-regulated bionanoparticles translocation through nanopores with polyelectrolyte brushes, Anal. Chem., 84 (2012) 9615-9622.

[36] C. Wei, A.J. Bard, S.W. Feldberg, Current rectification at quartz nanopipet electrodes, Anal. Chem., 69 (1997) 4627-4633.

[37] Z. Siwy, Y. Gu, H.A. Spohr, D. Baur, A. Wolf-Reber, R. Spohr, P. Apel, Y. E. Korchev, Rectification and voltage gating of ion currents in a nanofabricated pore, Europhys. Lett., 60 (2002) 349-355.

[38] D. Constantin, Z.S. Siwy, Poisson-Nernst-Planck model of ion current rectification through
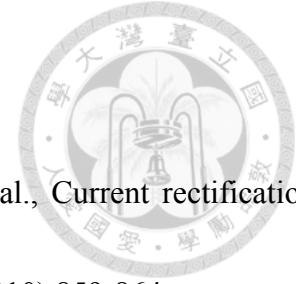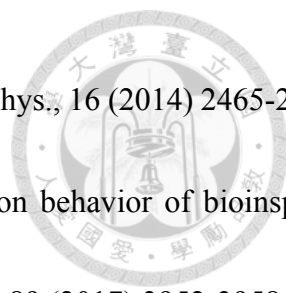
a nanofluidic diode, Phys. Rev. E, 76 (2007) 041202.

[39] W. Guo, H.W. Xia, F. Xia, X. Hou, L.X. Cao, L. Wang, et al., Current rectification in

temperature-responsive single nanopores, Chemphyschem, 11 (2010) 859-864.

[40] W.J. Lan, D.A. Holden, H.S. White, Pressure-dependent ion current rectification in conical-

shaped glass nanopores, J. Am. Chem. Soc., 133 (2011) 13300-13303.

[41] L.X. Cao, W. Guo, Y.G. Wang, L. Jiang, Concentration-gradient-dependent ion current

rectification in charged conical nanopores, Langmuir, 28 (2012) 2194-2199.

[42] T. Yamamoto, M. Doi, Electrochemical mechanism of ion current rectification of

polyelectrolyte gel diodes, Nat. Commun., 5 (2014) 4162.

[43] A.E.P. Schibel, E.N. Ervin, Antigen detection via the rate of ion current rectification change

of the antibody-modified glass nanopore membrane, Langmuir, 30 (2014) 11248-11256.

[44] H.J. Yao, J. Zeng, P.F. Zhai, Z.Z. Li, Y.X. Cheng, J.D. Liu, D. Mo, J.L. Duan, L.X. Wang,

Y.M. Sun, J. Liu, Large rectification effect of single graphene nanopore supported by PET

membrane, ACS Appl. Mater. Inter., 9 (2017) 11000-11008.

[45] M. Miansari, J.R. Friend, L.Y. Yeo, Enhanced ion current rectification in 2D graphene-based

nanofluidic devices, Adv. Sci., 2 (2015) 1500062.

[46] D. Woermann, Electrochemical transport properties of a cone-shaped nanopore: high and

low electrical conductivity states depending on the sign of an applied electrical potential

difference, Phys. Chem. Chem. Phys., 5 (2003) 1853-1858.

[47] D. Woermann, Electrochemical transport properties of a cone-shaped nanopore: revisited, Phys. Chem. Chem. Phys., 6 (2004) 3130-3132.

[48] J.Y. Jung, P. Joshi, L. Petrossian, T.J. Thornton, J.D. Posner, Electromigration current rectification in a cylindrical nanopore due to asymmetric concentration polarization, Anal. Chem., 81 (2009) 3128-3133.

[49] L.J. Cheng, L.J. Guo, Rectified ion transport through concentration gradient in homogeneous silica nanochannels, Nano Lett., 7 (2007) 3165-3171.

[50] Z.S. Siwy, Ion-current rectification in nanopores and nanotubes with broken symmetry, Adv. Funct. Mater., 16 (2006) 735-746.

[51] P. Ramirez, P.Y. Apel, J. Cervera, S. Mafe, Pore structure and function of synthetic nanopores with fixed charges: tip shape and rectification properties, Nanotechnol., 19 (2008) 315707.

[52] H.C. Zhang, Y. Tian, J. Hou, X. Hou, G.L. Hou, R.W. Ou, et al., Bioinspired smart gate-location-controllable single nanochannels: experiment and theoretical simulation, ACS Nano, 9 (2015) 12264-12273.

[53] C.Y. Lin, L.H. Yeh, J.P. Hsu, S. Tseng, Regulating current rectification and nanoparticle transport through a salt gradient in bipolar nanopores, Small, 11 (2015) 4594-4602.

[54] S. Nasir, M. Ali, P. Ramirez, V. Gomez, B. Oschmann, F. Muench, M.N. Tahir, R. Zentel, S.

26
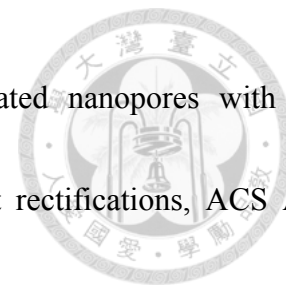
Mafe, W. Ensinger, Fabrication of single cylindrical Au-coated nanopores with non-homogeneous fixed charge distribution exhibiting high current rectifications, ACS Appl. Mater. Inter., 6 (2014) 12486-12494.

[55] M. Tagliazucchi, Y. Rabin, I. Szleifer, Transport rectification in nanopores with outer membranes modified with surface charges and polyelectrolytes, ACS Nano, 7 (2013) 9085-9097.

[56] C.Y. Lin, J.P.Y. Hsu, L. H., Rectification of ionic current in nanopores functionalized with bipolar polyelectrolyte brushes, Sens. Actuator B, 258 (2018) 1223-1229.

[57] J.Y. Lin, C.Y. Lin, J.P. Hsu, S. Tseng, Ionic current rectification in a pH-tunable polyelectrolyte brushes functionalized conical nanopore: effect of salt gradient, Anal. Chem., 88 (2016) 1176-1187.

[58] M. Ali, P. Ramirez, S. Nasir, Q.H. Nguyen, W. Ensinger, S. Mafe, Current rectification by nanoparticle blocking in single cylindrical nanopores, Nanoscale, 6 (2014) 10740-10745.

[59] J. Cervera, B. Schiedt, R. Neumann, S. Mafé, P. Ramírez, Ionic conduction, rectification, and selectivity in single conical nanopores, J. Chem. Phys., 124 (2006) 104706.

[60] D. Stein, M. Kruithof, C. Dekker, Surface-charge-governed ion transport in nanofluidic channels, Phys. Rev. Lett., 93 (2004) 035901.

[61] Z.P. Zeng, Y. Ai, S.Z. Qian, pH-regulated ionic current rectification in conical nanopores

functionalized with polyelectrolyte brushes, Phys. Chem. Chem. Phys., 16 (2014) 2465-2474.

[62] J.P. Hsu, H.H. Wu, C.Y. Lin, S. Tseng, Ion current rectification behavior of bioinspired nanopores having a pH-tunable zwitterionic surface, Anal. Chem., 89 (2017) 3952-3958.

[63] D.H. Lin, C.Y. Lin, S. Tseng, J.P. Hsu, Influence of electroosmotic flow on the ionic current rectification in a pH-regulated, conical nanopore, Nanoscale, 7 (2015) 14023-14031.

[64] G. Perez-Mitta, A.G. Albesa, M.E.T. Molares, C. Trautmann, O. Azzaroni, The influence of divalent anions on the rectification properties of nanofluidic diodes: insights from experiments and theoretical simulations, Chemphyschem, 17 (2016) 2718-2725.

[65] J.Z. Wei, G.H. Du, J.L. Guo, Y.N. Li, W.J. Liu, H.J. Yao, et al., The rectification of mono- and bivalent ions in single conical nanopores, Nucl. Instrum. Meth. B, 404 (2017) 219-223.

[66] C.Y. Lin, F. Chen, L.H. Yeh, J.P. Hsu, Salt gradient driven ion transport in solid-state nanopores: the crucial role of reservoir geometry and size, Phys. Chem. Chem. Phys., 18 (2016) 30160-30165.

[67] Y. Marcus, Ionic radii in aqueous solutions, Chemical Reviews, 88 (1988) 1475-1498.

[68] H. Daiguji, Ion transport in nanofluidic channels, Chemical Society Reviews, 39 (2010) 901-911.
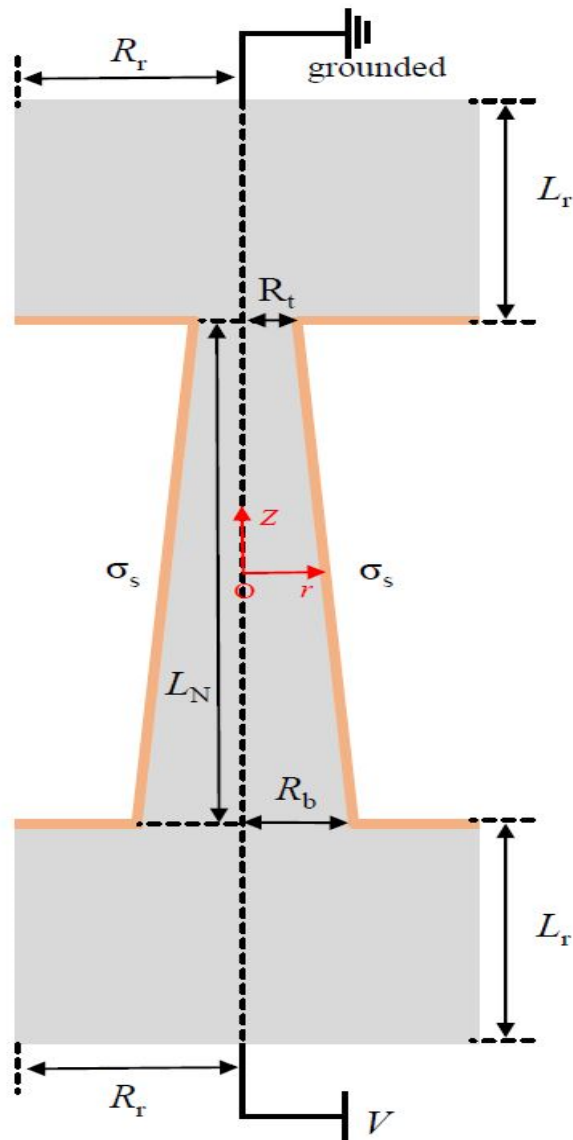
Figure 1-1. A conical nanochannel of axial length L_N, tip radius R_t, base radius R_b, and opening angle θ connecting two large, identical cylindrical reservoirs. The nanochannel surface and the reservoir side walls are homogeneously charged with the density σ_s. An electric potential bias V is applied to base-end reservoir with the tip-end reservoir grounded. L_r and R_r are the length and the radius, respectively, of a cylindrical computation domain defined in each reservoir; (r, θ, z) are the cylindrical coordinates adopted with its origin at the nanochannel center.
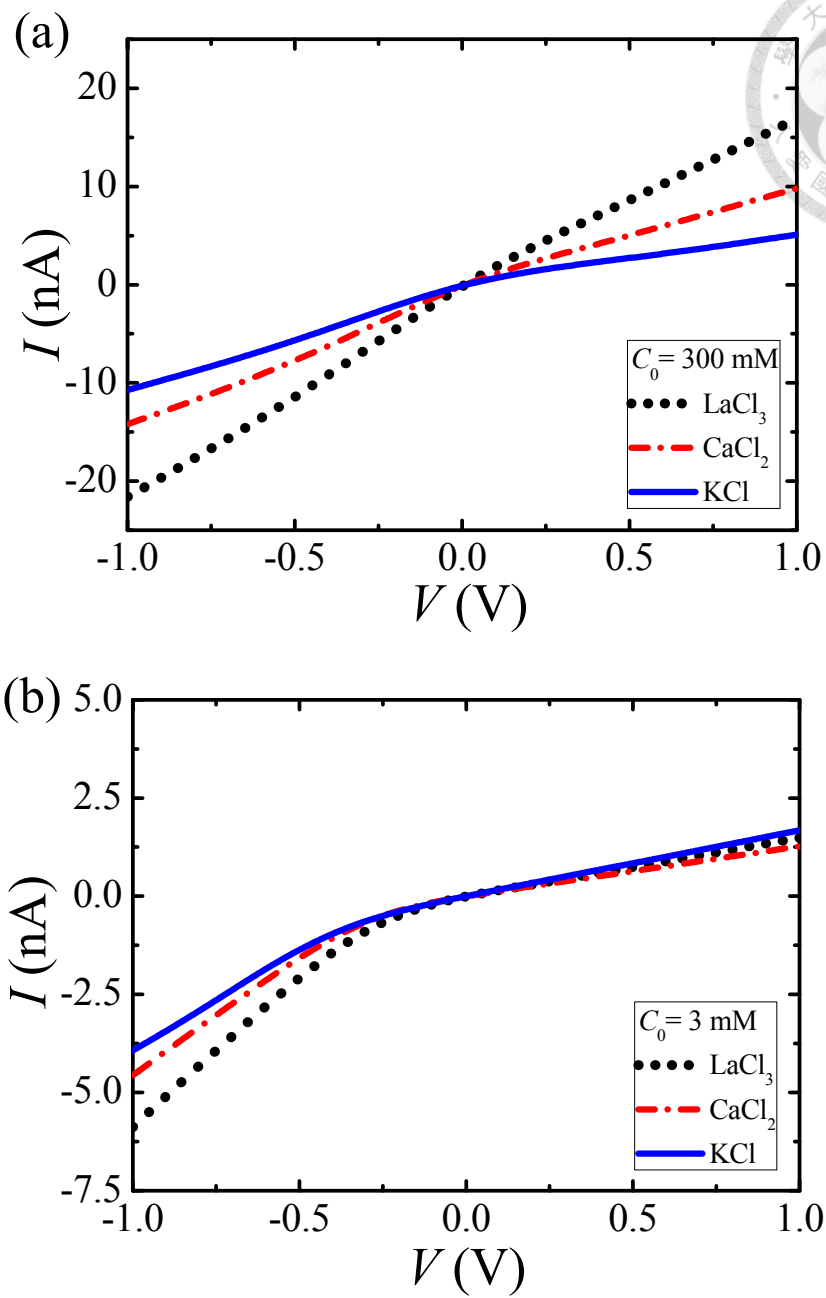
Figure 1-2. Variation of the *I-V* curve of various types of salt having the same anions with the

applied potential bias *V* at $\sigma_s = -1\text{e/nm}^2, \theta = 6°$. (a): C_0=300 mM; (b): C_0=3 mM.
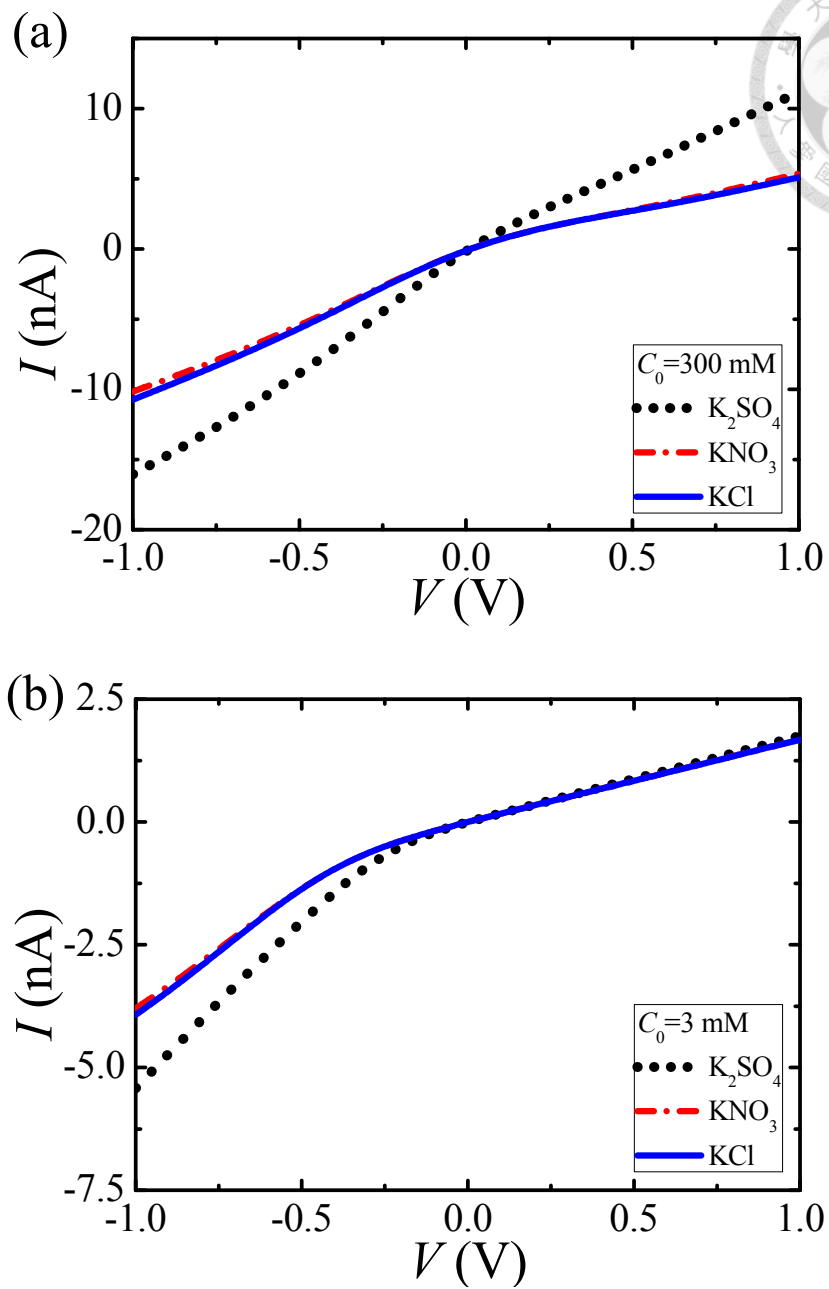
Figure 1-3. Variation of the *I-V* curve of various types of salt having the same cations with the

applied potential bias *V* at $\sigma_s = -1e/nm^2$, $\theta = 6°$. (a): C_0=300 mM; (b): C_0=3 mM.
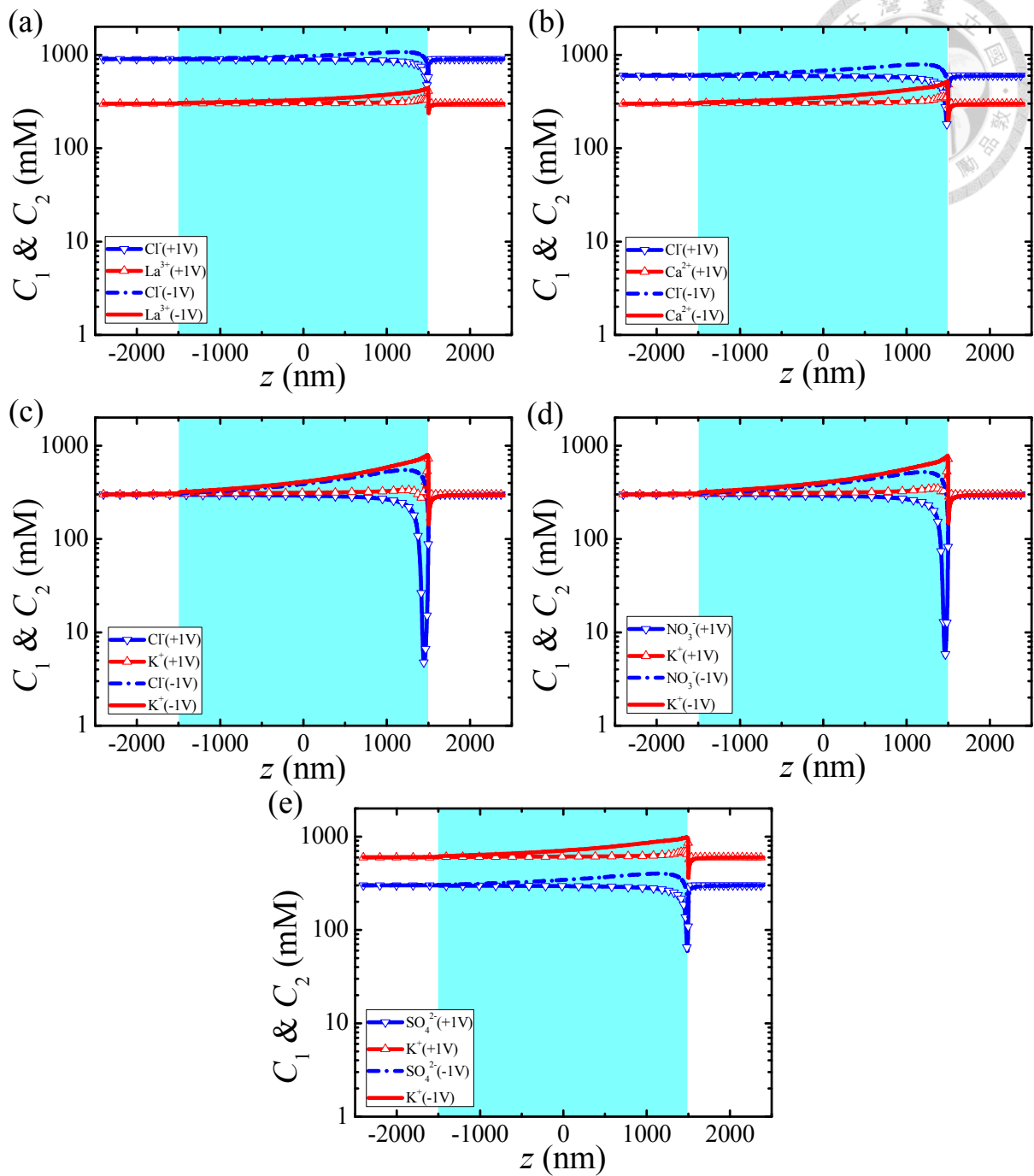
Figure 1-4. Axial variation in the cross sectional averaged concentration of cations (anions) C_1

(C_2) for various types of salt at $V=\pm 1$ V and $C_0=300$ mM. (a) LaCl$_3$, (b) CaCl$_2$, (c) KCl, (d) KNO$_3$,

(e) K$_2$SO$_4$. Red curves: C_1; blue curves: C_2.
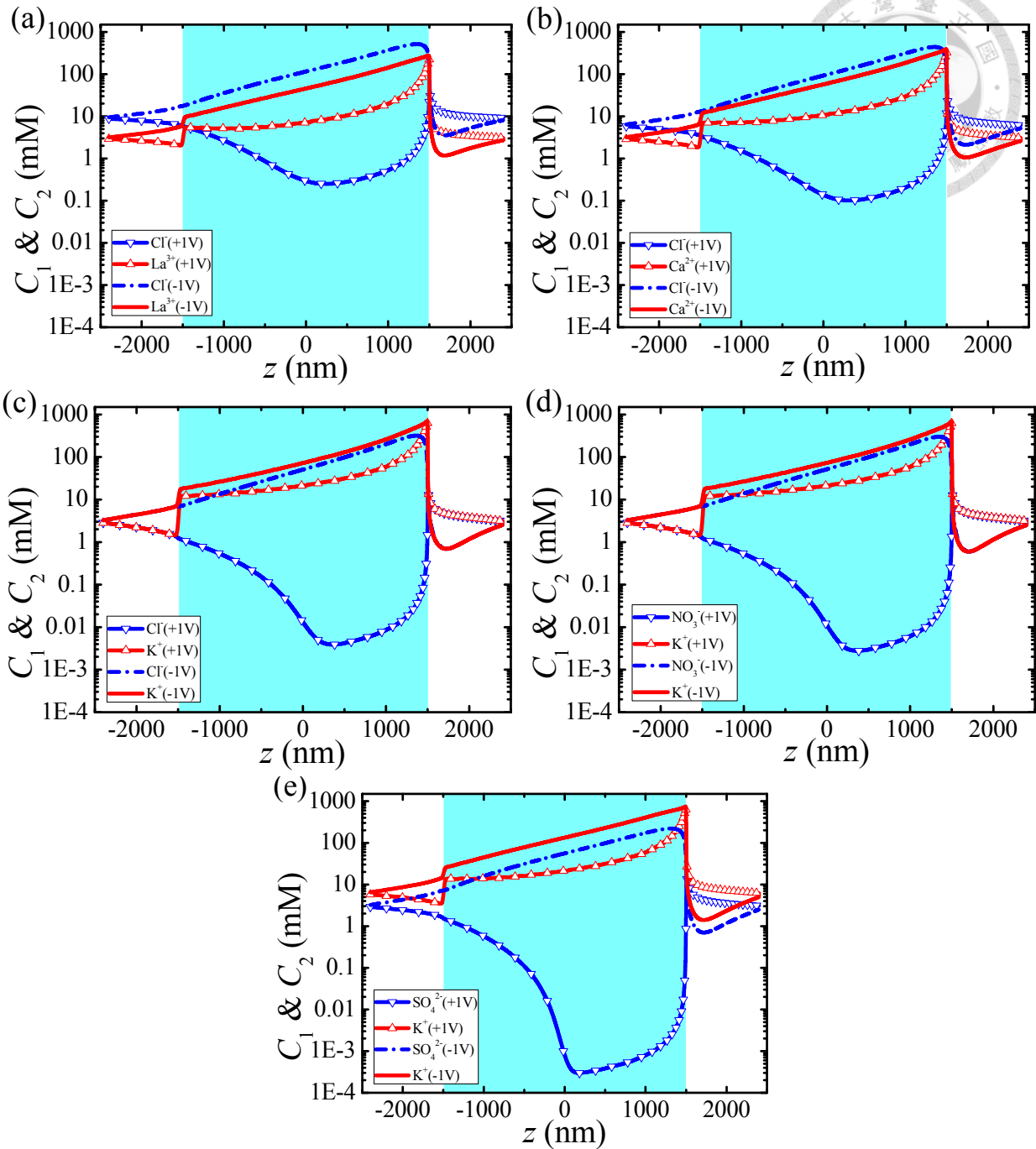
Figure 1-5. Axial variation in the cross sectional averaged concentration of cations (anions) C_1

(C_2) for various types of salt at $V=\pm 1$ V and $C_0=3$ mM. (a) LaCl$_3$, (b) CaCl$_2$, (c) KCl, (d) KNO$_3$,

(e) K$_2$SO$_4$. Red curves: C_1; blue curves: C_2.

33
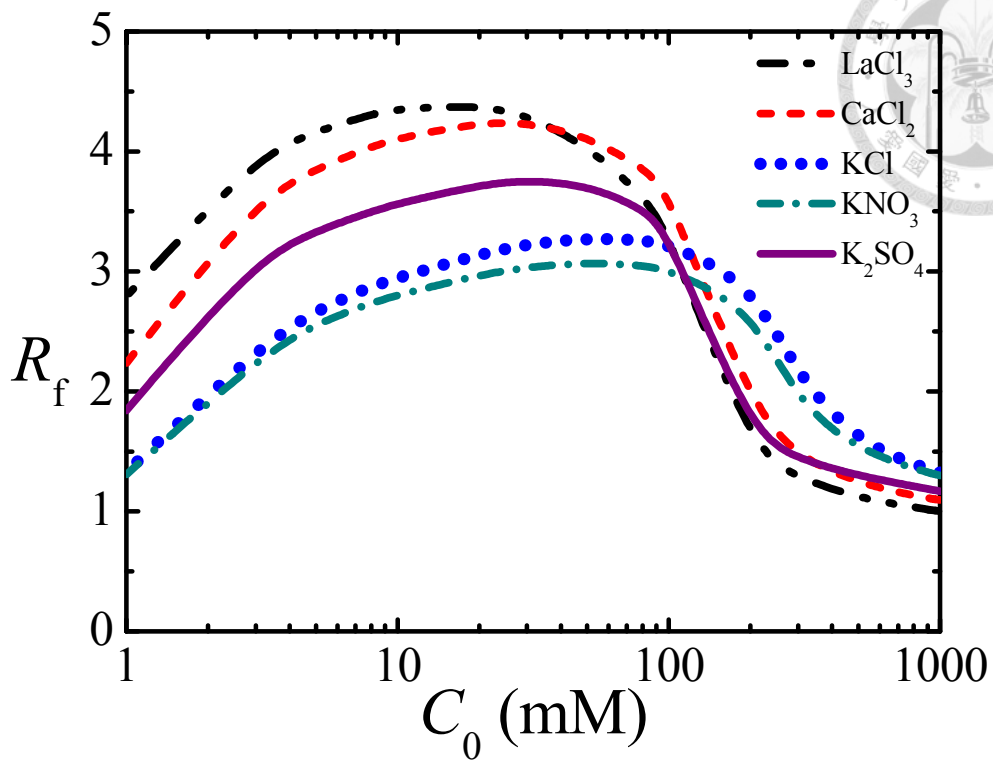
Figure 1-6. Variation in the rectification factor R_f with the bulk salt concentration C_0 for

various types of salt at $V=\pm 1$ V.

34
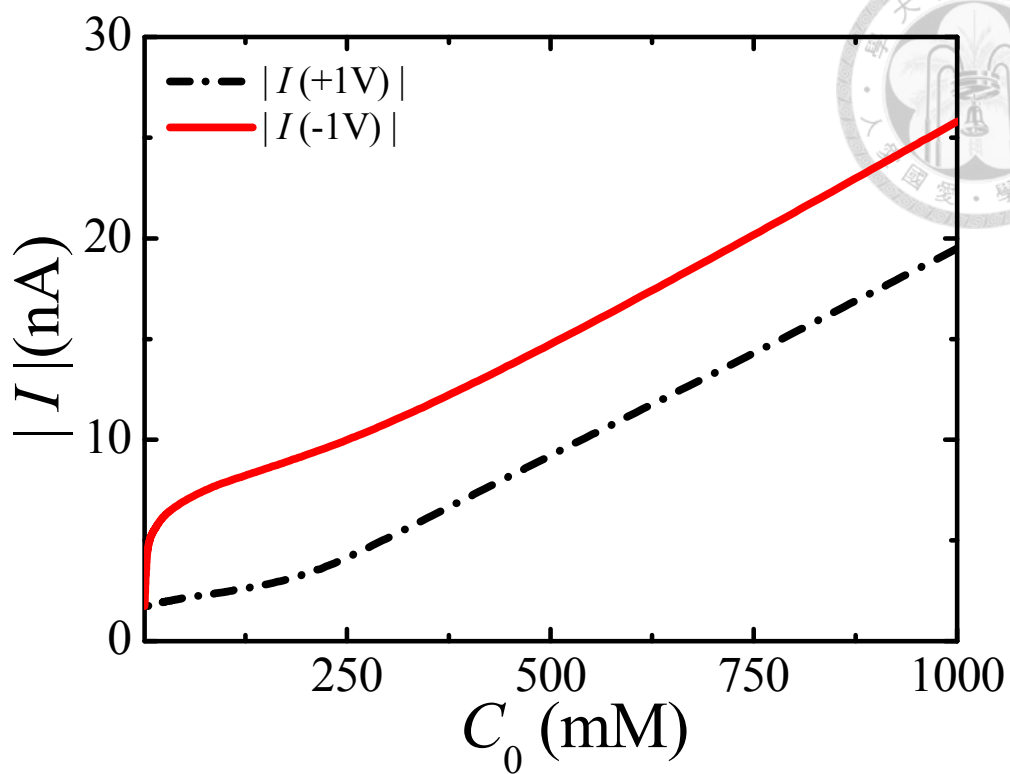
Figure 1-7. Variation in the magnitude of the ionic current |I| with the bulk salt

concentration C_0 at $V=\pm 1$ V for the case of KCl. Solid red curve: I(-1V); dashed black

curve: I(+1V).
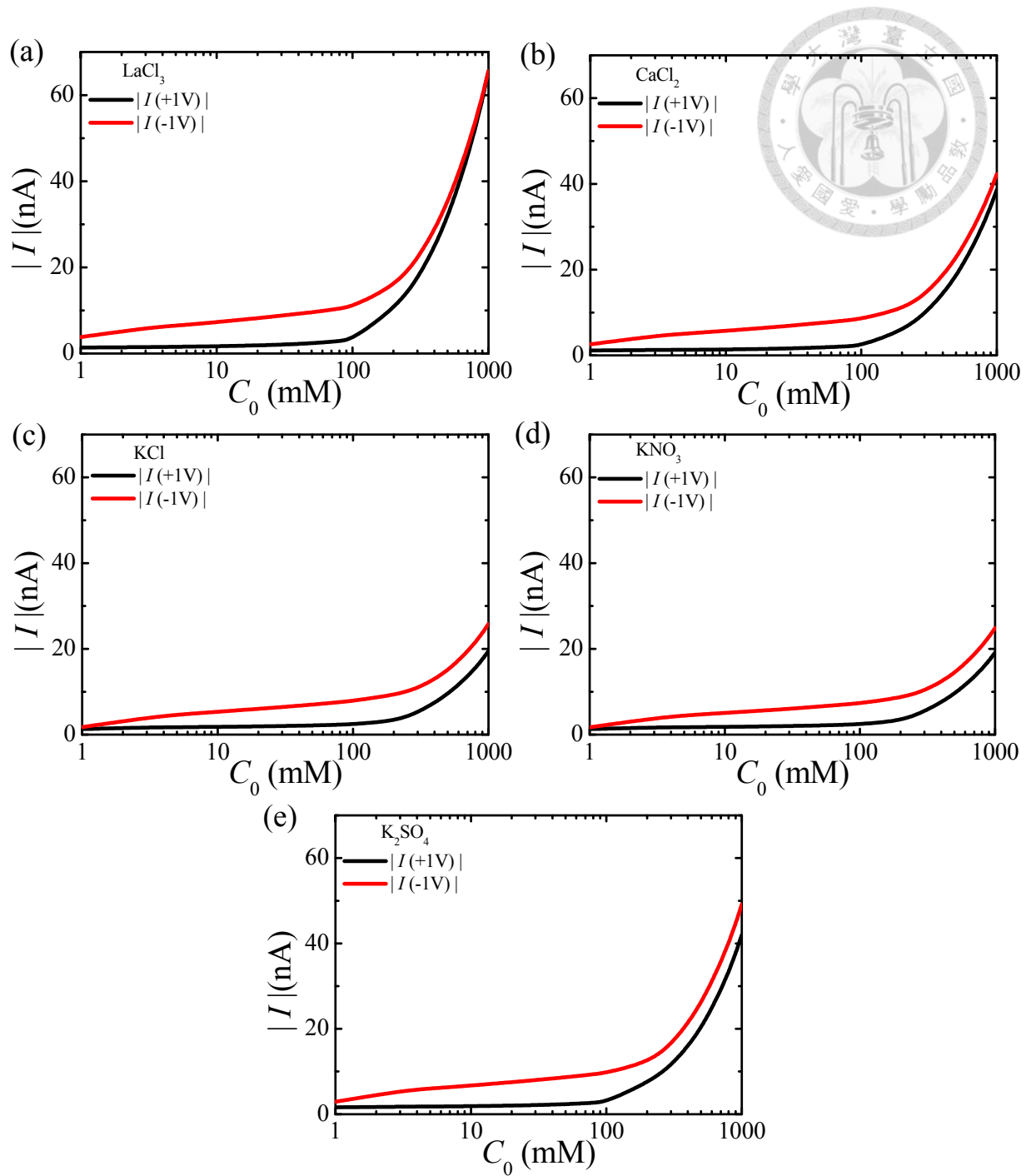
Figure 1-8. Variation in the magnitude of the ionic current $|I|$ with the bulk salt concentration C_0 at $V=\pm 1$ V for various types of salt.
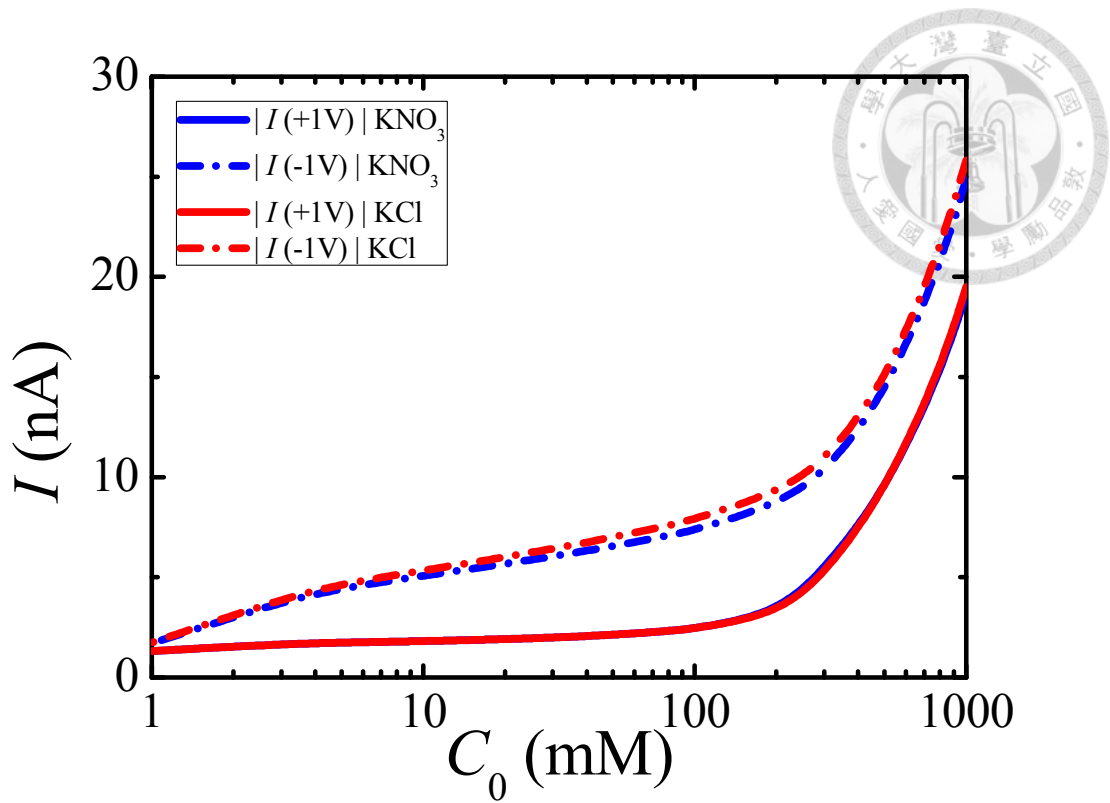
Figure 1-9. Ionic current I vs bulk salt concentration C_0 at $V=\pm 1$ V for the cases of KCl and

KNO$_3$. Red curve: KCl; blue curve: KNO$_3$; solid curve: V=+1V; short dash dot curve: V=-1V.
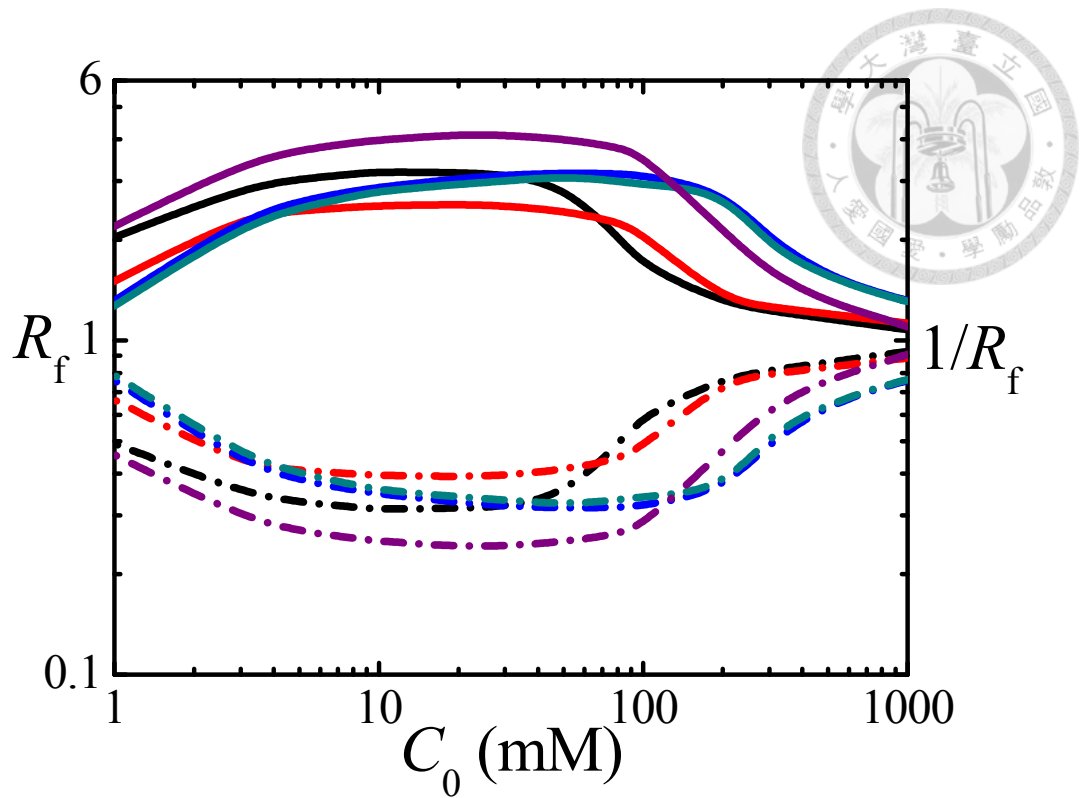
Figure 1-10. Variations of R_f (dashed curves) and ($1/R_f$) (solid curves) as a function of C_0 for various types of salt at $V=\pm1$ V and $\sigma_s =+$e/nm^2. Black curve: LaCl$_3$; red curve: CaCl$_2$; blue curve: KCl; green curve: KNO$_3$; purple curve: K$_2$SO$_4$.
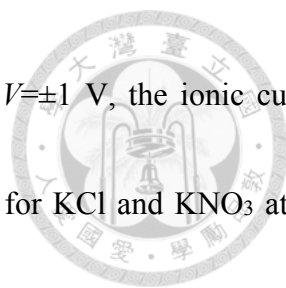
Table 1-1. Percentage selectivity of anions, $S = \left| I^- / I \right| \times 100\%$, at $\mid V = \pm 1$ V, the ionic current contributed by anions, I^-, and the total ionic current, I, at $V=-1$V for KCl and KNO$_3$ at two levels of C_0.

%	KCl		KNO$_3$	
C_0 (mM)	300	3	300	3
S ($V=+1$ V)	1	0.07	0.8	0.06
S ($V=-1$ V)	10.7	7.4	8.5	5.5
$V=-1$V				
C_0 (mM)	300	3	300	3
I^- (nA)	-1.15	-0.29	-0.86	-0.21
I (nA)	-10.73	-3.93	-10.16	-3.79
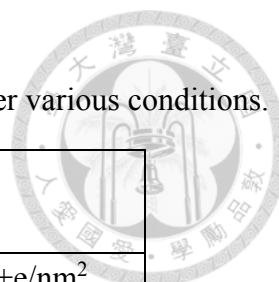
Table 1-2. Ionic current I (nA) for the cases of $CaCl_2$ and $LaCl_3$ under various conditions.

CaCl₂		
C_0=20 mM	σ_s =-e/nm²	σ_s =+e/nm²
I(-1V)	-6.48	-2.06
I(+1V)	1.53	5.26
LaCl₃		
C_0=10 mM	σ_s =-e/nm²	σ_s =+e/nm²
I(-1V)	-7.30	-1.99
I(+1V)	1.67	6.33

Table 1-3. Ionic currents I (nA) contributed by the major and minor species for the case of

$CaCl_2$ and $LaCl_3$ under various conditions when ion enrichment occurs.

CaCl₂		
C_0=20 mM	σ_s =-e/nm²	σ_s =+e/nm²
major species	-5.26 (Ca^{2+})	5.25 (Cl^-)
minor species	-1.22 (Cl^-)	0.016 (Ca^{2+})
LaCl₃		
C_0=10 mM	σ_s =-e/nm²	σ_s =+e/nm²
major species	-5.90 (La^{3+})	6.07 (Cl^-)
minor species	-1.40 (Cl^-)	0.26 (La^{3+})

Table 1-4. Ionic current I (nA) for the case of K_2SO_4 at C_0=20 mM.

	σ_s =-e/nm^2	σ_s =+e/nm^2
I(-1V)	-7.47	-1.90
I(+1V)	2.01	7.85

Table 1-5. Ionic current I (nA) contributed by the major and minor species for the case of

K_2SO_4 at σ_s =±e/nm^2 and C_0=20 mM when ion enrichment occurs.

	σ_s =-e/nm^2	σ_s =+e/nm^2
major species	-6.69 (K^+)	6.64 (SO_4^{2-})
minor species	-0.78 (SO_4^{2-})	1.21 (K^+)

41
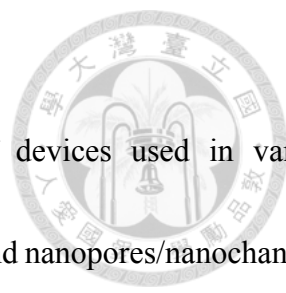
Chapter 2

Electrokinetic Ion Transport in Cigar-Shaped Nanochannels Functionalized with a pH-Tunable Zwitterionic Surface
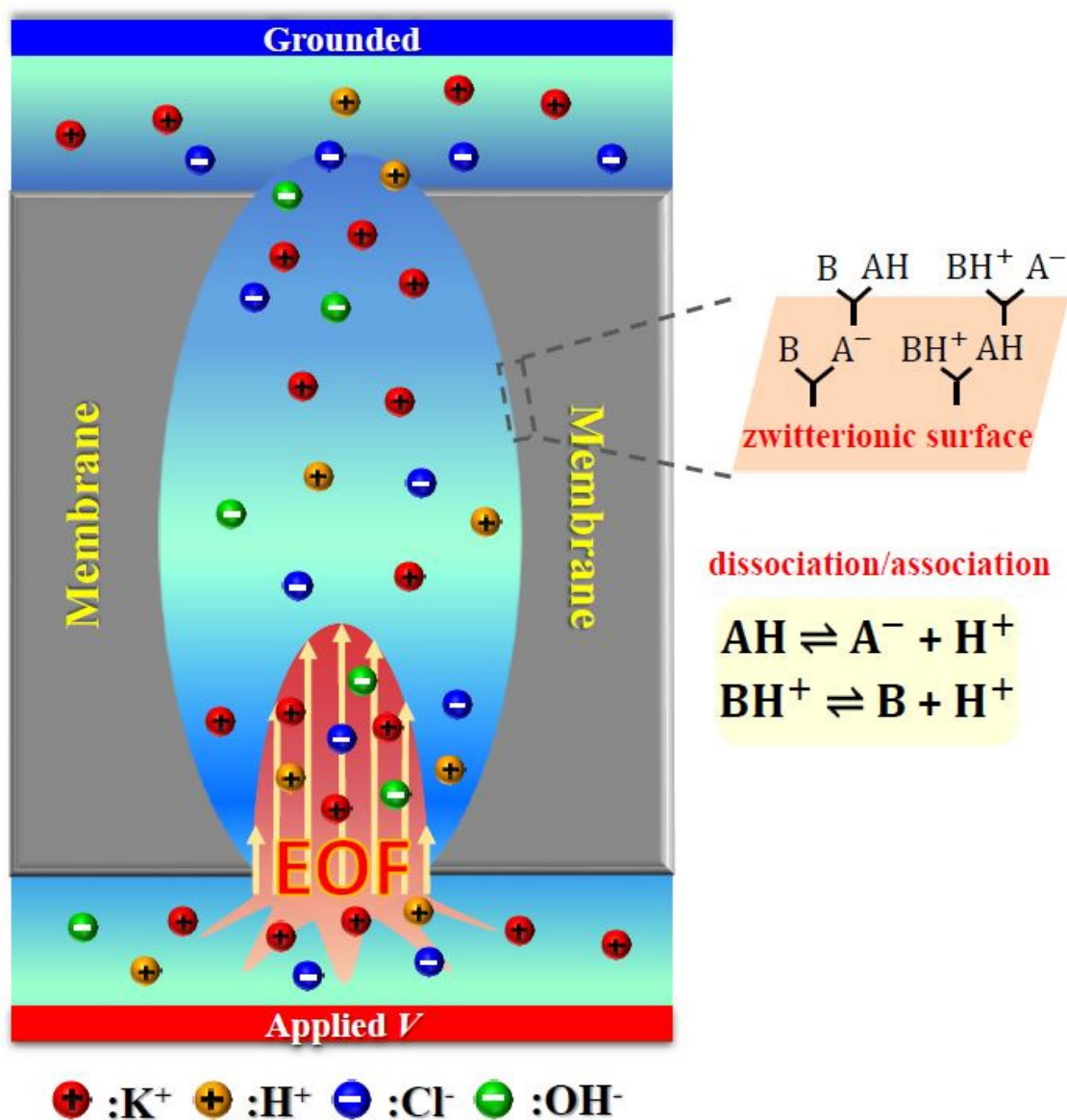
2-1. Introduction

Recent progress in nanotechnology facilitates fabrication of devices used in various applications, including, for example, nanopipettes, nanoelectrodes, and nanopores/nanochannels. In addition to capable of simulating biological ion channels, surface functionalized nanopores/nanochannels are also readily applicable in sensing ions and biomolecules[1-5], modeling nanofluidic diodes[6-11], ionic gates[12-16], and controlling the transport ions and particles[17-23]. Recent applications of nanopores/nanochannels also include renewable energy storage[24-26], desalination of seawater[27,28], and controlled release of drugs[29]. Moreover, inspired by biological ion channels and ion pumps[30-32] existing in cell membrane to intelligently control ions into and out of it, bioinspired artificial functional nanochannels are essential for various vital processes including maintaining cellular ion homeostasis[33] and energy conversion[34-36].
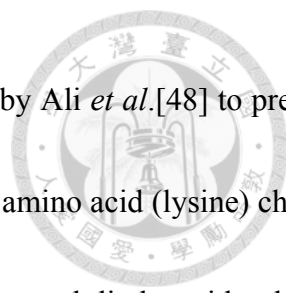
For an aqueous, monovalent salt solution of concentration 10^{-3} M the associated thickness of electric double layer (EDL), or Debye length[37], is ca. 10 nm at room temperature. This implies that the overlapping of EDL in a nanopore or nanochannel having a linear size of that order is significant, yielding several interesting electrokinetic phenomena. These include, for example, ionic current rectification (ICR)[38,39], ion selectivity[40,41], and ion concentration polarization (ICP)[42,43]. These phenomena are important in nanopore-based biosensing[44], and the

43

associated mechanisms have many potential applications in regulating ion transport[45], and

separation and detection of bioentities[46], to name a few.

Ionic current rectification (ICR) is an asymmetric diode-like current-voltage behavior, where

the ionic current arising from an applied potential bias exhibits a preferential direction. For a

nano-scaled device, ICR can come, for example, from its asymmetric geometry [38,47], non-

uniform surface charge[48,49], and an imposed salt concentration gradients[50]. Several

mechanisms have been proposed for interpreting this phenomenon, including, for instance, the

electrochemical prosperities of the tip of a nanopore[51], electric potential barrier inside a

nanopore[52], and the enrichment/depletion of ions inside a nanopore[53]. The results of recent

studies reveal that the ICR behavior of a nanopore can be influenced by factors such as the applied

voltage[54,55], bulk salt concentration [54-56], its shape [55,56], electroosmotic flow[57], pH

[56-58], and temperature[59].

Nanopores/nanochannels can be organic, inorganic, biological, or composite. Several

fabrication techniques were proposed including, for instance, track-etching, electrochemical

etching, electron beam, laser, and self-assembly of biological molecules. It was shown that both

the shape and the structure of a polymeric nanochannel can be designed through controlling

etching conditions. Adopting polyethylene terephthalate (PET) membrane, Apel *et al.*[60]

prepared single nanopore by irradiating it with single swift heavy ions using a surfactant-

controlled track-etching technique. A similar approach was adopted by Ali *et al.*[48] to prepare

cigar-shaped nanopores with its wall functionalized with amphoteric amino acid (lysine) chains.

It was shown that the nanopores obtained can be operated as resistors and diodes with a broad

range of rectifying properties. Their results are informative for interpreting ionic transport in

biological systems such as ion channels, and relevant application of tunable nanopore technology

such as information processing and drug controlled release. However, both the orifice radii of a

nanopore and the shape of its surface are fixed in their analysis, a more detailed discussion on

the influence of these key parameters is highly desirable.

Various types of nanochannel shape and ways that the nanochannel surface are functionalized

have been proposed. The former includes, for example, conical nanopores, concave nanopores

having a bullet-like tip, and convex nanopores having a trumpet-like tip. Assuming constant

surface charge density, Ramírez *et al.*[55] investigated comprehensively the influence of the

shape of a nanopore on its rectification and ionic selectivity behaviors. They found that as a bullet

(trumpet) like nanopore approaches a conical nanopore, both the rectification factor and the

conductance decrease (increase), but the selectivity increases (decreases). Since a Poisson-

Nernst-Planck (PNP) model is adopted in their analysis, the electroosmotic (EOF) effect[57],

which can be significant if the solution pH deviates appreciably from the isoelectric point and the

applied electric potential bias is high, is neglected. In addition, instead of maintaining constant

charge density, the surface of a nanopore is usually charge- or pH-regulated. This nature comes either from the properties of the original material or from that of the materials used to functionalize the nanopore surface.
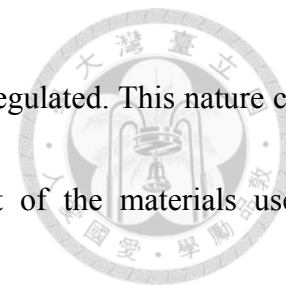
Inspired by the ion channels and ion pumps existing in cell membrane, Zhang *et al*.[61] showed that through applying a pH gradient a cigar-shaped nanochannel can serve as a double-gate: it can open and close alternately under a symmetric pH gradient, and simultaneously under an asymmetric pH gradient. Their study was followed by Liu *et al*.[15] to develop a double-gated nanochannel which is dual-responsive to K^+ and pH. While these results are very interesting and valuable, the behavior of the electrokinetic ion transport in the cigar-shaped nanochannel deserves a more detailed discussion. In fact, the available theoretical results for that behavior in a nanopore/nanochannel having a pH-regulated surface bearing zwitterionic groups, taking account of the effects of pH and pore/channel geometry simultaneously are still very limited. However, obtaining these results is highly desirable and necessary for a sophisticated design of relevant devices.

In this study we simulate the rectification and ionic selectivity behaviors of a cigar-shaped nanochannel having a pH-regulated surface bearing zwitterionic groups, taking account of the EOF effect. A thorough numerical simulation is conducted to illustrate the influences of the surface curvature, the base opening radii, and the bulk salt concentration and pH. In addition to

46
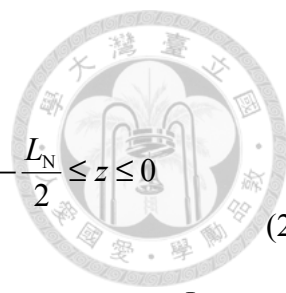
searching for the optimum conditions, the underlying mechanisms are also elaborated.

2-2. Theory

As shown schematically in Figure 2-1, we consider a cigar-shaped nanochannel having the

tip, base, and center radii R_t, R_b, and R_c, respectively, and axial length L_N connecting two large,

identical, cylindrical reservoirs of radius R_r and length L_r. The nanochannel can be formed by, for

example, etching a membrane, and L_N corresponds to its thickness. Both the nanochannel and the

two reservoirs are filled with an incompressible, aqueous Newtonian salt solution. The two

reservoirs are large enough so that the concentration of each ionic species at places far away from

the membrane maintains its bulk ionic concentration. A potential bias V is applied across the

nanochannel with the electrode in the upper reservoir ground (0 V). The external electric potential

difference across the nanochannel drives the electroosmotic flow and the ion transport through

the nanochannel, and then it yields an ionic current. The system under consideration is axial

symmetric, and we choose to work on the cylindrical coordinates (r, θ, z) with the origin placed

at the center of the nanochannel tip end.

The surface of the nanochannel can be described by Zhang *et al.*[61]

47

$$r(z) = \begin{cases} \dfrac{R_c - R_t \exp\left[-(L_N/2h_1)\right] - (R_c - R_t)\exp\left[-(\dfrac{-z}{L_N/2})(L_N/2h_1)\right]}{1-\exp\left[-(L_N/2h_1)\right]}, & -\dfrac{L_N}{2} \leq z \leq 0 \\[4mm] \dfrac{R_c - R_b \exp\left[-(L_N/2h_2)\right] - (R_c - R_b)\exp\left[-(\dfrac{z+L_N}{L_N/2})(L_N/2h_2)\right]}{1-\exp\left[-(L_N/2h_2)\right]}, & -L_N \leq z < -\dfrac{L_N}{2} \end{cases} \quad (2.1)$$

where $R_c=r(z=-L_N/2)$, $R_t=r(z=0)$, $R_b=r(z=-L_N)$, h is a geometry parameter characterizing the curvature of the nanochannel profile, or the curvature radius, and $L_N/2h$ is the shape-controlling parameter which depends on degree of etching. As $L_N/2h \to 0$, the nanochannel approaches a bi-conical one, and $L_N/2h$ increases, it becomes more cigar-like. The opening radii (R_t and R_b) can be adjusted by modifying.

The surface of the nanochannel is modified by materials having pH-tunable, zwitterionic functional groups so that it bears charges when immersed in an aqueous solution, implying that their charges are exquisitely dependent on the local concentration of protons. To mimic the pH-regulated nature of biological ion channels, let AH and B be the corresponding acidic and basic functional groups, respectively, with associated reactions $AH \rightleftharpoons A^- + H^+$ and $BH^+ \rightleftharpoons B + H^+$, and equilibrium constants $K_A = \Gamma_{A^-}[H^+]/\Gamma_{AH}$ and $K_B = \Gamma_B[H^+]/\Gamma_{BH^+}$, respectively. $[H^+]$ and Γ_m are the molar concentration of H^+ (mM) and the surface site density of species m (AH, A^-, BH^+, and B), respectively. For simplicity, we assume that the acidic and the basic functional groups have the same density Γ_t so that $\Gamma_{A^-} + \Gamma_{AH} = \Gamma_{BH^+} + \Gamma_B = \Gamma_t$. Therefore, if e is the elementary charge, the

48
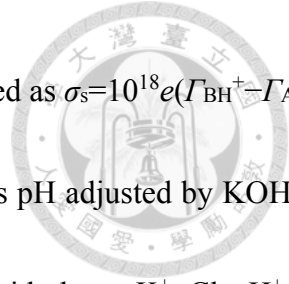
surface charge density of the nanochannel, σ_s (C/m^2), can be expressed as $\sigma_s=10^{18}e(\Gamma_{BH^+}-\Gamma_{A^-})$.

Suppose that the liquid phase is an aqueous KCl solution with its pH adjusted by KOH and

HCl, implying that four kinds of ionic species are present in the liquid phase: K$^+$, Cl$^-$, H$^+$, and

OH$^-$, denoted by species j, j=1, 2, 3, and 4, respectively. Let C_{10}, C_{20}, C_{30}, and C_{40} be the bulk

concentrations of these ions (mM), respectively, and C_0 the bulk concentration of KCl (mM).

Since pH=$-$log([H$^+$]$_0$/1000) with [H$^+$]$_0$ being the bulk molar concentration of H$^+$ (mM), C_{30}=10^{-pH+3}, C_{40}=10$^{-(14-pH)+3}$, C_{10}=$C_0$$-$10^{-pH+3}+10$^{-(14-pH)+3}$, and C_{20}=C_0 for pH$\geq$7; C_{30}=10^{-pH+3}, C_{40}=10$^{-(14-pH)+3}$, C_{10}=C_0, and C_{20}=C_0+10^{-pH+3}$-$10$^{-(14-pH)+3}$ for pH<7.

To fully describe the present problem, the following set of nonlinear, couple differential

equations need be solved simultaneously:

$$\nabla \cdot \mathbf{N}_j = \nabla \cdot [c_j\mathbf{u} - D_j(\nabla c_j + \frac{z_jFc_j}{RT}\nabla\phi)]=0 \qquad (2.2)$$

$$\nabla^2\phi = -\frac{\rho_e}{\varepsilon} = -\sum_{j=1}^{4}\frac{z_jFc_j}{\varepsilon} \qquad (2.3)$$

$\mathbf{N}_j$, c_j, D_j, and z_j are the flux density, the molar concentration, the diffusivity, and the valence of

ionic species j, respectively (j = 1, 2, 3, and 4). F, R, T, $\mathbf{u}$, and ϕ are Faraday constant, the

universal gas constant, the absolute temperature, the fluid velocity, and the electric potential,

respectively. ρ_e and ε are the space charge density of mobile ions and the permittivity of the

liquid phase, respectively.

Since the fluid flow in the present problem is in the creeping flow regime, the equations

49

governing the flow field at steady state can be described by

$$\nabla \cdot \mathbf{u} = 0 \tag{2.4}$$

$$\mu \nabla^2 \mathbf{u} - \nabla p - \rho_e \nabla \phi = \mathbf{0} \tag{2.5}$$

μ and p are the fluid viscosity and the hydrodynamic pressure, respectively.

Equations (2.2)-(2.5) need be solved subject to the following conditions: (i) The rigid nanochannel surface Ω_1 is non-slip (i.e., $\mathbf{u=0}$), impenetrable to ions (i.e., $\mathbf{n} \cdot \mathbf{N}_j = 0$, $\mathbf{n}$ is the unit outer normal vector), and has a pH-regulated charge density σ_s defined previously. (ii) The boundary Ω_2 of the computation domain is grounded, and an electric potential bias V is applied to its boundary Ω_3. All the ionic concentrations reach their bulk values on Ω_2 and Ω_3, ($c_j=C_{j0}$). A normal flow with no external pressure gradient (i.e., $p=0$) is specified on these two boundaries. (iii) There is no accumulated charge on the boundary Ω_4 of the computation domain ($\mathbf{n} \cdot \nabla \phi = 0$), the normal flux of ions vanishes on that surface (i.e., $\mathbf{n} \cdot \mathbf{N}_j = 0$), and it is slip. (iv) Electric potential, electric field, ionic concentration, and flow field are all continuous on the interface between the charged wall and liquid. (v) All the dependent variables are symmetric to the nanochannel axis.

The solution of Eqs. (2.2)-(2.5) can be used to evaluate the ionic current I through the nanochannel by integrating the normal component of the total ionic flux over a surface S perpendicular to the nanochannel axis

$$I = \int_S F(\sum_{j=1}^{4} z_j \mathbf{N}_j) \cdot \mathbf{n} \, dS \qquad (2.6)$$

2-3. Results and Discussion

A thorough numerical simulation is conducted to illustrate the influence of the parameters

key to the system under consideration on its ion transport behavior. These include the surface

curvature ($L_N/2h$), the base radii R_b, the bulk salt concentration C_0, and the solution pH. We

assume L_N=3000 nm, L_r=300 nm, R_r=300 nm, R_t=5 nm, and R_c=100 nm[61], Γ_t=1.5 nm^{-2}, and

pK_A=3 and pK_B=9[41, 53, 56], that is, the isoelectric point (IEP) is 6. In addition,

$\varepsilon = 6.95 \times 10^{-10}$ F/m, F=96500 C/mol, R=8.3145 J/(mol·K), $\mu = 10^{-3}$ Pa·s, and T=298.15 K. D_1(K$^+$),

D_2(Cl$^-$), D_3(H$^+$), and D_4(OH$^-$) are 1.957, 2.032, 9.312, and 5.26($\times 10^{-9}$) m^2/s, respectively. We

consider the case where $R_t \neq R_b$ and $L_N/2h_1 = L_N/2h_2 = L_N/2h$, with R_t=5 nm and R_b is either 15 nm

or 25 nm. Note that the orifice diameter of the cigar-like nanochannel varies along its axis, so are

the degree of EDL overlapping and the ionic distribution, yielding its ICR behavior. Since the

rectification factor R_f is usually defined at a voltage higher than 0.5 V, we choose

R_f=|I(−1V)/I(+1V)| to quantify the rectification characteristics.

Equations (2.2)-(2.5) are solved numerically subject to prespecified boundary conditions by

COMSOL (version 4.3a, http://www.comsol.com) operated in a high-performance cluster.

Quadratic, triangular elements are used and, if necessary, non-uniform elements with larger

51

number of elements are assigned locally. In our case, using a total number of 200000 mesh elements is sufficient for retrieving results that are sufficiently accurate and reliable.

2-3.1 Cation-Selective Nanochannel (pH 10)

Let us consider first the case where pH=10. In this case, since the nanochannel is negatively charged, it is generally cation-selective. Figure 2-2 shows the simulated current-voltage (I-V) curves under various conditions. As can be seen in this figure, there is a preference for ionic current at a negative applied potential bias at this level of pH so that the rectification factor R_f of the nanochannel is larger than unity for all the levels of the bulk salt concentration C_0 examined. Note that the higher the bulk salt concentration C_0 and the larger the base radii R_b the larger the ionic current is. Figure 2-2 also shows that the larger the ($L_N/2h$) the larger the ionic current. This is because the larger the ($L_N/2h$) the greater the inner space of the nanochannel so that a more amount of ions is able to diffuse through it, yielding a larger current. Due to the enrichment of ions inside the nanochannel, this phenomenon is more pronounced for $V<0$.

To explain the influences of the surface curvature ($L_N/2h$), the bulk salt concentration C_0, and the base radii R_b on the ICR behavior of a nanochannel, we plot the variations of R_f with $L_N/2h$ under various conditions at pH 10 in Figure 2-3. This figure reveals that for both values of R_b (15 and 25 nm), R_f increases monotonically with increasing ($L_N/2h$) at all the levels of C_0 examined, except at C_0=100 mM, where R_f shows a local maximum at $L_N/2h$=5. Note that both $R_f(R_b$=25

52

nm) and $R_f(R_b$=15 nm) are larger than unity, and for the same values of R_t and ($L_N/2h$), $R_f(R_b$=25 nm)$>R_f(R_b$=15 nm). This is because the larger the difference between R_t and R_b the greater the difference in the degree of electric double layer overlapping near the both nanochannel tip regions, and the more significant the ICR effect.

Figure 2-3 also reveals that R_f has a local maximum as the bulk salt concentration C_0 varies. This behavior was also reported previously for conical nanopores[54], and was explained by the rates of change in R_f and $I(V$=$\pm$1 V) with respect to C_0.

The ICR behavior observed in Figure 2-3 can be explained by the ionic conductivity and the strength of the electric field in the nanochannel. Letting λ_j be the molar conductivity of the jth ionic species, we define respectively the axial cross sectional averaged concentration $\overline{c_j}$ and the corresponding ionic conductivity G as [17]

$$\overline{c_j} = \frac{\int c_j dA}{\int dA}, \quad j = 1, 2, 3, 4 \tag{2.7}$$

and

$$G = \sum_{j=1}^{4} \overline{c_j} \lambda_j \tag{2.8}$$

Under the conditions considered, λ_1 (K$^+$), λ_2 (Cl$^-$), λ_3 (H$^+$), and λ_4 (OH$^-$) are 7.352$\times$10^{-3}, 7.654$\times$10^{-3}, 35$\times$10^{-3}, and 19.8$\times$10^{-3} S m^2 mol^{-1}, respectively. Note that the ionic current is proportional to G.

53

Figure 2-4 illustrates the variations in G for various combinations of C_0, ($L_N/2h$), and V; the corresponding axial variations in the cross sectional averaged strength of the electric field $E_{z,avg}$ are summarized in Figures S1−S4 of the Supporting Information. The latter reveals that $E_{z,avg}$ is appreciable only near the tip end of the nanochannel, where the effect of surface charge is more important. In addition, for both $V=\pm1$ V, the larger the ($L_N/2h$), the stronger the $E_{z,avg}$. Since the qualitative behaviors of both G and $E_{z,avg}$ at $R_b=15$ nm are similar to those at $R_b=25$ nm, those at $R_b=25$ nm are adopted for interpreting the observed ICR behavior seen in Figure 2-3.

Figure 2-4(a) reveals that if $C_0=1$ mM, the difference between $G(V=+1$ V) and $G(V=−1$ V) is relatively small for each level of ($L_N/2h$) so that R_f is close to unity. Note that as shown in Figure S1 of the Supporting Information, if $V=+1$ V, a local electric field with its direction opposite to that of the applied electric field is induced near the nanochannel tip. This phenomenon is more appreciable as ($L_N/2h$) gets smaller, implying that the smaller the ($L_N/2h$) the more important the effect of ion concentration polarization (ICP). Figure 2-4(b) indicates that the behavior of G at $C_0=10$ mM is similar to that at $C_0=1$ mM seen in Figure 2-4(a). That is, for both $V=\pm1$ V, G (and therefore, R_f) is insensitive to the variation in ($L_N/2h$). However, for each level of ($L_N/2h$), $G(V=−1$ V) is appreciably larger than $G(V=+1$ V), so that $R_f(C_0=10$ mM) is larger than $R_f(C_0=1$ mM). On the other hand, as illustrated in Figure S2 of the Supporting Information, the degree of increase in $E_{z,avg}$ as ($L_N/2h$) increases at $V=−1$ V is larger than that at $V=+1$ V so that R_f increases

54

with increasing $(L_N/2h)$.

As seen in Figure S3 of the Supporting Information that for both $V=\pm1$ V, the averaged axial electric field $E_{z,avg}$ near the nanochannel tip at $C_0=100$ mM increases with increasing $(L_N/2h)$. However, Figure 2-4(c) reveals that as $(L_N/2h)$ increases from 2 to 5, the position at which the local maximum of $G(V=-1$ V) occurs shifts towards the nanochannel tip end, where $E_{z,avg}$ has the largest value. This leads to a larger ionic current. In contrast, $G(V=+1$ V) varies inappreciably as $(L_N/2h)$ increases from 2 to 5, so is the corresponding ionic current. Therefore, R_f increases with increasing $(L_N/2h)$. If $(L_N/2h)$ is further raised from 5 to 11, the degree of increase in $E_{z,avg}(V=+1$ V) is larger than that in $E_{z,avg}(V=-1$ V), yielding a decrease in R_f. These explain the presence of a local maximum in R_f as $(L_N/2h)$ increases from 2 to 11.

Figure 2-4(d) reveals that at $C_0=500$ mM, $G(V=-1$ V) increases appreciably when $(L_N/2h)$ is raised from 2 to 11, but $G(V=+1$ V) follows the reverse trend. Since the ionic current is proportional to G, R_f also increases appreciably from 1.79 to 4.07.

To further examine the transport properties of the present cigar-shaped nanochannel, we evaluate its selectivity S defined below:

$$S = \frac{|I_+| - |I_-|}{|I_+| + |I_-|}, \qquad\qquad (2.9)$$
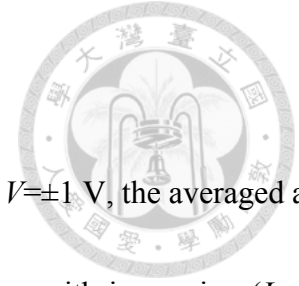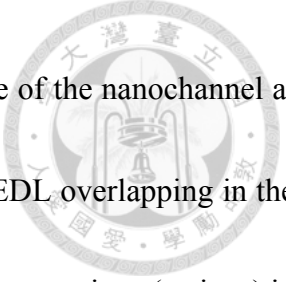
where $I_+=I_1+I_3$ and $I_-=I_2+I_4$ are the ionic current contributed by cations and that by anions, respectively. If $S>0$, a nanochannel is cation-selective; if $S<0$, it is anion-selective, and non-

55
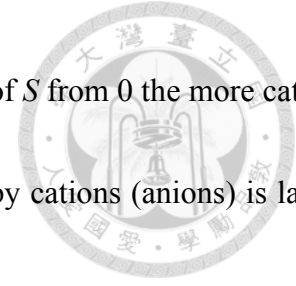
selective if $S=0$. For $S>0$ ($S<0$), the more appreciable the deviation of S from 0 the more cation-

(anion-) selective it is, implying that the ionic current contributed by cations (anions) is larger

than that that by anions (cations).

Figure 2-5 shows the simulated variation in the selectivity S as a function of the surface

curvature ($L_N/2h$) at pH 10. Since the pH is higher than the IEP (6) of the nanochannel, it is

negatively charged in this case, and therefore, cation-selective ($S>0$) and the ionic current is

mainly contributed by cations. The variation of S with ($L_N/2h$) at $V=+1$ V is more sensitive

than that at $V=-1$ V, and for the same nanochannel shape and bulk salt concentration, $S(V=+1$

V$)>S(V=-1$ V), in general. This is because the nanochannel is negatively charged at pH 10,

ion depletion occurs when $V=+1$ V. In this case EDL is thick and its overlapping is significant

so that the ionic current is mainly contributed by counterions (cations), yielding a large S.

Note that for the same applied voltage and surface curvature S increases with decreasing C_0,

and the nanochannel becomes more cation-selective. This is because the lower the C_0 the

thicker the EDL and the more significant its overlapping near the nanochannel tip region,

making it more difficult for coions to pass through so that counterions are enriched and coions

depleted, and S deviates more from zero. In addition, since EDL overlapping becomes less

significant as ($L_N/2h$) increases, for fixed values of V and C_0, S decreases as ($L_N/2h$) increases

from 2 to 11. A comparison between Figure 2-5(a) and Figure 2-5(b) reveals that $S(R_b=15$ nm)

is slightly larger than $S(R_b=25$ nm). This is because the internal space of the nanochannel at

R_b=15 nm is smaller than that at R_b=25 nm. Therefore, the effect of EDL overlapping in the

former is more significant than that in the latter so that the amount of counterions (cations) in

the former is greater than that in the latter. Note that both S and R_f are dominated mainly by

the conditions near the nanochannel tip region. This is because the factors key to the present

system, including the analyte size effect [54, 55, 62, 63], the influence of the radial electrical

double layer[62, 64], and the major part of the applied axial voltage drop[54, 55, 65, 66], are

most significant in that region and act together to determine the final device performance.

Since the tip size is fixed, S is insensitive to the variation in $(L_N/2h)$ in Figure 2-5, especially

at V=+1 V.

2-3.2 Anion-Selective Nanochannel (pH 4)

At pH 4 the nanochannel is positively charged, and therefore, anion-selective. In this case

Figure 2-6 reveals that there is a preference for ionic current at a positive applied potential

bias at this level of pH so that $0<R_f<1$ for all the levels of the bulk salt concentration C_0

examined. This figure also indicates that the higher the bulk salt concentration C_0 and the

larger the base radii R_b the greater the ionic current. In addition, the larger the surface

curvature $(L_N/2h)$ the larger the ionic current, which can be explained by the same reasoning

57

as that employed in the discussion of Figure 2-2.

Figure 2-7 summarizes the dependence of the rectification factor R_f on the surface

curvature ($L_N/2h$) under various conditions at pH 4. For the cases of both values of R_b assumed

(15 and 25 nm), R_f is seen to increase monotonically with increasing ($L_N/2h$) at all the levels

of C_0 considered. Note that both $R_f(R_b=25$ nm) and $R_f(R_b=15$ nm) are lower than unity, and

for the same values of R_t and ($L_N/2h$), $R_f(R_b=25$ nm)$<R_f(R_b=15$ nm). That is, the performance

of rectifying ionic current of a nanochannel having a larger R_b (25 nm) is better than that

having a smaller R_b (15 nm). This is because the larger the difference between R_t and R_b the

greater the difference in the degree of electric double layer overlapping near the nanochannel

tip regions, and therefore, the more significant the ICR effect. Figure 2-7 and Figure S5 of the

Supporting Information also suggest that R_f has a local minimum as the bulk salt concentration

C_0 varies.
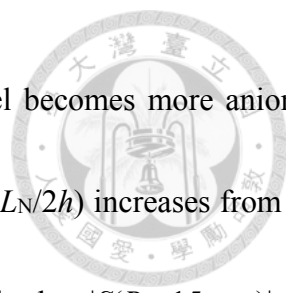
Figure 2-7 indicates that for the level of the bulk salt concentration considered, the larger

the ($L_N/2h$) the closer the R_f to unity, that is, the less significant the ICR effect. This can be

explained by Figure 2-8 and Figures S6-S9 of the Supporting Information. As seen in the latter

$E_{z,avg}$ is appreciable near the nanochannel tip region, where the effect of surface charge is most

important. In addition, for both $V=\pm 1$ V, the larger the ($L_N/2h$) the stronger the $E_{z,avg}$. Since

the qualitative behaviors of both G and $E_{z,avg}$ at $R_b=15$ nm in Figure 2-7 are similar to those at

R_b=25 nm, the results at R_b=25 nm shown in Figure 2-8 and Figures S6-S9 of the Supporting

Information are adopted for interpreting the observed ICR behavior seen in Figure 2-7.

Figures S6-S9 of the Supporting Information reveal that the degree of increase in the axial

electric field with increasing (L_N/2h) at V=−1 V is much more appreciable than that at V=+1

V, implying that tuning (L_N/2h) is more favorable to I(−1 V). The ionic conductivity at V=−1

V shown in Figure 2-8 suggests that it is insensitive to the variation in (L_N/2h). In contrast,

the ionic conductivity at V=+1 V decreases appreciably with increasing (L_N/2h). Therefore, at

pH 4 if (L_N/2h) is raised, the nanochannel favors I(−1 V), making R_f closer to unity (less

rectification effect).

To further investigate the ion transport behavior in the present cigar-shaped nanochannel,

we plot the selectivity S against the surface curvature (L_N/2h) under various conditions in

Figure 2-9.

Since the pH is lower than the IEP (6) of the nanochannel, it is positively charged so that

Cl^- and OH^- are attracted into it and K^+ and H^+ repelled out of it. Therefore, the ionic current

is mainly contributed by anions, yielding S<0. In this case, the larger the |S| the more the

nanochannel anion-selective. Figure 2-9 reveals that the variation of S with (L_N/2h) at V=−1

V is more sensitive than that at V=+1 V, and for the same nanochannel shape and bulk salt

concentration, |S(V=−1 V)|>|S(V=+1 V)|, in general. For the same applied voltage and surface
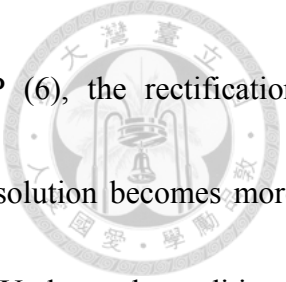
curvature, $|S|$ increases with decreasing C_0, that is, the nanochannel becomes more anion-selective. In addition, for fixed values of V and C_0, $|S|$ decreases as $(L_N/2h)$ increases from 2 to 11. A comparison between Figure 2-9(a) and 2-9(b) also reveals that $|S(R_b=15\ nm)|$ is slightly larger than $|S(R_b=25\ nm)|$. These behaviors are all result from the EDL overlapping inside the nanochannel. Note that if C_0 exceeds ca. 100 mM, $|S(V=-1\ V)|\cong|S(V=+1\ V)|$. This is because if C_0 exceeds that level, EDL is sufficiently thin so that its overlapping becomes insignificant, making the effect of surface charge unimportant, and therefore, $|S|$ is small.

2-3.3 Effect of pH Regulation

To further understand the electrokinetic ion transport phenomenon in the nanochannel functionalized with a pH-tunable zwitterionic surface, Figure 2-10 and Figure 2-11 illustrates the influence of pH on the current rectification factor R_f and the selectivity S. If pH is larger (smaller) than 6, R_f is larger (smaller) than unity, and S is generally larger (smaller) than zero, implying that the nanochannel is cation- (anion-) selective. This is because the IEP of the nanochannel is 6, so that it is negatively charged for pH>6, and positively charged for pH<6. If $S>0$ ($S<0$), the more noticeable deviation of S from zero represents the more significant cation- (anion-) selective.

Note that the variations of R_f and S with the surface curvature ($L_N/2h$) depend on the level

60

of pH. As the pH value is in the intermediate range near IEP (6), the rectification

characteristics almost vanish, indicated by $R_f \cong 1$. When the liquid solution becomes more

alkaline, the zwitterionic surface becomes more negatively charged. Under such conditions,

the preferential direction of the ionic current is pointed from the tip toward the base, indicated

by $R_f > 1$. If $C_0 = 100$ mM, R_f monotonously increases as the pH value increases from 6 to 10,

so is the charge density of the nanochannel. However, if C_0 is lowered to 10 mM, R_f shows a

local maximum at pH$\cong 8$. This is because raising the charge density has the effect of confining

the mobile ions in the EDL near the nanochannel surface, thereby reducing the

electromigrative ionic flux[58]. Note that at $C_0 = 10$ mM, R_f decreases monotonically with

increasing surface curvature ($L_N/2h$) for pH ranging from 6 to 8, but this trend is reversed for

pH ranging from 8 to 10. At $C_0 = 100$ mM, R_f decreases monotonically with increasing ($L_N/2h$)

for pH ranging from 6 to ca. 9.5. If pH exceeds ca. 9.5,

$R_f(L_N/2h=5) > R_f(L_N/2h=2) > R_f(L_N/2h=8) > R_f(L_N/2h=11)$. This can be explained by the

reasoning employed in the discussion of Figures 2-4 and S2-S3 and S10 of the Supporting

Information.

If pH is lower than IEP, the lower the pH the more the nanochannel is positively charged,

and the charge magnitude increases as pH decreases. Thus, the preferential direction of the

ionic current is reversed, indicated by $0 < R_f < 1$. However, the more the pH deviates from the

IEP the higher surface charge density. Therefore, R_f monotonously decreases as the pH value decreases from 6 to 3. Figure 2-10 reveals that R_f monotonously increases with increasing the surface curvature ($L_N/2h$) for pH ranging from 3 to 6. Note that at $C_0=10$ mM, $R_f(L_N/2h=2)>R_f(L_N/2h=11)>R_f(L_N/2h=8)>R_f(L_N/2h=5)$ near pH 2, but if C_0 is raised to 100 mM, R_f monotonously decreases with increasing ($L_N/2h$) near pH 2. These can also be explained by the reasoning employed in the discussion of Figures 2-8, and S7, S8, and S11 of the Supporting Information.

As the solution pH approaches the IEP of the nanochannel (i.e., 6), because its surface is only slightly charged it becomes non-selective, resulting in $S \cong 0$. If pH>IEP, S increases monotonically with increasing pH. This is because the more the pH deviates from the IEP the more complete the dissociation of the functional groups of zwitterionic surface, yielding a higher charge density, so that a more amount of counterions is attracted into the nanochannel, yielding a larger $|S|$. Figure 10(b) and (d) reveals that for the same nanochannel shape and solution pH, $S(V=+1$ V$)>S(V=-1$ V$)$, and for the same nanochannel shape, solution pH, and applied potential bias, $S(C_0=10$ mM$)>S(C_0=100$ mM$)$. In addition, the smaller the surface curvature of a nanochannel the better is its performance in selecting ionic species.
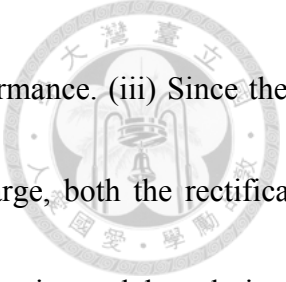
If pH<IEP, the nanochannel is anion-selective ($S<0$), and for the same nanochannel shape and solution pH, $S(V=+1$ V$)>S(V=-1$ V$)$. In this case, the lower the pH the better is the

62

performance of the nanochannel in selecting ionic species. However, if pH is too low, this trend

is reversed. Among the types of ion present in the liquid phase H^+ has the largest mobility, and

as pH decreases its presence becomes more significant, which is more pronounced especially

when the bulk salt concentration is low (C_0=10 mM). This is because as C_0 decreases less amount

of K^+ is attracted by the nanochannel surface, leading to an increase in the concentration of H^+.

2-4. Conclusions

Taking account of the effect of electroosmotic flow (EOF), the electrokinetic ion transport in a

cigar-shaped nanochannel modified with pH-tunable, zwitterionic functional groups is modeled

for the first time. Extending previous studies, where the surface of a nanochannel is assumed a

constant surface charge density, we assume that its charged conditions depend upon external

stimuli such as the solution pH and the bulk salt concentration, which is closer to reality. The ion

current rectification (ICR) and the ionic selectivity behaviors of the nanochannel are investigated

and the associated mechanisms interpreted. Based on a thorough numerical simulation we

conclude the following. (i) Depending upon the direction of the applied electric field, the

asymmetric geometry of the cigar-shaped nanochannel yields either ion enrichment or ion

depletion inside it. (ii) The degree of electric double layer overlapping inside the nanochannel is

influenced by the solution pH, the bulk salt concentration, the applied potential bias, the opening

63

radii and the shape of the nanochannel, so is the nanochannel performance. (iii) Since the ion transport in the nanochannel is governed mainly by its surface charge, both the rectification behavior and the ion selectivity depend highly on the bulk salt concentration and the solution pH. (iv) The axial variation of the ionic conductivity and that of the electric field in the nanochannel play a significant role. In particular, the nanochannel shape affects significantly the electric field, especially near the tip region, which eventually determines the performance of the nanochannel. (v) This study is an initial step for future work on structure-function relationships that will pave the way for designing membranes for specific purposes and providing valuable information for establishing smart nanochannel systems. These show great promise in many applications, including ionic gates/diodes, energy conversion, and drug controlled release.

References

[1] M. Ali, B. Yameen, R. Neumann, W. Ensinger, W. Knoll, O. Azzaroni, Biosensing and Supramolecular Bioconjugation in Single Conical Polymer Nanochannels. Facile Incorporation of Biorecognition Elements into Nanoconfined Geometries, Journal of the American Chemical Society, 130(2008) 16351-16357.

[2] Y.Q. Fu, H. Tokuhisa, L.A. Baker, Nanopore DNA sensors based on dendrimer-modified nanopipettes, Chemical Communications, 32(2009) 4877-4879.

[3] S. Umehara, M. Karhanek, R.W. Davis, N. Pourmand, Label-free biosensing with functionalized nanopipette probes, Proceedings of the National Academy of Sciences of the United States of America, 106(2009) 4611-4616.

[4] Y.L. Ying, J.J. Zhang, R. Gao, Y.T. Long, Nanopore-Based Sequencing and Detection of Nucleic Acids, Angewandte Chemie-International Edition, 52(2013) 13154-13161.

[5] N.A.W. Bell, U.F. Keyser, Specific Protein Detection Using Designed DNA Carriers and Nanopores, Journal of the American Chemical Society, 137(2015) 2035-2041.

[6] I. Vlassiouk, Z.S. Siwy, Nanofluidic diode, Nano Letters, 7(2007) 552-556.

[7] E.B. Kalman, I. Vlassiouk, Z.S. Siwy, Nanofluidic bipolar transistors, Advanced Materials, 20(2008) 293-297.

[8] M. Ali, P. Ramirez, S. Mafe, R. Neumann, W. Ensinger, A pH-Tunable Nanofluidic

65

Diode with a Broad Range of Rectifying Properties, ACS Nano, 3(2009) 603-608.

[9] M. Ali, S. Mafe, P. Ramirez, R. Neumann, W. Ensinger, Logic Gates Using Nanofluidic

Diodes Based on Conical Nanopores Functionalized with Polyprotic Acid Chains,

Langmuir, 25(2009) 11993-11997.

[10] X.Z. Jin, N.R. Aluru, Gated transport in nanofluidic devices, Microfluidics and

Nanofluidics, 11(2011) 297-306.

[11] C.Y. Li, F.X. Ma, Z.Q. Wu, H.L. Gao, W.T. Shao, K. Wang, et al., Solution-pH-

Modulated Rectification of Ionic Current in Highly Ordered Nanochannel Arrays Patterned

with Chemical Functional Groups at Designed Positions, Advanced Functional Materials,

23(2013) 3836-3844.

[12] K. Xiao, G.H. Xie, P. Li, Q. Liu, G.L. Hou, Z. Zhang, et al., A Biomimetic Multi-

Stimuli-Response Ionic Gate Using a Hydroxypyrene Derivation-Functionalized

Asymmetric Single Nanochannel, Advanced Materials, 26(2014) 6560-6565.

[13] S.F. Buchsbaum, G. Nguyen, S. Howorka, Z.S. Siwy, DNA-Modified Polymer Pores

Allow pH- and Voltage-Gated Control of Channel Flux, Journal of the American Chemical

Society, 136(2014) 9902-9905.

[14] Q. Liu, K. Xiao, L.P. Wen, H. Lu, Y.H. Liu, X.Y. Kong, et al., Engineered Ionic Gates

for Ion Conduction Based on Sodium and Potassium Activated Nanochannels, Journal of

the American Chemical Society, 137(2015) 11976-11983.

[15] M.Y. Liu, H.C. Zhang, K. Li, L.P. Heng, S.T. Wang, Y. Tian, et al., A Bio-inspired

Potassium and pH Responsive Double-gated Nanochannel, Advanced Functional

Materials, 25(2015) 421-426.

[16] H.C. Zhang, X. Hou, J. Hou, L. Zeng, Y. Tian, L. Li, et al., Synthetic Asymmetric-

Shaped Nanodevices with Symmetric pH-Gating Characteristics, Advanced Functional

Materials, 25(2015) 1102-1110.

[17] L.H. Yeh, C. Hughes, Z.P. Zeng, S.Z. Qian, Tuning Ion Transport and Selectivity by a

Salt Gradient in a Charged Nanopore, Analytical Chemistry, 86(2014) 2681-2686.

[18] L. Luo, S.R. German, W.J. Lan, D.A. Holden, T.L. Mega, H.S. White, Resistive-Pulse

Analysis of Nanoparticles, in: R.G. Cooks, J.E. Pemberton (Eds.), Annual Review of

Analytical Chemistry, 7(2014) 513-535.

[19] D.G. Haywood, A. Saha-Shah, L.A. Baker, S.C. Jacobson, Fundamental Studies of

Nanofluidics: Nanopores, Nanochannels, and Nanopipets, Analytical Chemistry, 87(2015)

172-187.

[20] Z.D. Harms, D.G. Haywood, A.R. Kneller, L. Selzer, A. Zlotnick, S.C. Jacobson,

Single-Particle Electrophoresis in Nanochannels, Analytical Chemistry, 87(2015) 699-705.

[21] Y.H. Qiu, I. Vlassiouk, Y.F. Chen, Z.S. Siwy, Direction Dependence of Resistive-Pulse

Amplitude in Conically Shaped Mesopores, Analytical Chemistry, 88(2016) 4917-4925.

[22] E. Weatherall, P. Hauer, R. Vogel, G.R. Willmott, Pulse Size Distributions in Tunable Resistive Pulse Sensing, Analytical Chemistry, 88(2016) 8648-8656.

[23] Y.H. Qiu, C.Y. Lin, P. Hinkle, T.S. Plett, C. Yang, J.V. Chacko, et al., Highly Charged Particles Cause a Larger Current Blockage in Micropores Compared to Neutral Particles, ACS Nano, 10(2016) 8413-8422.

[24] J.P. Hsu, S.C. Lin, C.Y. Lin, S. Tseng, Power generation by a pH-regulated conical nanopore through reverse electrodialysis, Journal of Power Sources, 366(2017) 169-177.

[25] Y. Hou, R. Vidu, P. Stroeve, Solar Energy Storage Methods, Industrial & Engineering Chemistry Research, 50(2011) 8954-8964.

[26] J. Gao, W. Guo, D. Feng, H.T. Wang, D.Y. Zhao, L. Jiang, High-Performance Ionic Diode Membrane for Salinity Gradient Power Generation, Journal of the American Chemical Society, 136(2014) 12265-12272.

[27] S.J. Kim, S.H. Ko, K.H. Kang, J. Han, Direct seawater desalination by ion concentration polarization, Nature Nanotechnology, 5(2010) 297-301.

[28] M. Heiranian, A.B. Farimani, N.R. Aluru, Water desalination with a single-layer MoS2 nanopore, Nature Communications, 6(2015) 8616.

[29] A.S. Hoffman, The origins and evolution of "controlled" drug delivery systems,

68

Journal of Controlled Release, 132(2008) 153-163.

[30] S. Herzig, J. Neumann, Effects of serine/threonine protein phosphatases on ion

channels in excitable membranes, Physiological Reviews, 80(2000) 173-210.

[31] D.C. Gadsby, Ion transport - Spot the difference, Nature, 427(2004) 795-797.

[32] D.C. Gadsby, Ion channels versus ion pumps: the principal difference, in principle,

Nature Reviews Molecular Cell Biology, 10(2009) 344-352.

[33] N. Reyes, D.C. Gadsby, Ion permeation through the Na+,K+-ATPase, Nature,

443(2006) 470-474.

[34] J. Xu, D.A. Lavan, Designing artificial cells to harness the biological ion

concentration gradient, Nature Nanotechnology, 3(2008) 666-670.

[35] A. Siria, P. Poncharal, A.L. Biance, R. Fulcrand, X. Blase, S.T. Purcell, et al., Giant

osmotic energy conversion measured in a single transmembrane boron nitride nanotube,

Nature, 494(2013) 455-458.

[36] S. Tseng, Y.M. Li, C.Y. Lin, J.P. Hsu, Salinity gradient power: influences of

temperature and nanopore size, Nanoscale, 8(2016) 2350-2357.

[37] R.B. Schoch, J.Y. Han, P. Renaud, Transport phenomena in nanofluidics, Reviews of

Modern Physics, 80(2008) 839-883.

[38] Z.S. Siwy, Ion-current rectification in nanopores and nanotubes with broken

symmetry, Advanced Functional Materials, 16(2006) 735-746.

[39] H.S. White, A. Bund, Ion current rectification at nanopores in glass membranes, Langmuir, 24(2008) 2212-2218.

[40] I. Vlassiouk, S. Smirnov, Z. Siwy, Ionic selectivity of single nanochannels, Nano Letters, 8(2008) 1978-1985.

[41] Z.P. Zeng, L.H. Yeh, M.K. Zhang, S.Z. Qian, Ion transport and selectivity in biomimetic nanopores with pH-tunable zwitterionic polyelectrolyte brushes, Nanoscale, 7(2015) 17020-17029.

[42] S.J. Kim, Y.C. Wang, J.H. Lee, H. Jang, J. Han, Concentration polarization and nonlinear electrokinetic flow near a nanofluidic channel, Phys Rev Lett, 99(2007) 044501.

[43] L.H. Yeh, M. Zhang, S. Qian, J.P. Hsu, S. Tseng, Ion Concentration Polarization in Polyelectrolyte-Modified Nanopores, Journal of Physical Chemistry C, 116(2012) 8672-8677.

[44] L.H. Yeh, M.K. Zhang, S.W. Joo, S. Qian, J.P. Hsu, Controlling pH-Regulated Bionanoparticles Translocation through Nanopores with Polyelectrolyte Brushes, Analytical Chemistry, 84(2012) 9615-9622.

[45] J.P. Hsu, T.W. Lin, C.Y. Lin, S. Tseng, Salt-Dependent Ion Current Rectification in Conical Nanopores: Impact of Salt Concentration and Cone Angle, Journal of Physical

Chemistry C, 121(2017) 28139-28147.

[46] R. Kwak, S.J. Kim, J. Han, Continuous-Flow Biomolecule and Cell Concentrator by

Ion Concentration Polarization, Analytical Chemistry, 83(2011) 7348-7355.

[47] G. Perez-Mitta, A.G. Albesa, M.E.T. Molares, C. Trautmann, O. Azzaroni, The

Influence of Divalent Anions on the Rectification Properties of Nanofluidic Diodes:

Insights from Experiments and Theoretical Simulations, Chemphyschem, 17(2016) 2718-

2725.

[48] M. Ali, P. Ramirez, H.Q. Nguyen, S. Nasir, J. Cervera, S. Mafe, et al., Single Cigar-

Shaped Nanopores Functionalized with Amphoteric Amino Acid Chains: Experimental and

Theoretical Characterization, ACS Nano, 6(2012) 3631-3640.

[49] C.Y. Lin, J.P. Hsu, L.H. Yeh, Rectification of ionic current in nanopores functionalized

with bipolar polyelectrolyte brushes, Sensors and Actuators B-Chemical, 258(2018) 1223-

1229.

[50] J.Y. Lin, C.Y. Lin, J.P. Hsu, S. Tseng, Ionic Current Rectification in a pH-Tunable

Polyelectrolyte Brushes Functionalized Conical Nanopore: Effect of Salt Gradient,

Analytical Chemistry, 88(2016) 1176-1187.

[51] D. Woermann, Electrochemical transport properties of a cone-shaped nanopore:

revisited, Physical Chemistry Chemical Physics, 6(2004) 3130-3132.
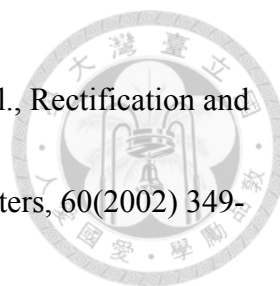
[52] Z. Siwy, Y. Gu, H.A. Spohr, D. Baur, A. Wolf-Reber, R. Spohr, et al., Rectification and voltage gating of ion currents in a nanofabricated pore, Europhysics Letters, 60(2002) 349-355.

[53] J.Y. Jung, P. Joshi, L. Petrossian, T.J. Thornton, J.D. Posner, Electromigration Current Rectification in a Cylindrical Nanopore Due to Asymmetric Concentration Polarization, Analytical Chemistry, 81(2009) 3128-3133.

[54] J. Cervera, B. Schiedt, R. Neumann, S. Mafe, P. Ramirez, Ionic conduction, rectification, and selectivity in single conical nanopores, Journal of Chemical Physics, 124(2006) 104706.

[55] P. Ramirez, P.Y. Apel, J. Cervera, S. Mafe, Pore structure and function of synthetic nanopores with fixed charges: tip shape and rectification properties, Nanotechnology, 19(2008) 315707.

[56] J.P. Hsu, H.H. Wu, C.Y. Lin, S. Tseng, Ion Current Rectification Behavior of Bioinspired Nanopores Having a pH-Tunable Zwitterionic Surface, Analytical Chemistry, 89(2017) 3952-3958.

[57] D.H. Lin, C.Y. Lin, S. Tseng, J.P. Hsu, Influence of electroosmotic flow on the ionic current rectification in a pH-regulated, conical nanopore, Nanoscale, 7(2015) 14023-14031.

[58] Z.P. Zeng, Y. Ai, S.Z. Qian, pH-regulated ionic current rectification in conical

nanopores functionalized with polyelectrolyte brushes, Physical Chemistry Chemical

Physics, 16(2014) 2465-2474.

[59] W. Guo, H.W. Xia, F. Xia, X. Hou, L.X. Cao, L. Wang, et al., Current Rectification in

Temperature-Responsive Single Nanopores, Chemphyschem, 11(2010) 859-864.

[60] P.Y. Apel, I.V. Blonskaya, S.N. Dmitriev, T.I. Mamonova, O.L. Orelovitch, B.

Sartowska, et al., Surfactant-controlled etching of ion track nanopores and its practical

applications in membrane technology, Radiation Measurements, 43(2008) S552-S559.

[61] H.C. Zhang, X. Hou, L. Zeng, F. Yang, L. Li, D.D. Yan, et al., Bioinspired Artificial

Single Ion Pump, Journal of the American Chemical Society, 135(2013) 16102-16110.

[62] S. Umehara, N. Pourmand, C.D. Webb, R.W. Davis, K. Yasuda, M. Karhanek, Current

rectification with poly-L-lysine-coated quartz nanopipettes, Nano Letters, 6(2006) 2486-

2492.

[63] E.A. Heins, Z.S. Siwy, L.A. Baker, C.R. Martin, Detecting single porphyrin molecules

in a conically shaped synthetic nanopore, Nano Letters, 5(2005) 1824-1829.

[64] M. Ali, B. Schiedt, K. Healy, R. Neumann, A. Ensinger, Modifying the surface charge

of single track-etched conical nanopores in polyimide, Nanotechnology, 19(2008) 085713.

[65] M.L. Kovarik, S.C. Jacobson, Integrated nanopore/microchannel devices for ac

electrokinetic trapping of particles, Analytical Chemistry, 80(2008) 657-664.

[66] S. Lee, Y.H. Zhang, H.S. White, C.C. Harrell, C.R. Martin, Electrophoretic capture and detection of nanoparticles at the opening of a membrane pore using scanning electrochemical microscopy, Analytical Chemistry, 76(2004) 6108-6115.
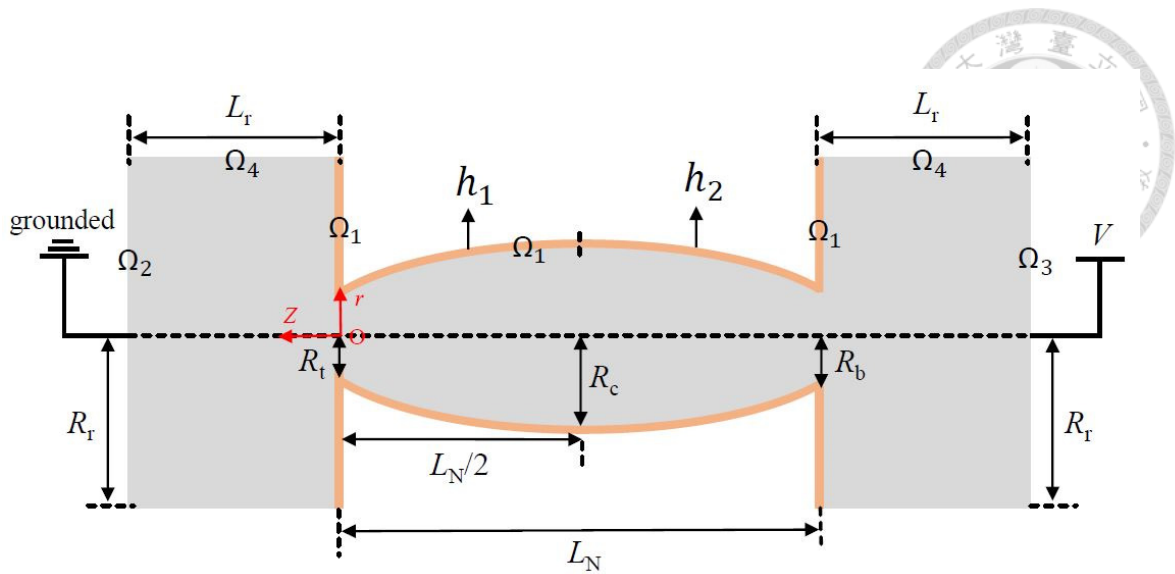
Figure 2-1. Schematic representation of the cigar-like nanochannel considered. r, θ, z, are the cylindrical coordinates adopted with the origin at the tip end center of the nanochannel, which is axial symmetry. Ω_1 denotes the inner and outer surface of the nanochannel, Ω_2 (Ω_3) the surface of a computational domain perpendicular to the nanochannel axis in the tip (base) end reservoir, and Ω_4 the surface of the computational domain parallel to the nanochannel axis in both reservoirs. A potential bias V is applied on one reservoir, and the other reservoir grounded (0 V). The cylindrical coordinates (r, θ, z) with its origin at the nanochannel tip end center are adopted.

75
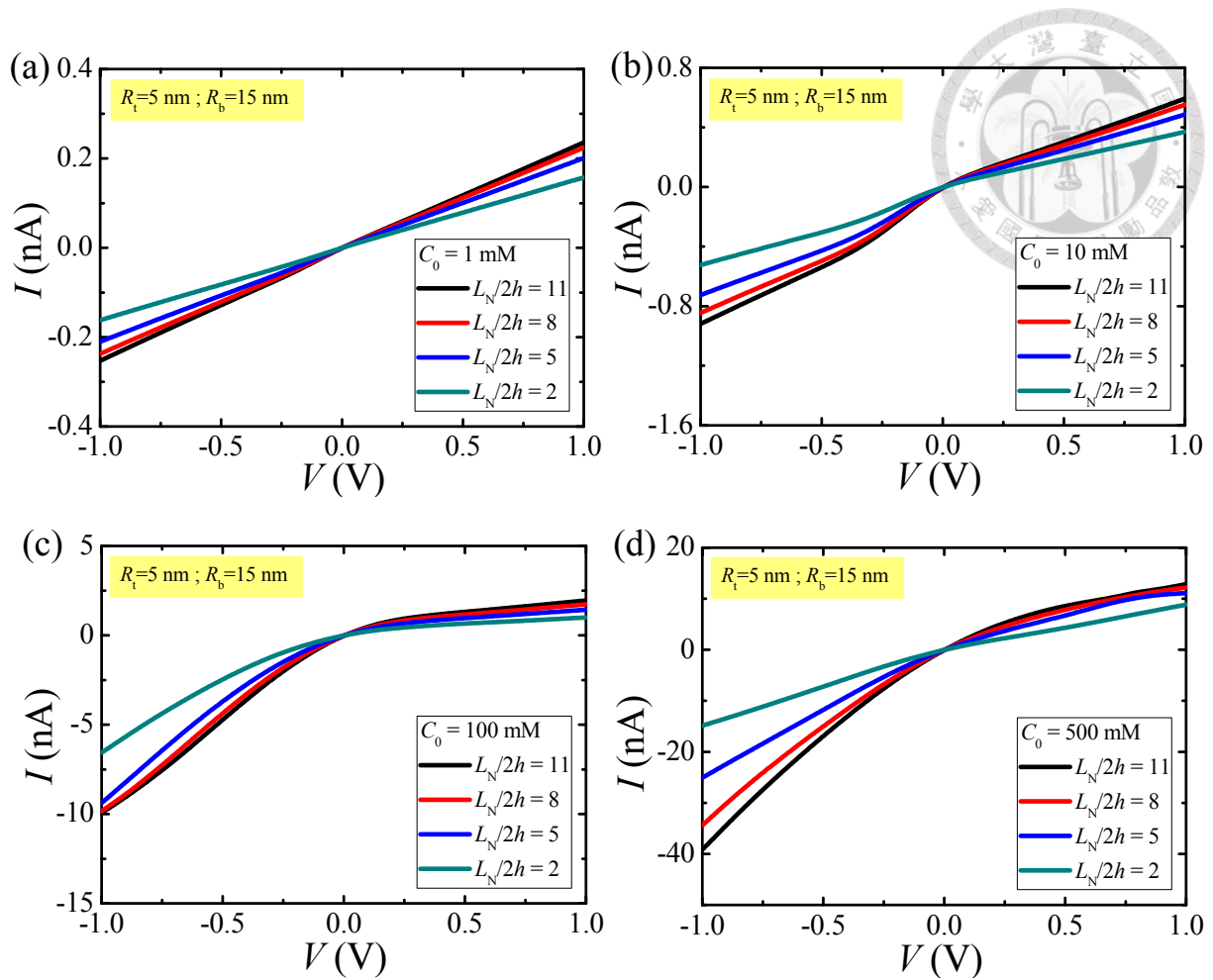
Figure 2-2(a)-(d). Simulated $I-V$ curves for various combinations of C_0 and $(L_N/2h)$ at pH

10 and R_t=5 nm. R_b is 15 nm in (a)-(d). C_0=1 mM in (a), C_0=10 mM in (b), C_0=100 mM in
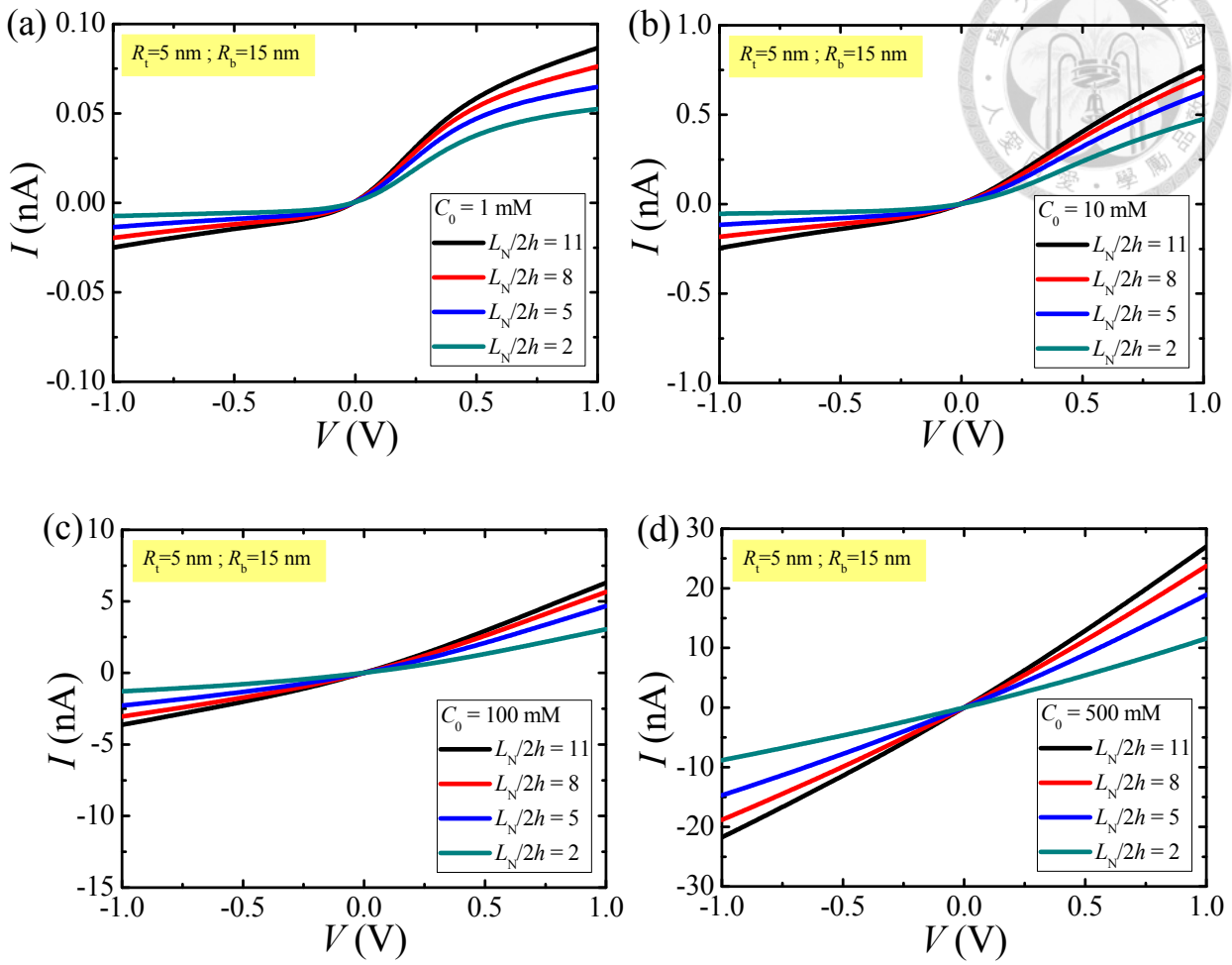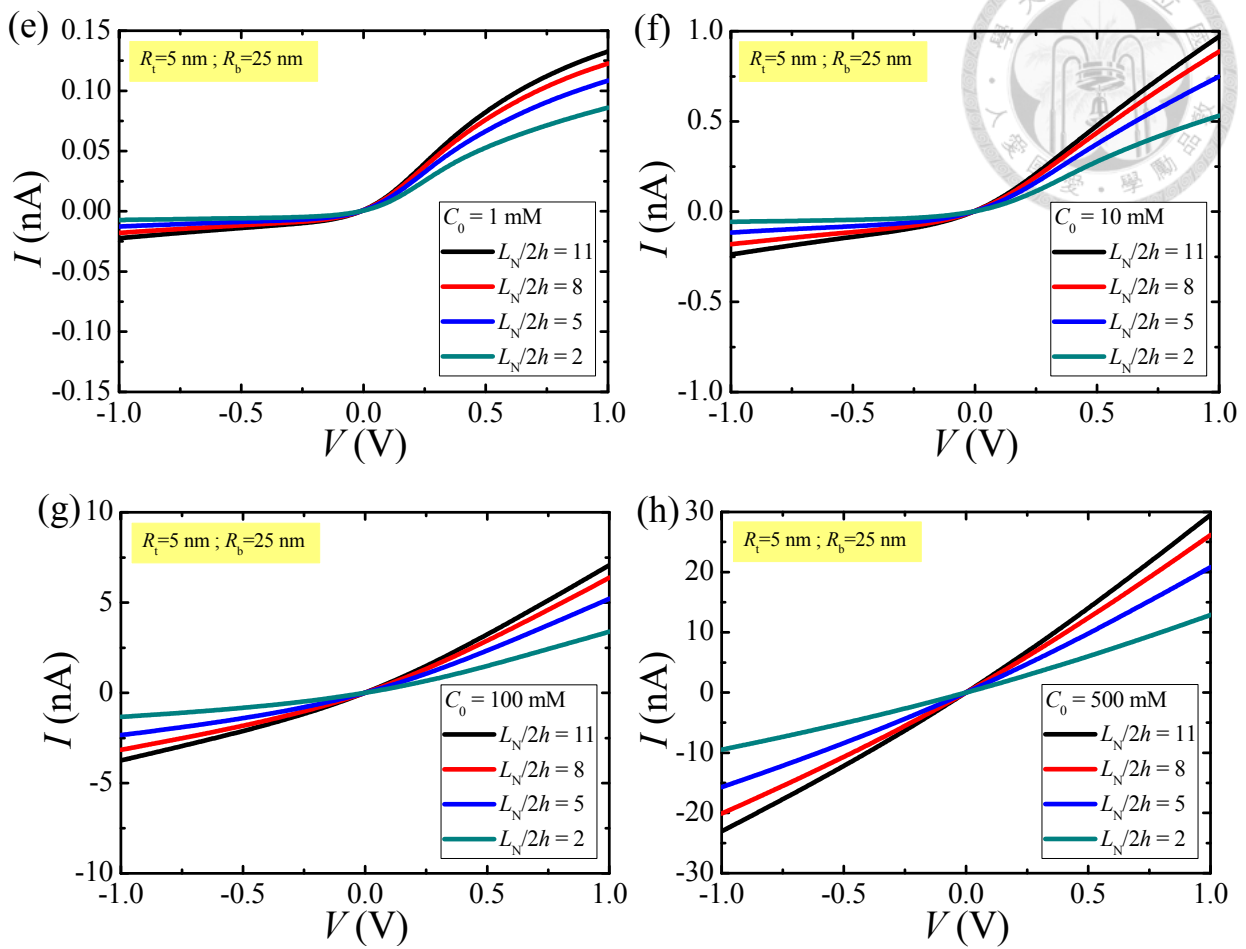
(c), and C_0=500 mM in (d).

76
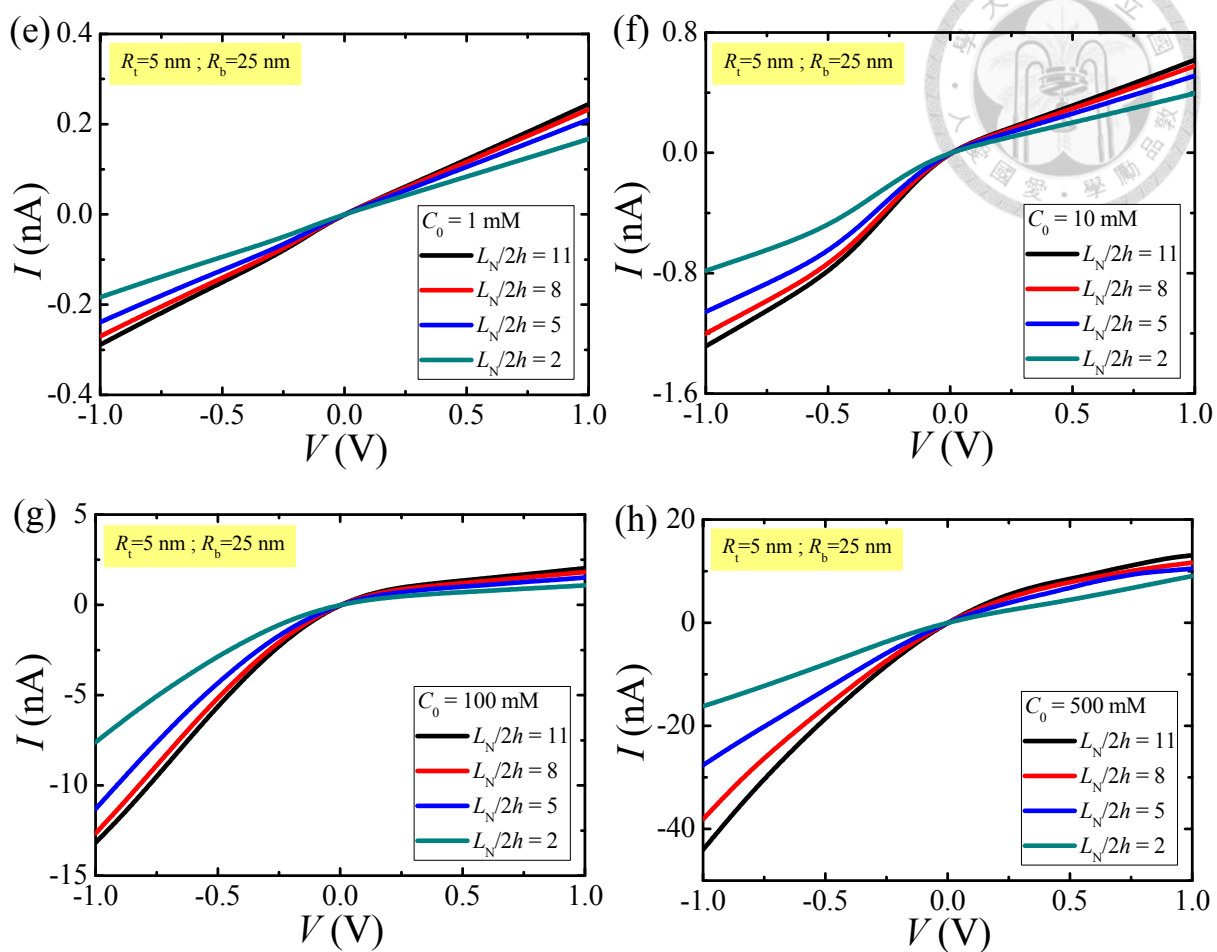
Figure 2-2(e)-(h). Simulated $I-V$ curves for various combinations of C_0 and $(L_N/2h)$ at pH

10 and R_t=5 nm. R_b is 25 nm in (e)-(h). C_0=1 mM in (e), C_0=10 mM in (f), C_0=100 mM in
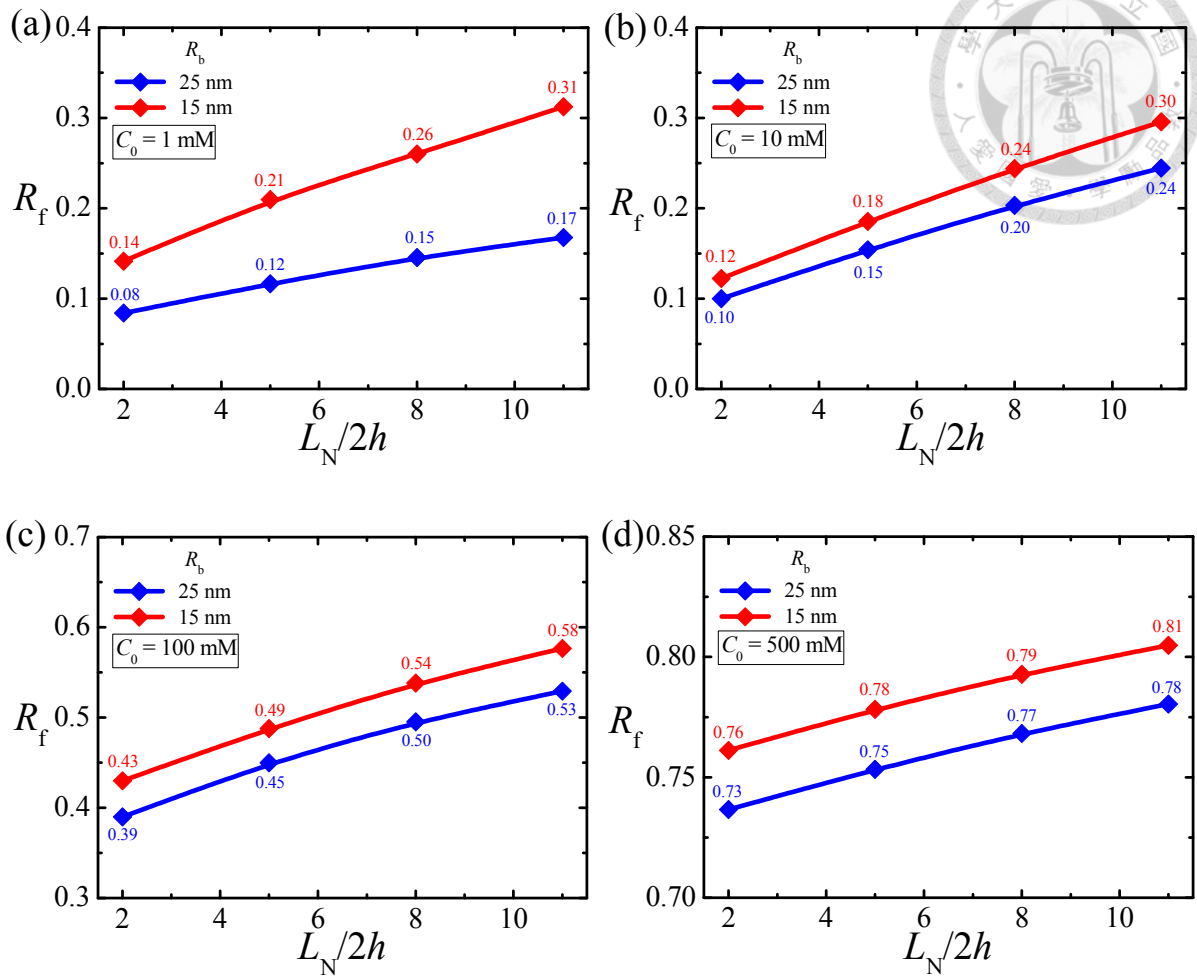
(g), and C_0=500 mM in (h).
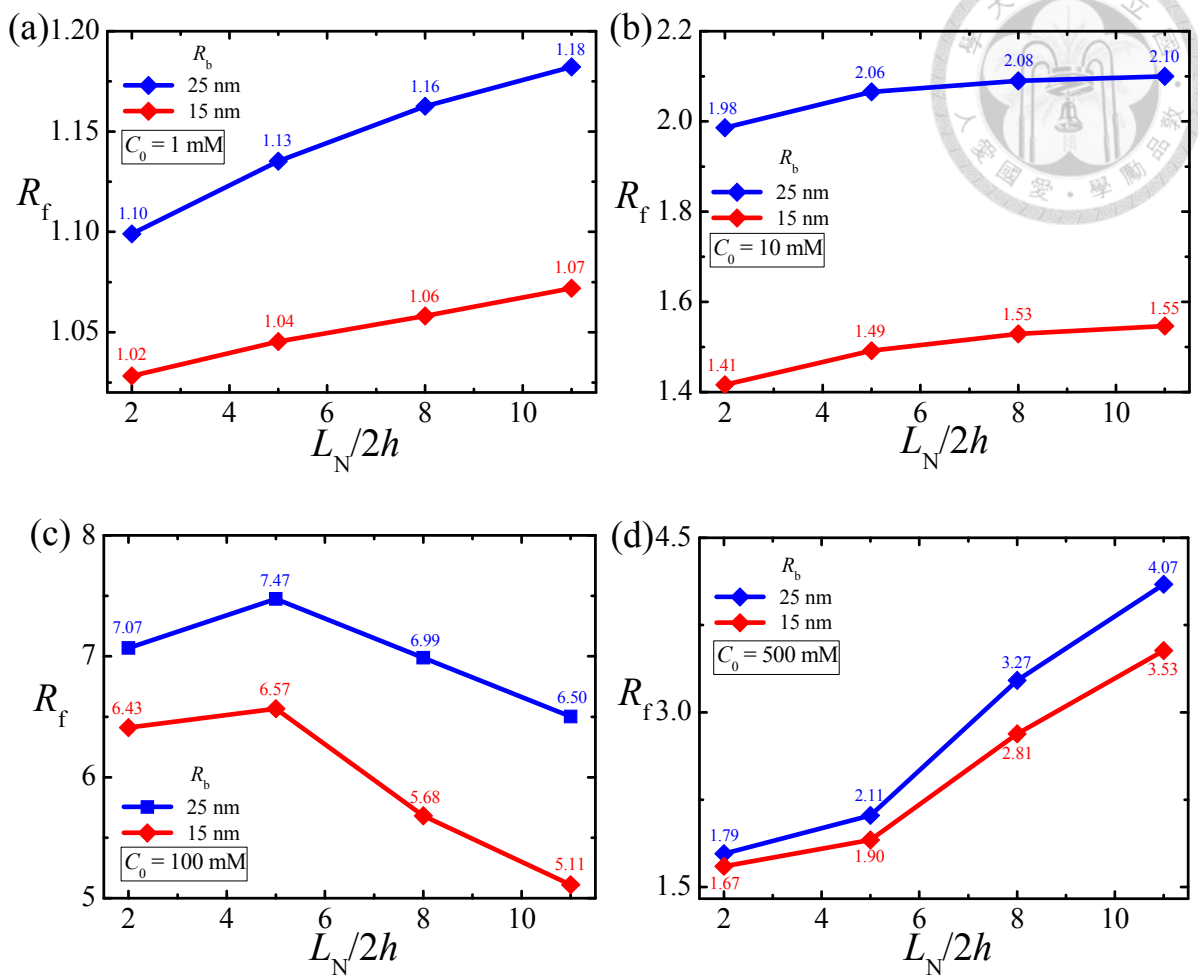
Figure 2-3(a)-(d). Variation of R_f with ($L_N/2h$) for various combinations of C_0 and R_b at

pH 10 and R_t=5 nm. (a) C_0=1 mM, (b) C_0=10 mM, (c) C_0=100 mM, and (d) C_0=500 mM.
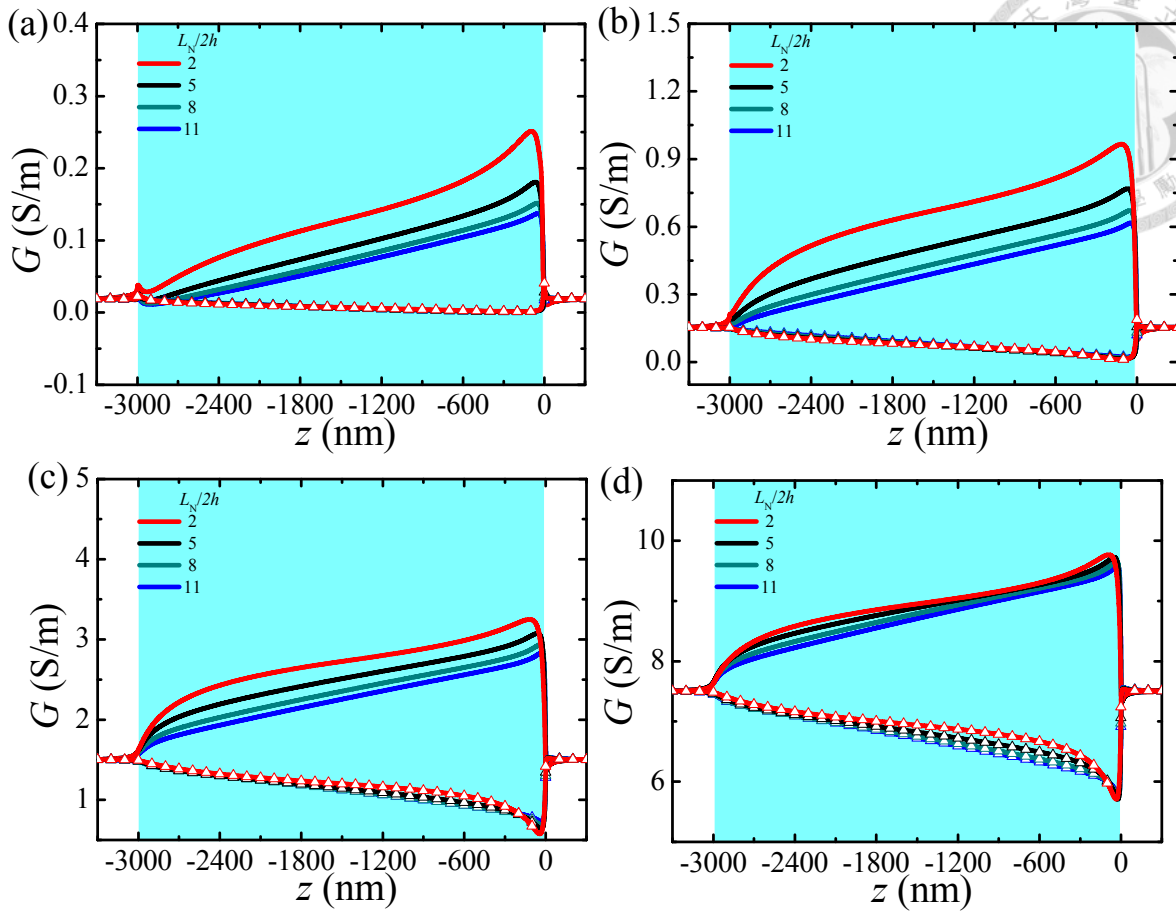
78
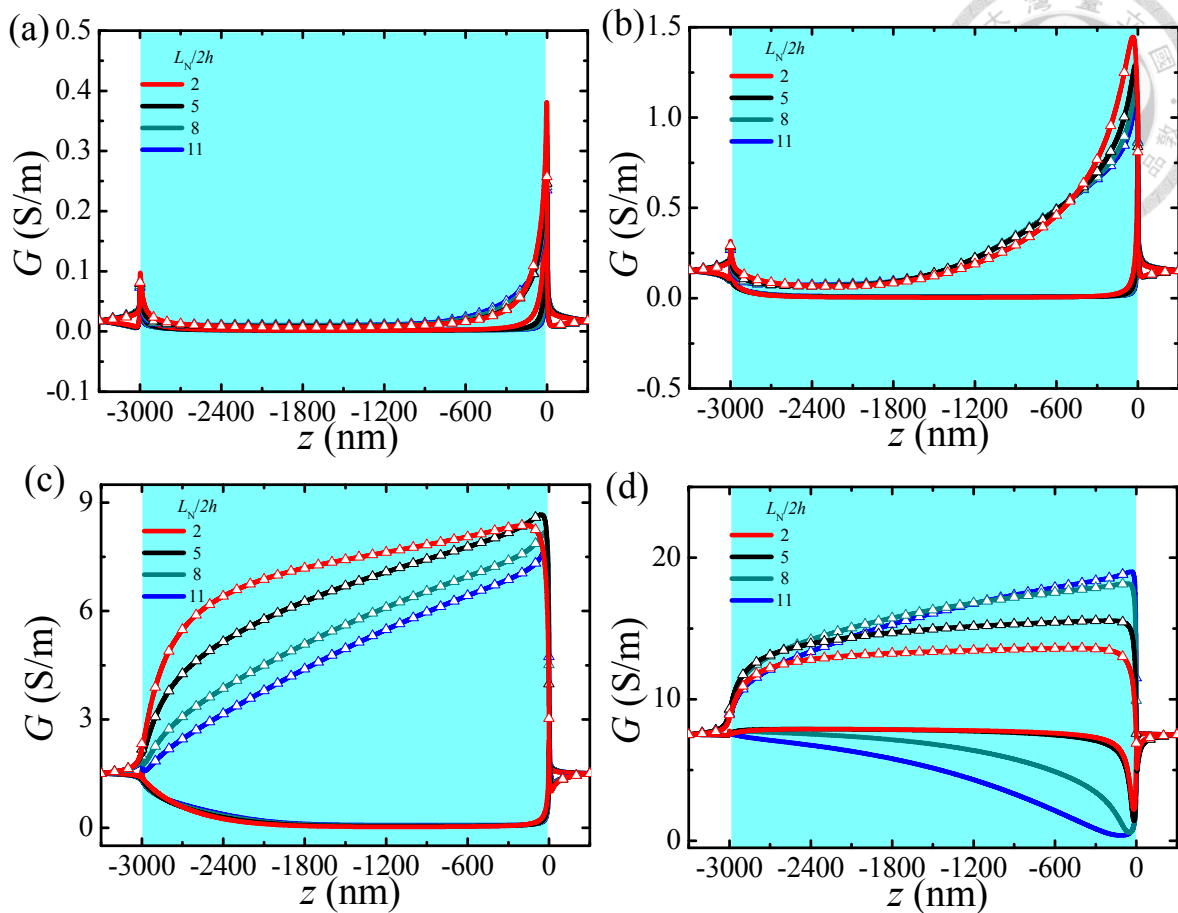
Figure 2-4(a)-(d). Axial variation in the cross sectional averaged ionic conductivity G at

pH 10, R_t=5 nm and R_b=25 nm for various levels of bulk salt concentration C_0. (a) C_0=1

mM, (b) C_0=10 mM, (c) C_0=100 mM, and (d) C_0=500 mM. Solid curves: V=+1 V; solid

curves with discrete symbols: V=−1 V. Shaded region denotes the nanochannel interior.
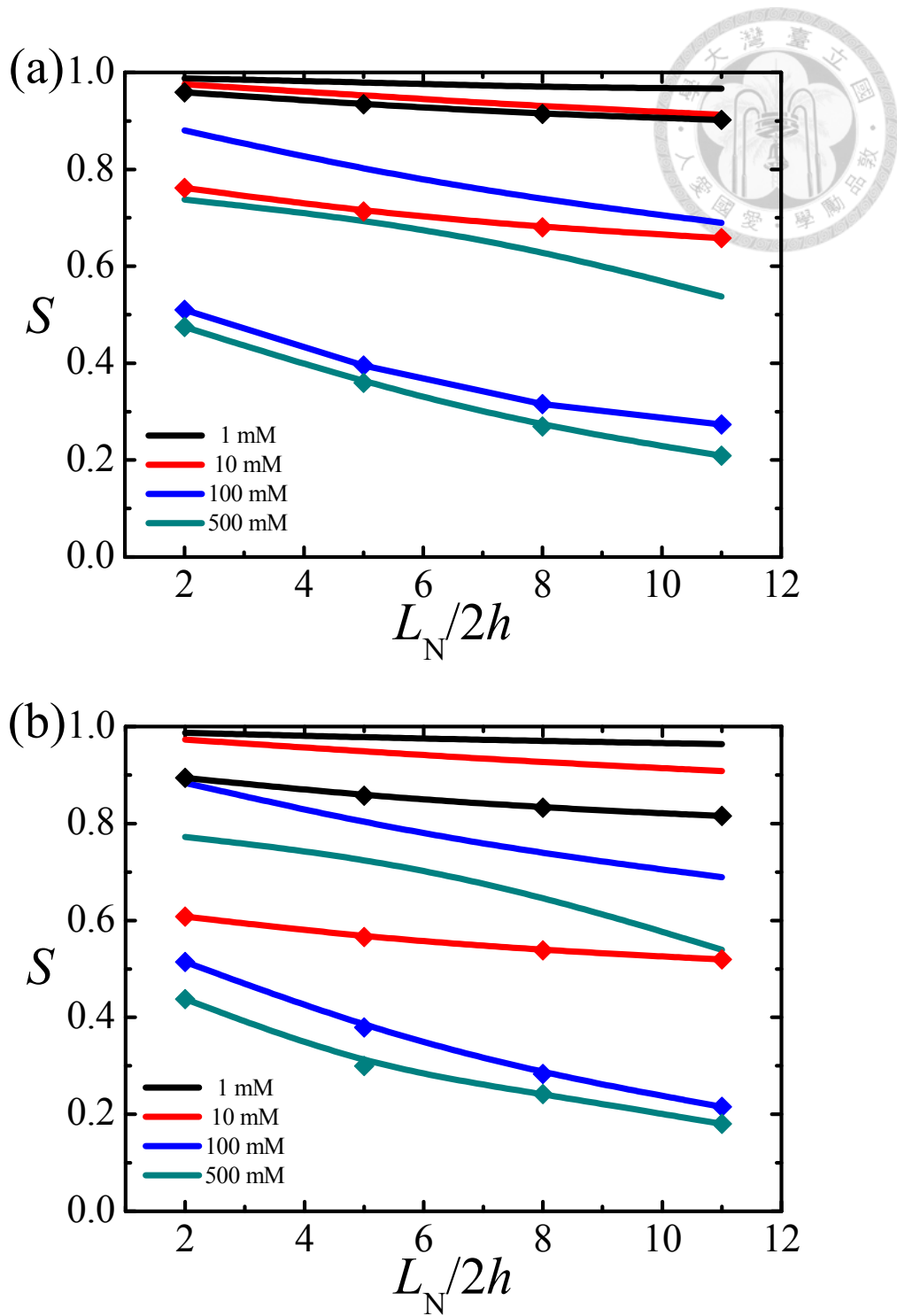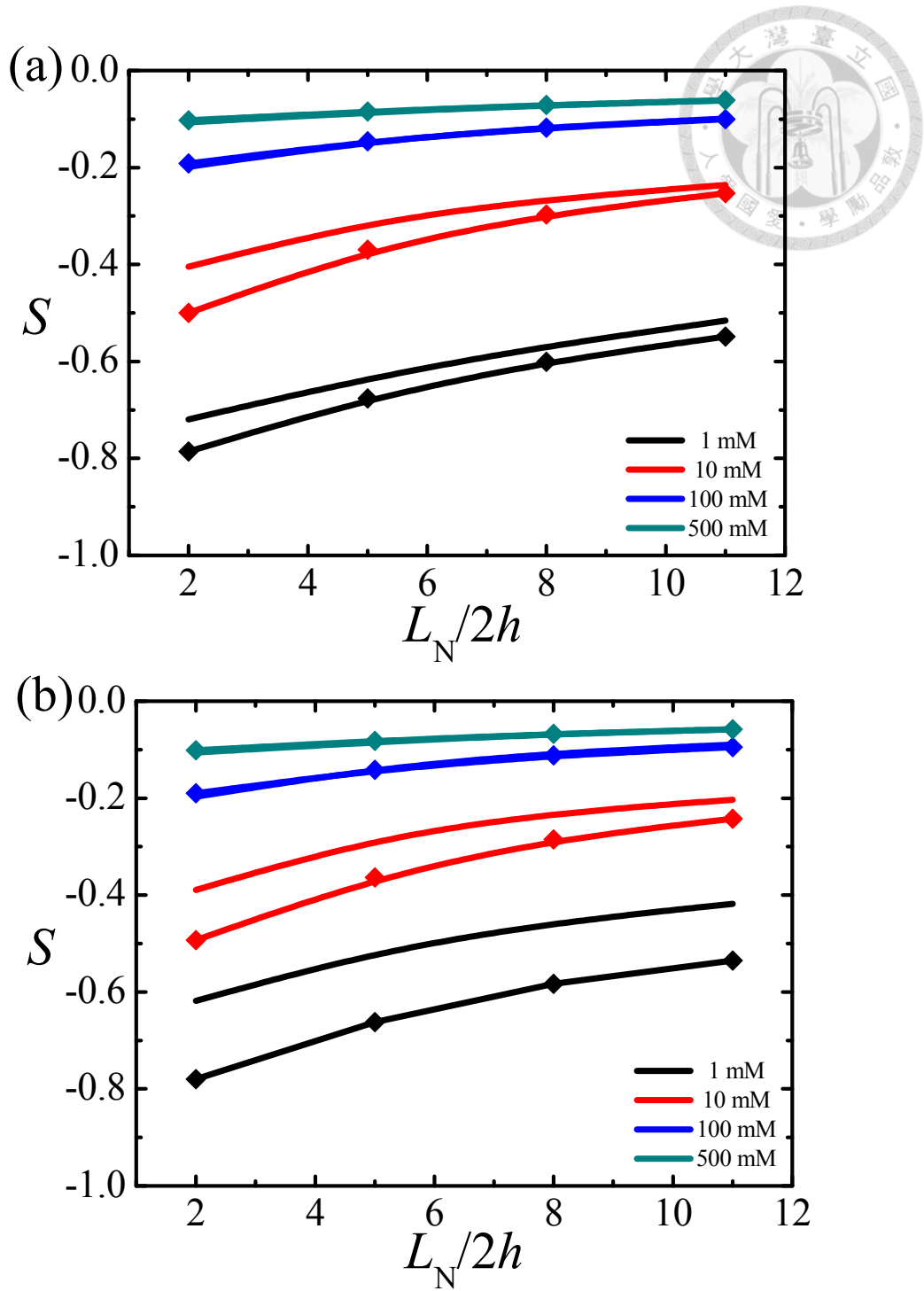
Figure 2-5. Variation in the selectivity S with the surface curvature ($L_N/2h$) at pH 10 and

R_t=5 nm for R_b=15 nm, (a), and R_b=25 nm, (b). Solid curve: V=+1 V; solid curve with

discrete symbols: V=−1 V.

Figure 2-6(a)-(d). Simulated $I-V$ curves for various combinations of C_0 and $(L_N/2h)$ at pH

4 and R_t=5 nm. R_b is 15 nm in (a)-(d). C_0=1 mM in (a), C_0=10 mM in (b), C_0=100 mM in

(c), and C_0=500 mM in (d).

81

Figure 2-6(e)-(h). Simulated $I-V$ curves for various combinations of C_0 and $(L_N/2h)$ at pH

4 and R_t=5 nm. R_b is 25 nm in (e)-(h). C_0=1 mM in (e), C_0=10 mM in (f), C_0=100 mM in

(g), and C_0=500 mM in (h).

82

Figure 2-7(a)-(d). Variation of R_f with ($L_N/2h$) for various combinations of C_0 and R_b at

pH 4 and R_t=5 nm. (a) C_0=1 mM, (b) C_0=10 mM, (c) C_0=100 mM, and (d) C_0=500 mM.

Figure 2-8(a)-(d). Axial variation in the cross sectional averaged ionic conductivity G at

pH 4, R_t=5 nm and R_b=25 nm for various levels of bulk salt concentration C_0. (a) C_0=1

mM, (b) C_0=10 mM, (c) C_0=100 mM, and (d) C_0=500 mM. Solid curves: V=+1 V; solid

curves with discrete symbols: V=−1 V. Shaded region denotes the nanochannel interior.

84

Figure 2-9. Variation in the selectivity S with the surface curvature ($L_N/2h$) at pH 4 and R_t=5

nm for R_b=15 nm, (a), and R_b=25 nm, (b). Solid curve: V=+1 V; solid curve with discrete

symbols: V=−1 V.

85
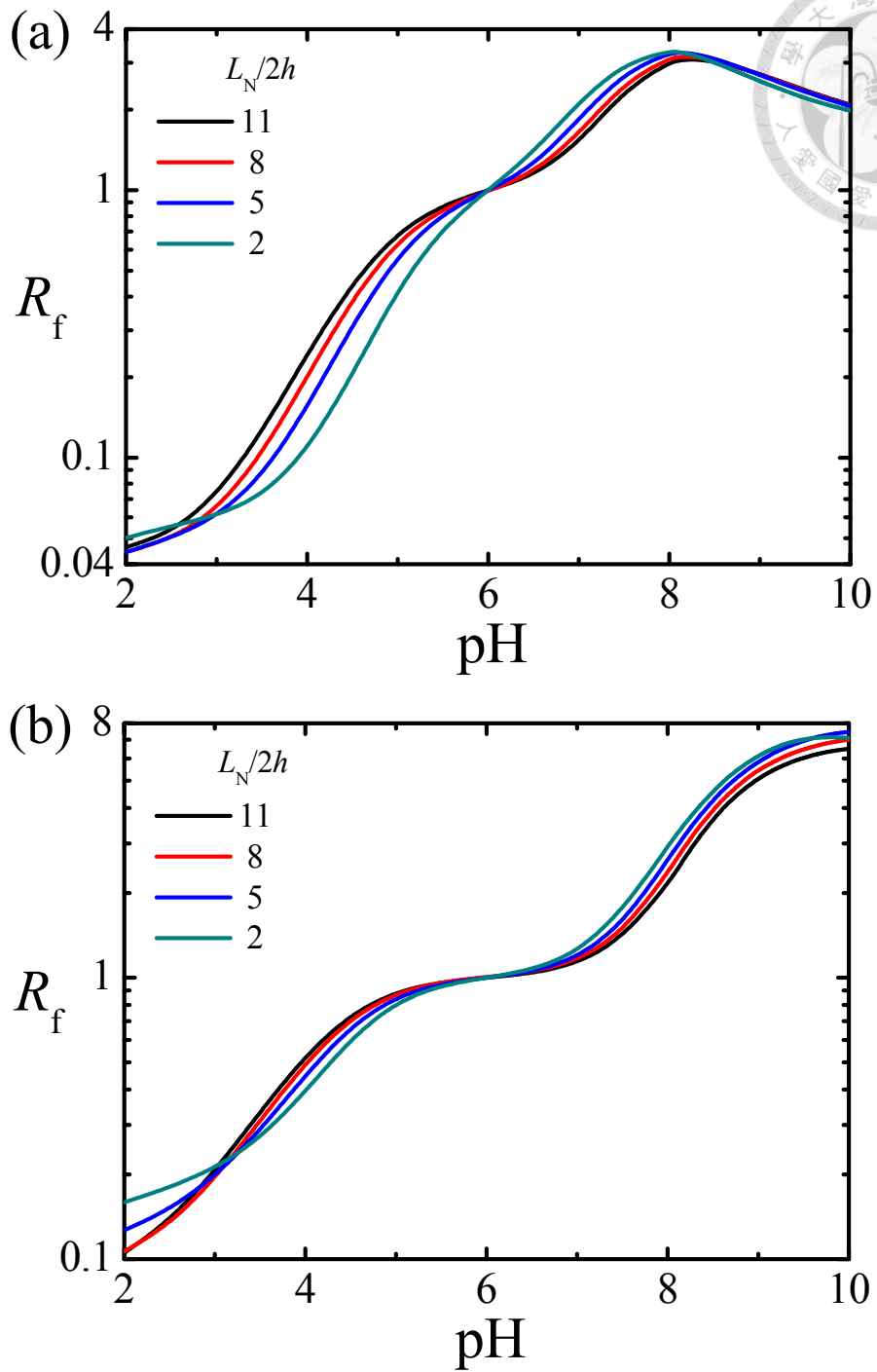
Figure 2-10. Variation in the R_f with pH for various combinations of C_0 and ($L_N/2h$) at

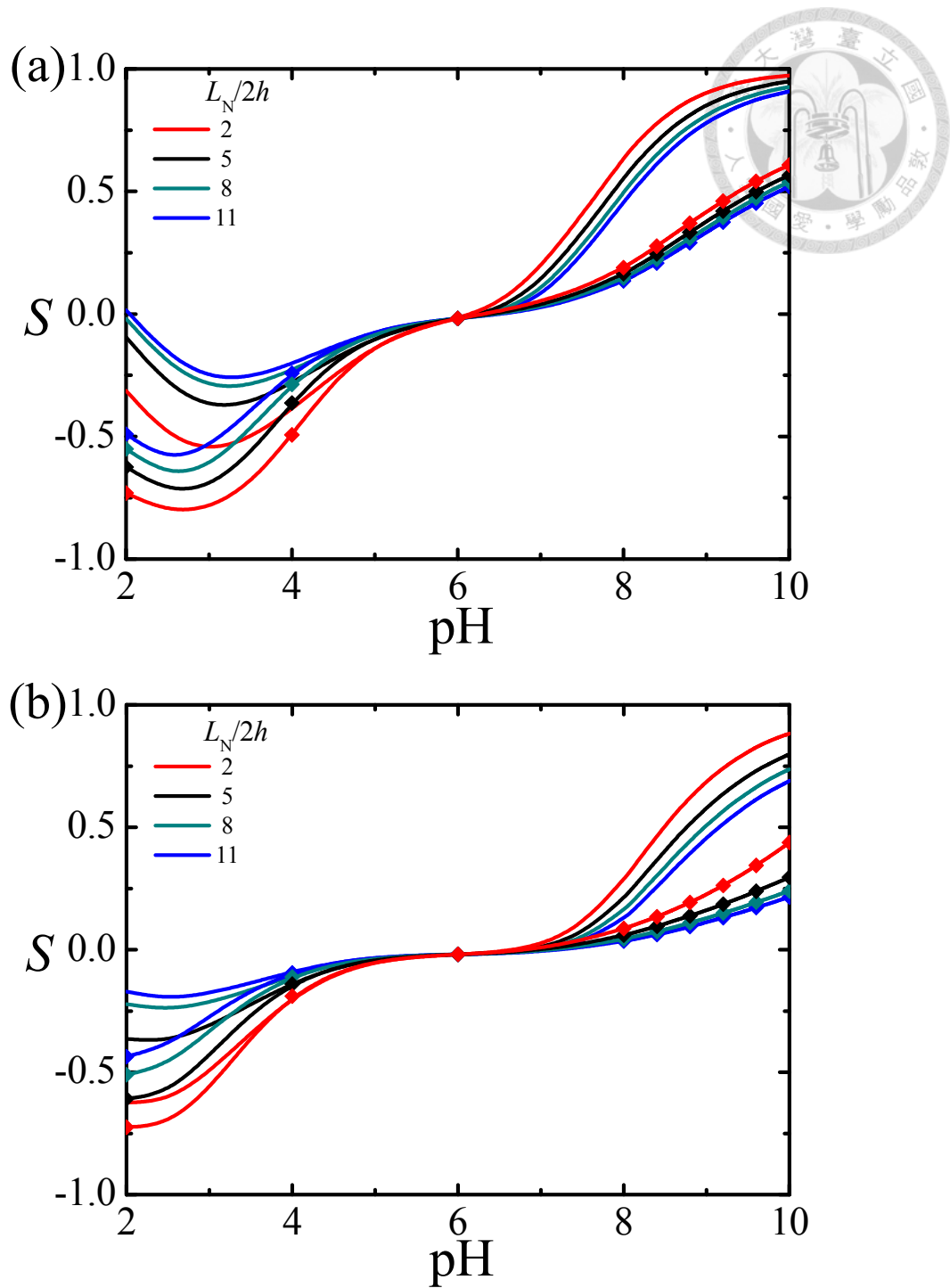R_t=5 nm and R_b=25 nm. C_0=10 mM in (a), C_0=100 mM in (b).

Figure 2-11. Variation in the selectivity S with pH for various combinations of C_0 and $(L_N/2h)$ at R_t=5 nm and R_b=25 nm. C_0=10 mM in (a), C_0=100 mM in (b). Solid curve: V=+1 V; solid curve with discrete symbols: V=−1 V.
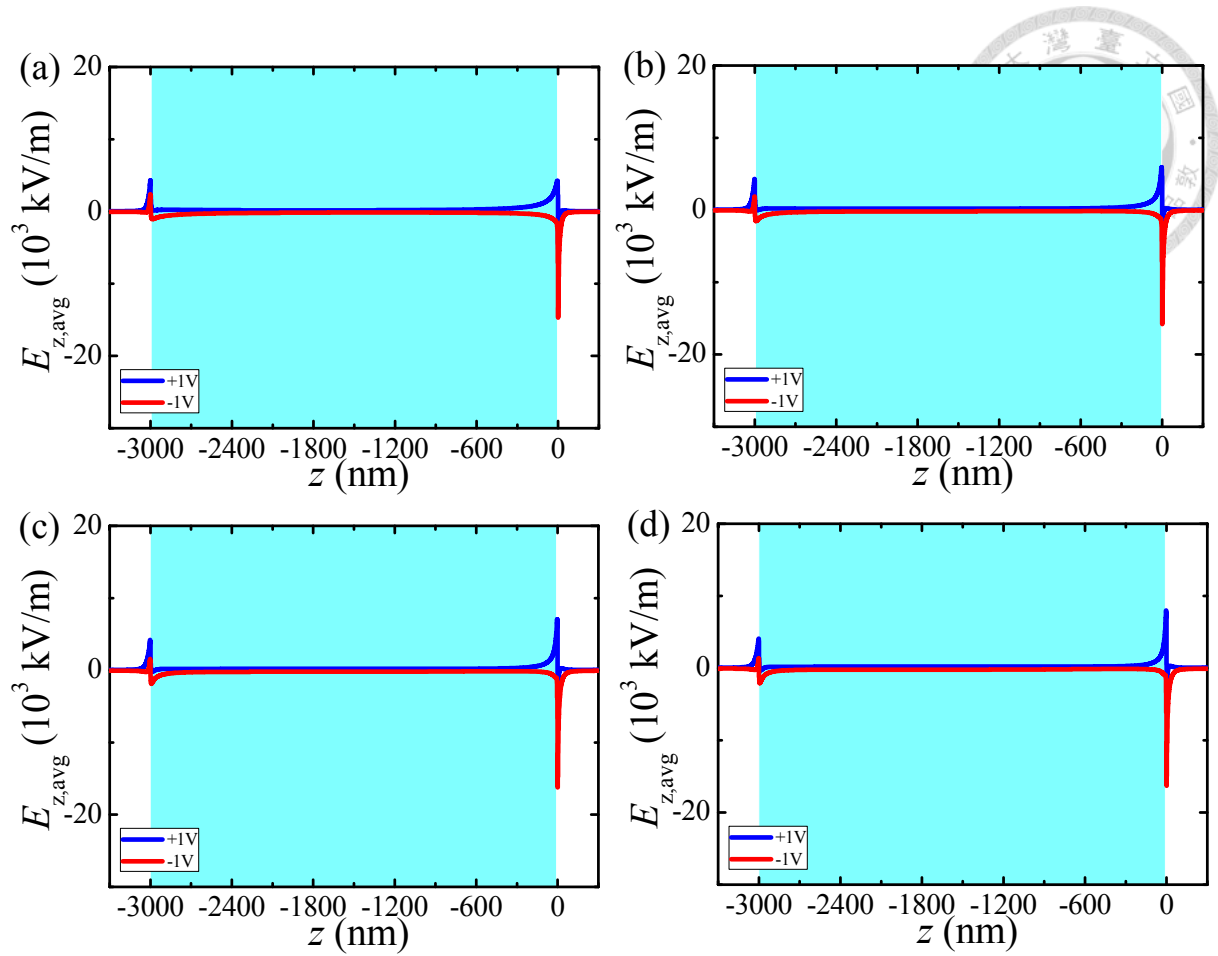
Figure S1. Axial distribution of the cross sectional averaged electric field $E_{z,avg}$ at pH 10, R_t=5 nm, R_b=25 nm and C_0=1 mM for V=+1 V (blue curve) and V=−1 V (red curve). ($L_N/2h$) is 2, (a), 5, (b), 8, (c), and 11, (d). Shaded area denotes nanochannel interior.
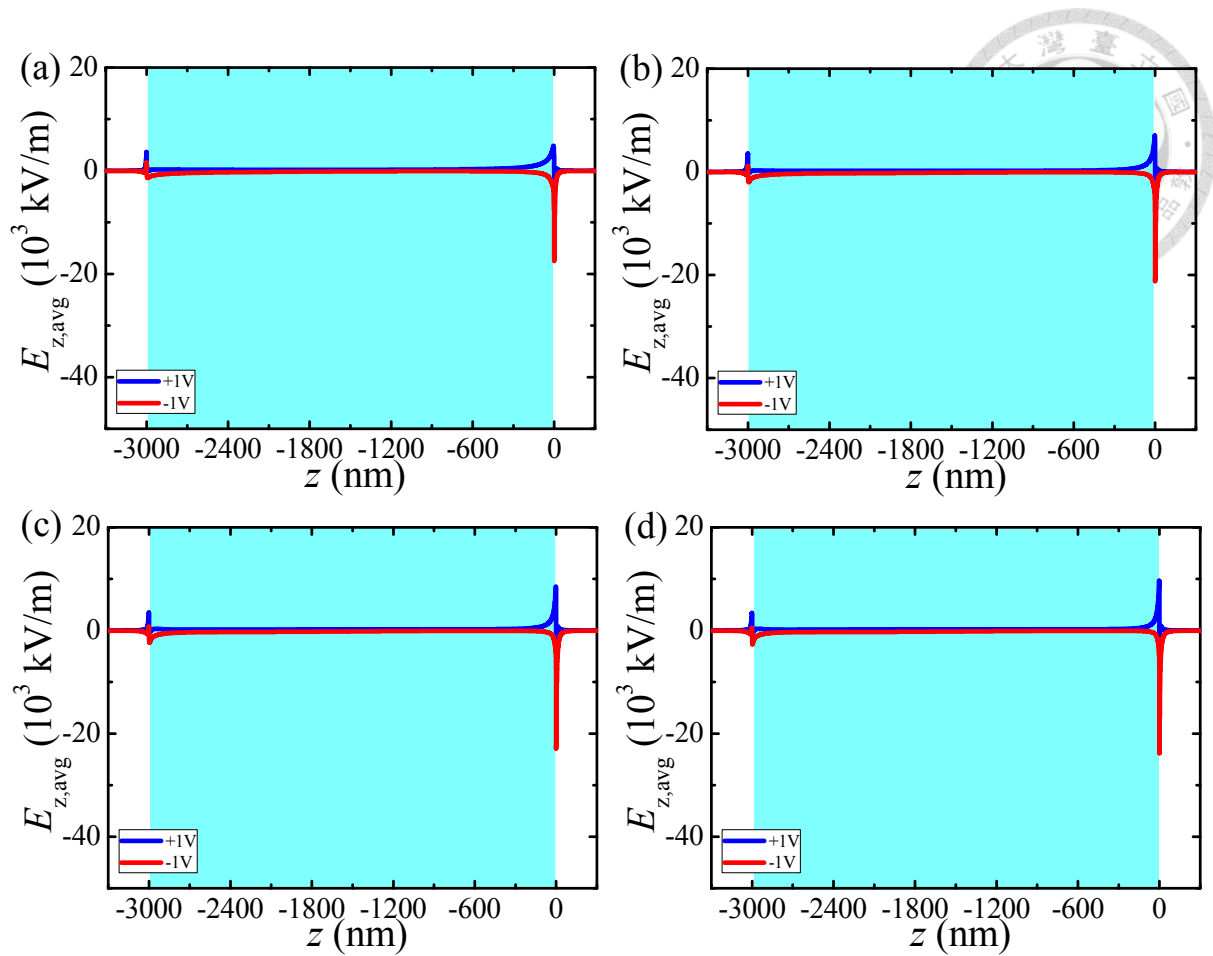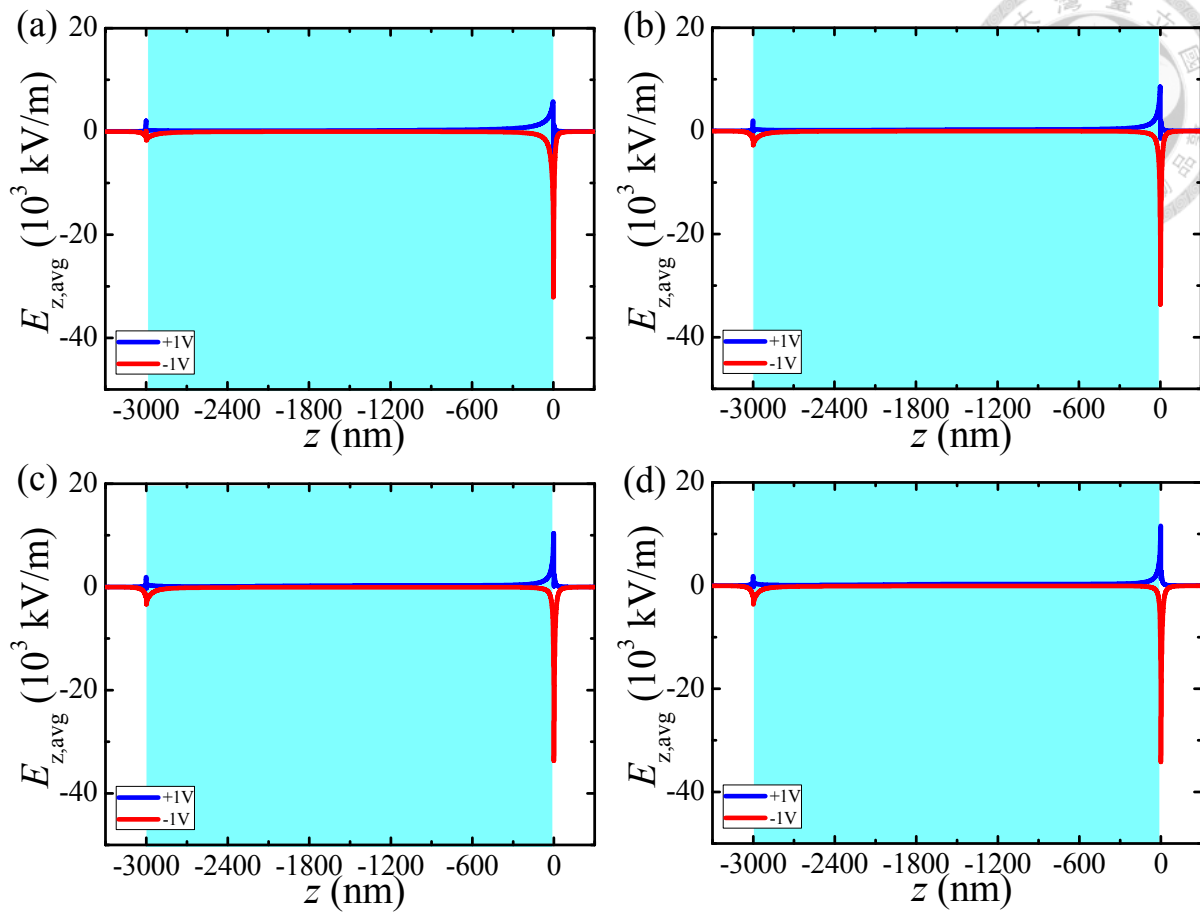
88

Figure S2. Axial distribution of the cross sectional averaged electric field $E_{z,avg}$ at pH 10, R_t=5

nm, R_b=25 nm and C_0=10 mM for V=+1 V (blue curve) and V=−1 V (red curve). ($L_N/2h$) is 2, (a),

5, (b), 8, (c), and 11, (d). Shaded area denotes nanochannel interior.

89

Figure S3. Axial distribution of the cross sectional averaged electric field $E_{z,avg}$ at pH 10, R_t=5 nm, R_b=25 nm and C_0=100 mM for V=+1 V (blue curve) and V=−1 V (red curve). ($L_N/2h$) is 2, (a), 5, (b), 8, (c), and 11, (d). Shaded area denotes nanochannel interior.
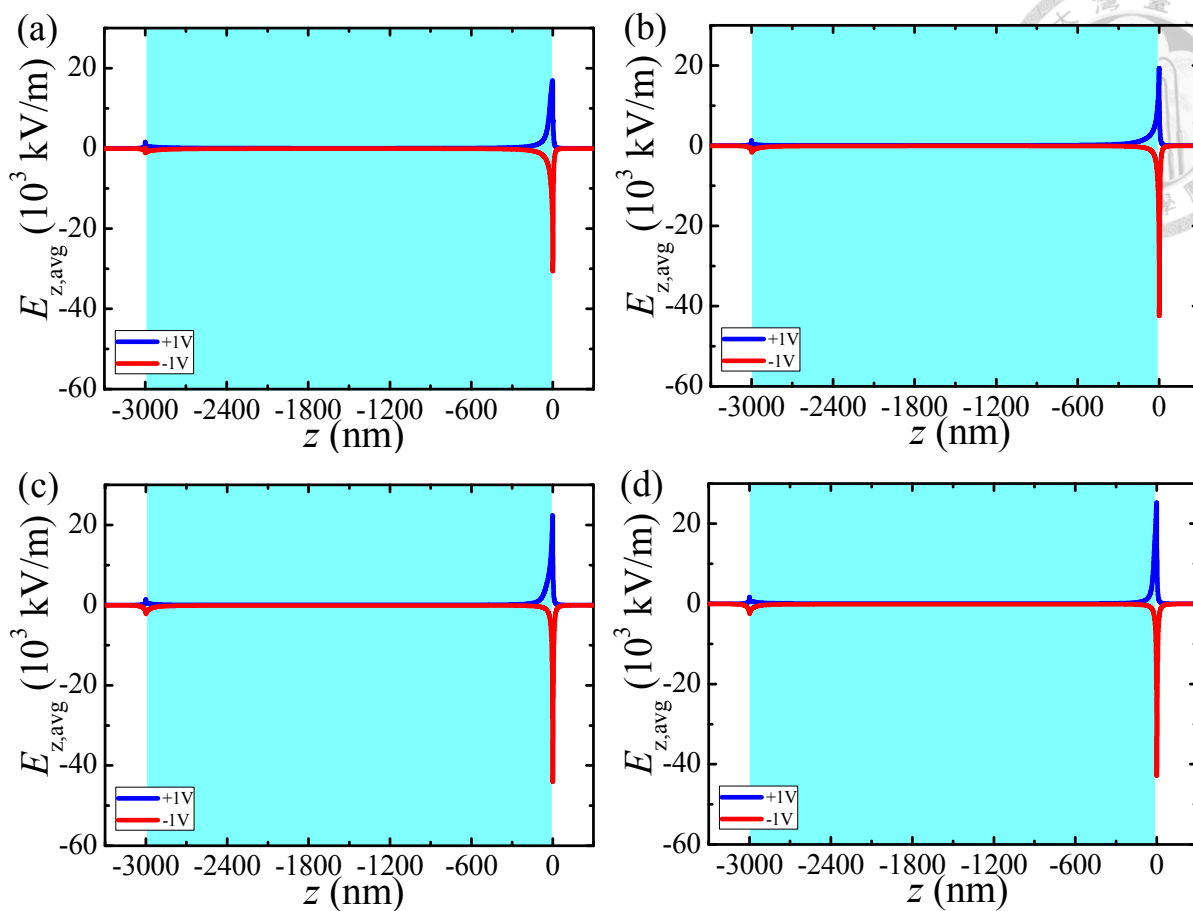
90

Figure S4. Axial distribution of the cross sectional averaged electric field $E_{z,avg}$ at pH 10, R_t=5

nm, R_b=25 nm and C_0=500 mM for V=+1 V (blue curve) and V=−1 V (red curve). ($L_N/2h$) is 2,

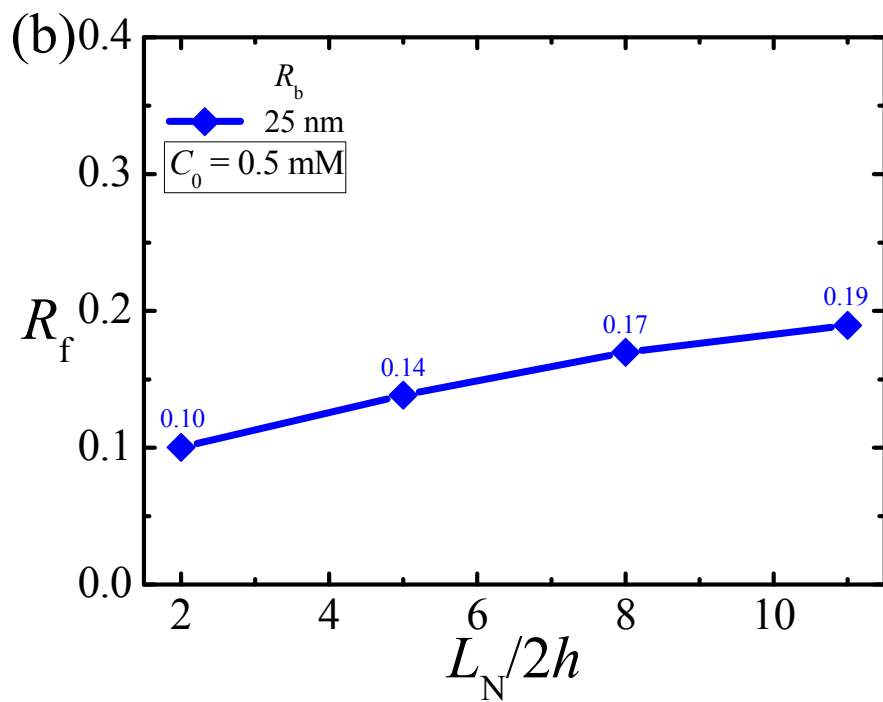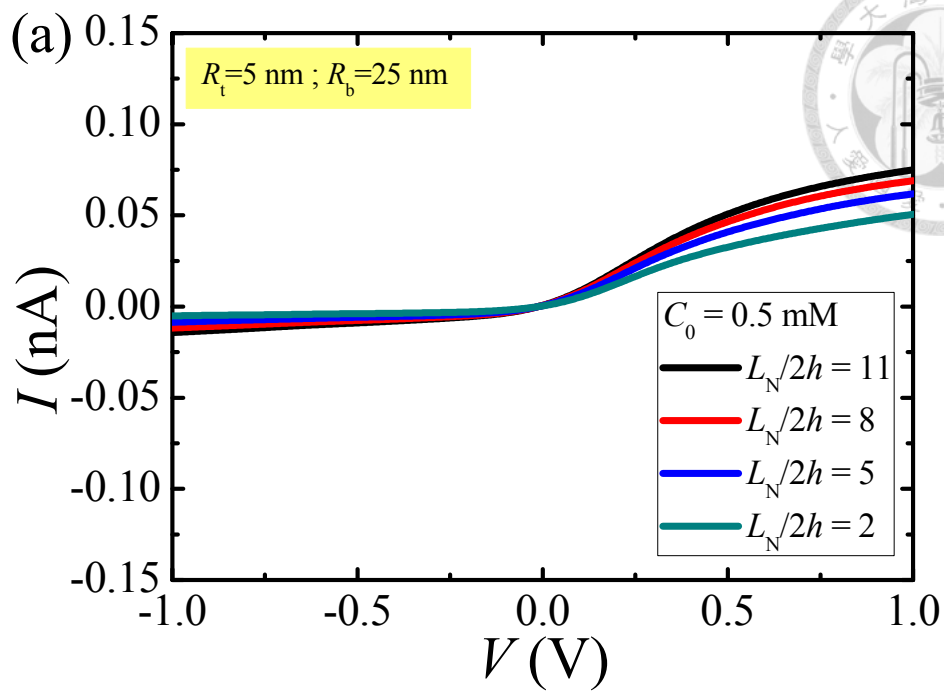(a), 5, (b), 8, (c), and 11, (d). Shaded area denotes nanochannel interior.

Figure S5. (a) Simulated $I-V$ curve for various levels of ($L_N/2h$) and (b) variation in R_f with ($L_N/2h$) at pH 4, R_t=5 nm, R_b=25 nm and C_0=0.5 mM.
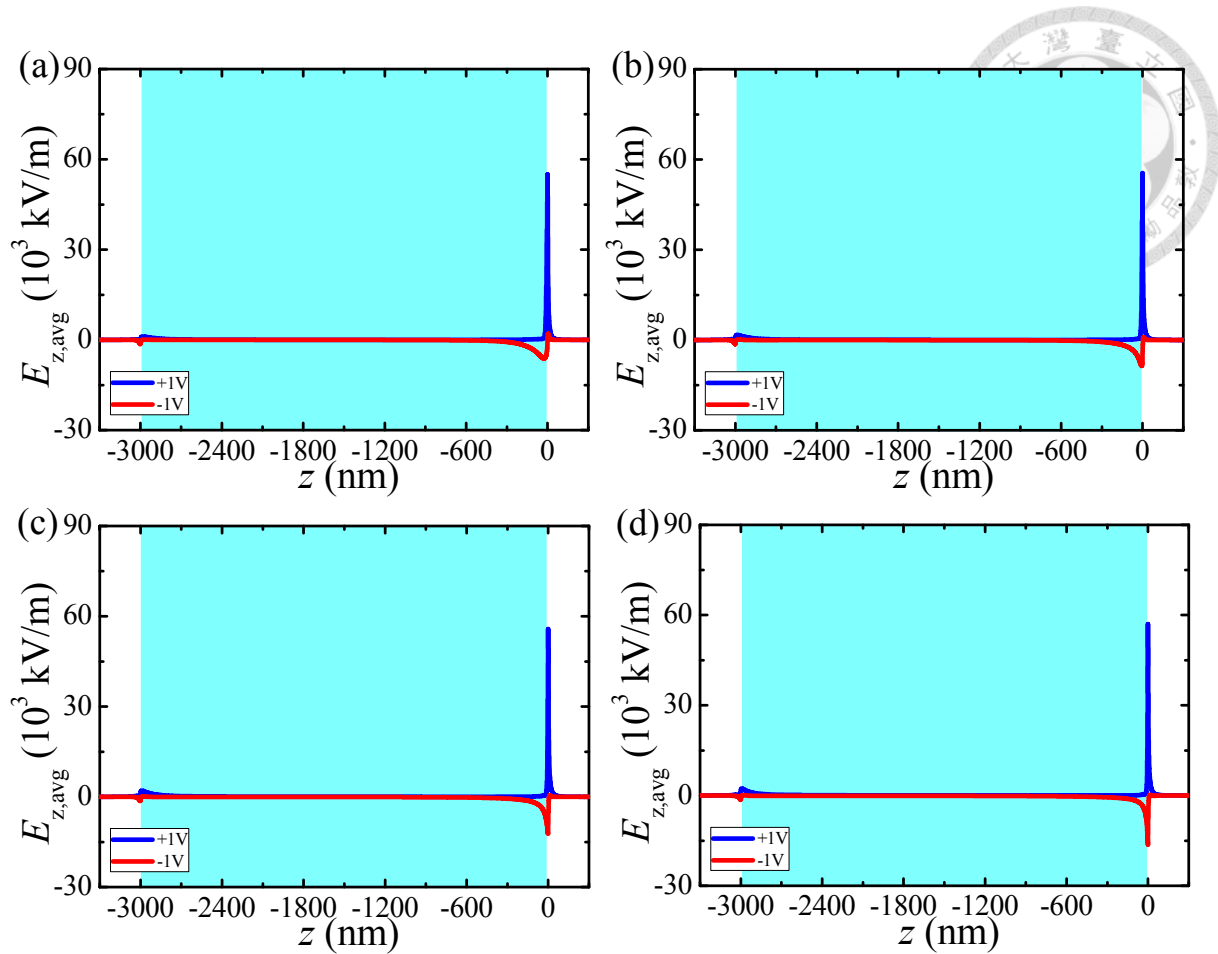
Figure S6. Axial distribution of the cross sectional averaged electric field $E_{z,avg}$ at pH 4, R_t=5 nm,

R_b=25 nm and C_0=1 mM for V=+1 V (blue curve) and V=−1 V (red curve). ($L_N/2h$) is 2, (a), 5,

(b), 8, (c), and 11, (d). Shaded area denotes nanochannel interior.
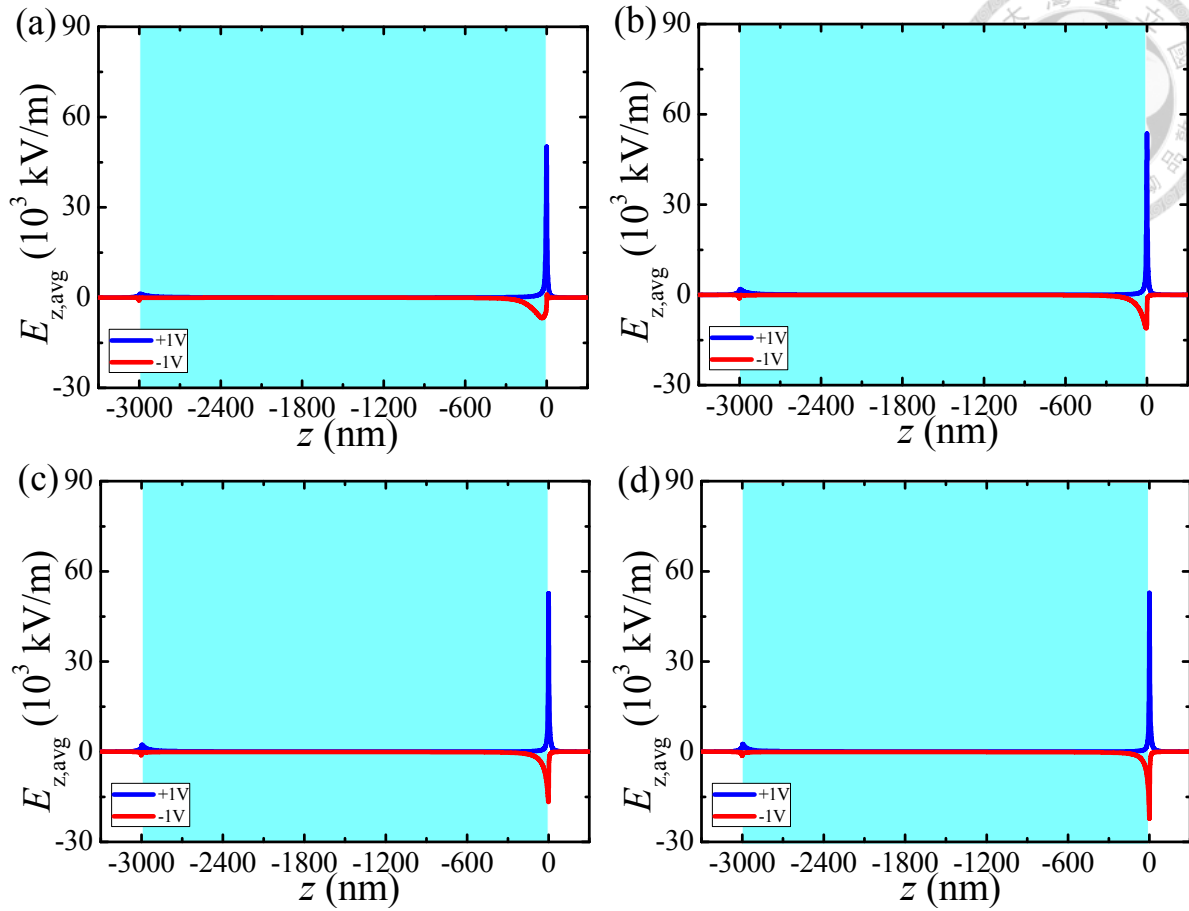
93

Figure S7. Axial distribution of the cross sectional averaged electric field $E_{z,avg}$ at pH 4, R_t=5 nm, R_b=25 nm and C_0=10 mM for V=+1 V (blue curve) and V=−1 V (red curve). ($L_N/2h$) is 2, (a), 5, (b), 8, (c), and 11, (d). Shaded area denotes nanochannel interior.

94

Figure S8. Axial distribution of the cross sectional averaged electric field $E_{z,avg}$ at pH 4, R_t=5 nm, R_b=25 nm and C_0=100 mM for V=+1 V (blue curve) and V=−1 V (red curve). ($L_N/2h$) is 2, (a), 5, (b), 8, (c), and 11, (d). Shaded area denotes nanochannel interior.
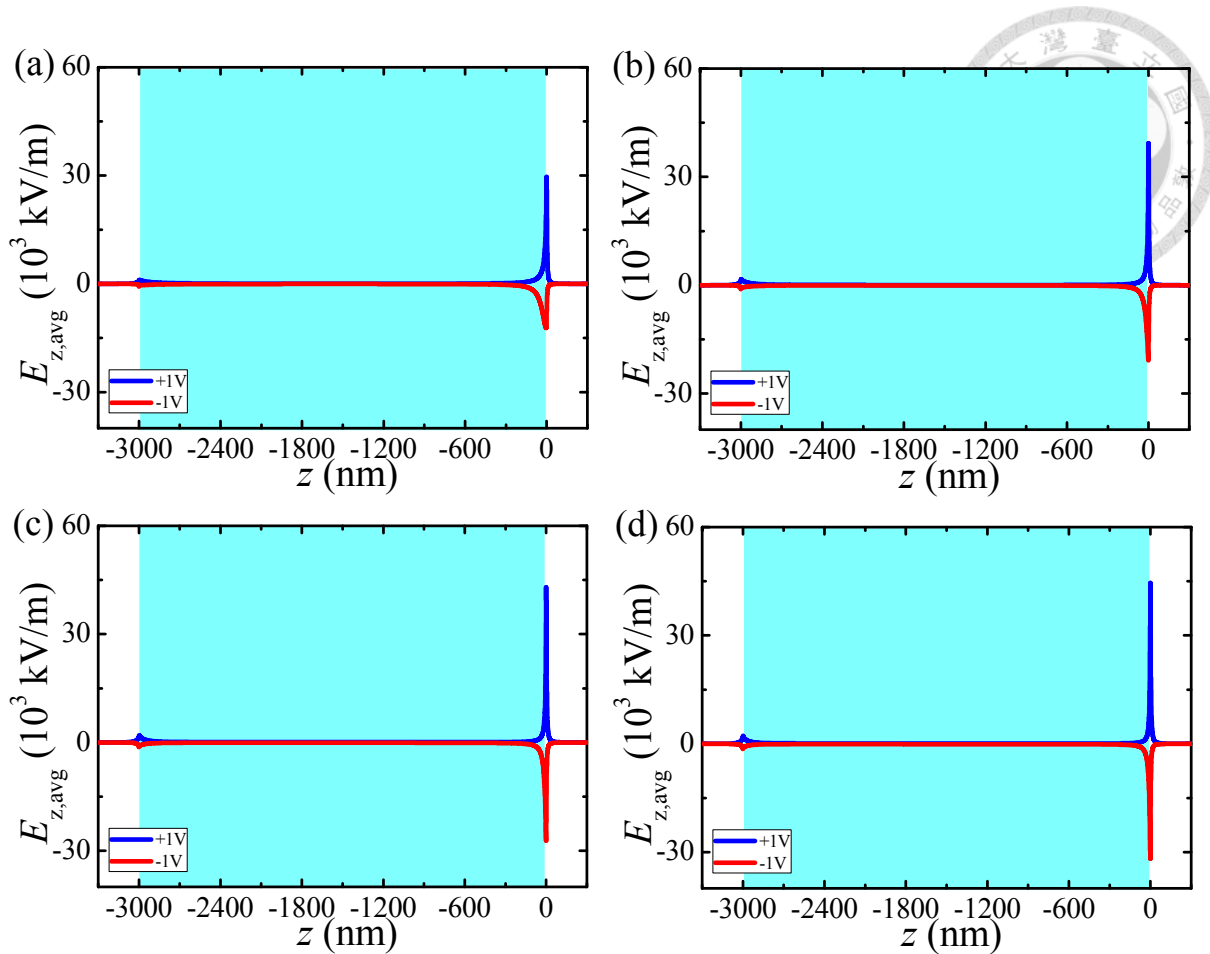
95

Figure S9. Axial distribution of the cross sectional averaged electric field $E_{z,avg}$ at pH 4, R_t=5 nm, R_b=25 nm and C_0=500 mM for V=+1 V (blue curve) and V=−1 V (red curve). ($L_N/2h$) is 2, (a), 5, (b), 8, (c), and 11, (d). Shaded area denotes nanochannel interior.
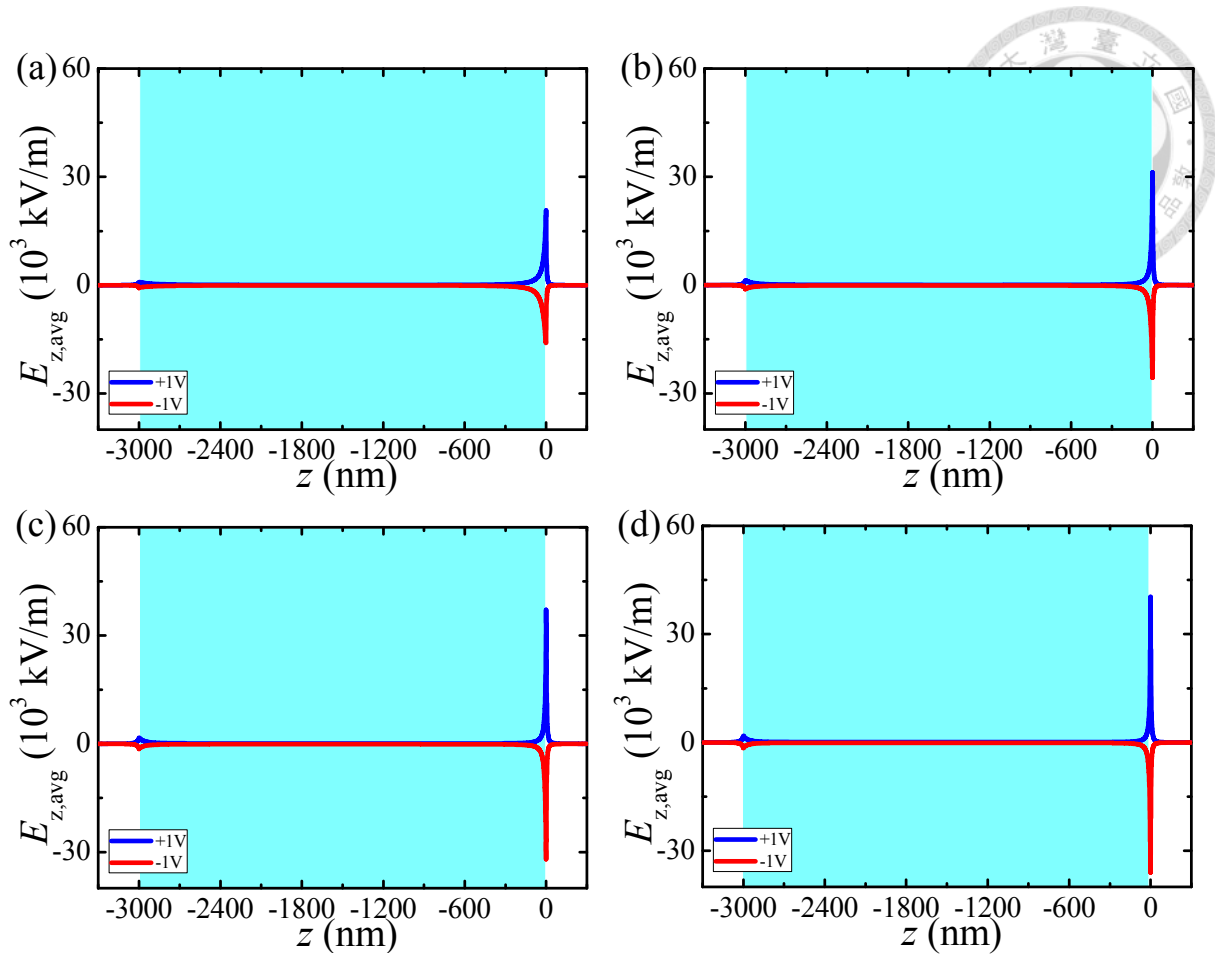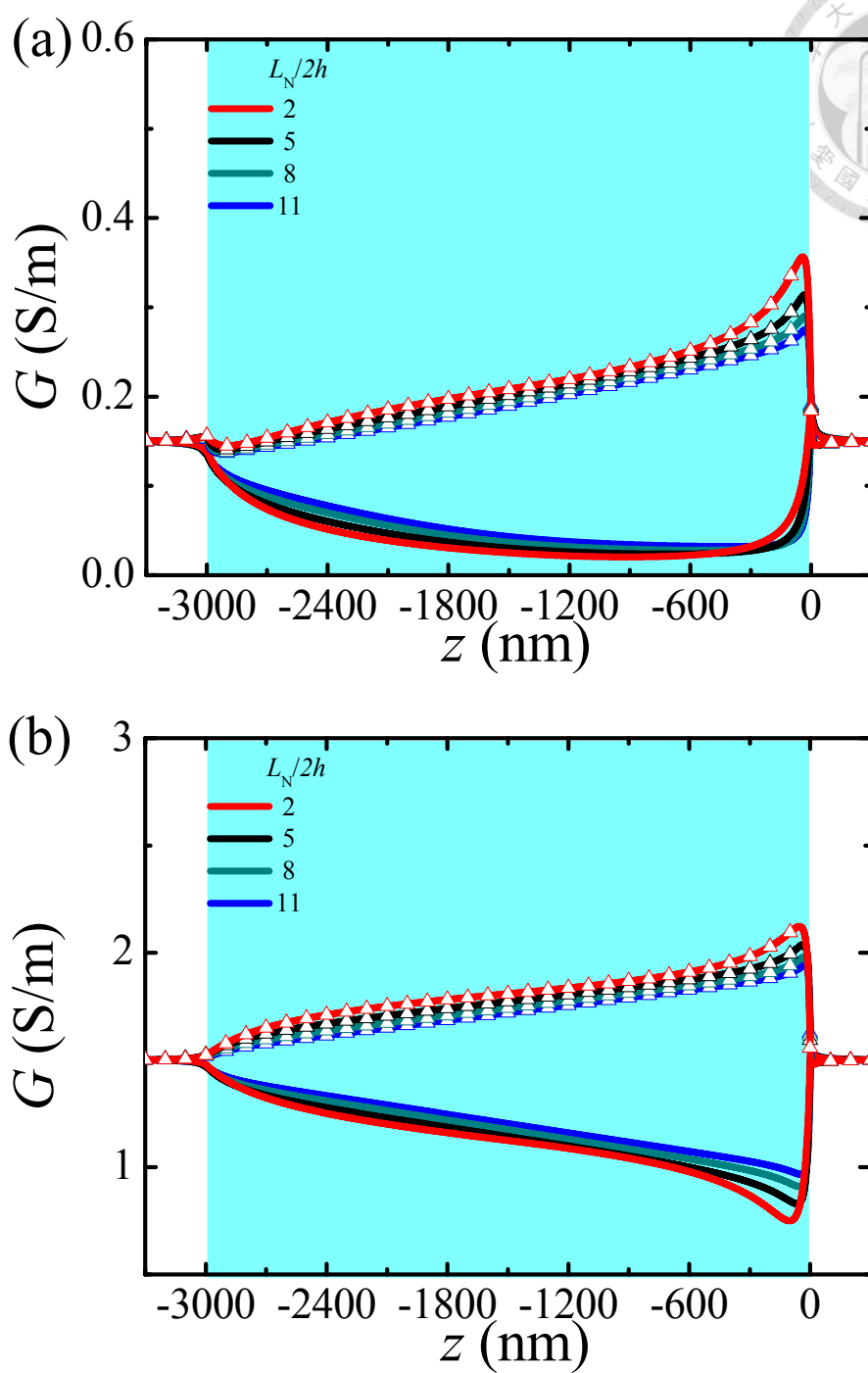
Figure S10. Axial variation in the cross sectional averaged ionic conductivity G at pH 7.5, R_t=5 nm and

R_b=25 nm for various levels of bulk salt concentration C_0. (a) C_0=10 mM, (b) C_0=100 mM. Solid curves:

V=+1 V; solid curves with discrete symbols: V=−1 V. Shaded region denotes the nanochannel interior.

97

Figure S11. Axial variation in the cross sectional averaged ionic conductivity G at pH 2, R_t=5 nm and

R_b=25 nm for various levels of bulk salt concentration C_0. (a) C_0=10 mM, (b) C_0=100 mM. Solid curves:

V=+1 V; solid curves with discrete symbols: V=−1 V. Shaded region denotes the nanochannel interior.
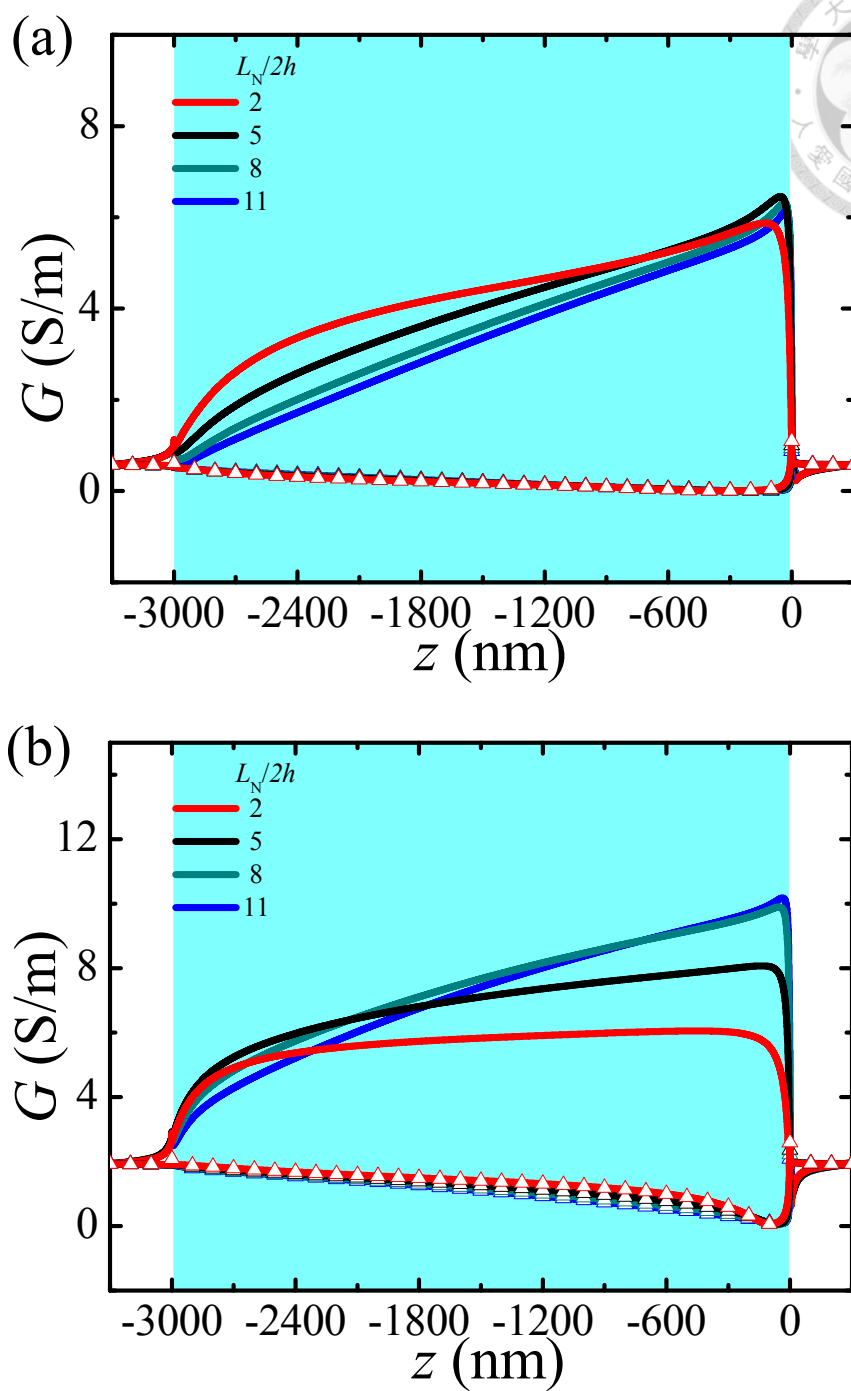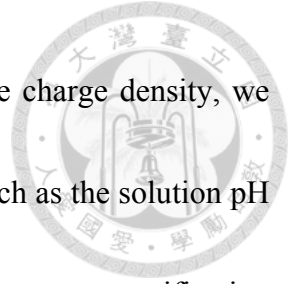
98

Conclusion

In Chapter 1, we theoretically analyze the influence of the ionic valence on the electrokinetic behavior of a conical nanochannel, in particular, its current-voltage characteristics and ionic current rectification (ICR) phenomenon. Typical salts including KCl, KNO$_3$, K$_2$SO$_4$, CaCl$_2$, and LaCl$_3$ are considered, for illustration. Due to the difference in the ionic strength and the diffusivity of ions, the behaviors of the current-voltage curves for the types of salt examined are different both quantitatively and qualitatively. The rectification factor has a local maximum as the salt concentration increases. In addition, the local maximum position is related to the asymmetry of salt valence ratio: the higher the ionic valence the lower the salt concentration at which the rectification factor has the local maximum. However, the maximal rectification factor occurs at the same ionic strength, regardless of the type of salt, implying that the thickness of electric double layer plays the key role. The ICR behavior of a positively charged conical nanochannel is qualitatively similar to that of a negatively charged nanochannel.

In Chapter 2, taking account of the effect of electroosmotic flow (EOF), the electrokinetic ion transport in a cigar-shaped nanochannel modified with pH-tunable, zwitterionic functional groups is modeled for the first time. Extending previous studies,

99

where the surface of a nanochannel is assumed a constant surface charge density, we

assume that its charged conditions depend upon external stimuli such as the solution pH

and the bulk salt concentration, which is closer to reality. The ion current rectification

(ICR) and the ionic selectivity behaviors of the nanochannel are investigated and the

associated mechanisms interpreted. Based on a thorough numerical simulation we

conclude the following. (i) Depending upon the direction of the applied electric field, the

asymmetric geometry of the cigar-shaped nanochannel yields either ion enrichment or ion

depletion inside it. (ii) The degree of electric double layer overlapping inside the

nanochannel is influenced by the solution pH, the bulk salt concentration, the applied

potential bias, the opening radii and the shape of the nanochannel, so is the nanochannel

performance. (iii) Since the ion transport in the nanochannel is governed mainly by its

surface charge, both the rectification behavior and the ion selectivity depend highly on

the bulk salt concentration and the solution pH. (iv) The axial variation of the ionic

conductivity and that of the electric field in the nanochannel play a significant role. In

particular, the nanochannel shape affects significantly the electric field, especially near

the tip region, which eventually determines the performance of the nanochannel. (v) This

study is an initial step for future work on structure-function relationships that will pave

the way for designing membranes for specific purposes and providing valuable

information for establishing smart nanochannel systems. These show great promise in

many applications, including ionic gates/diodes, energy conversion, and drug controlled

release.